AFWAL-TR-81-3053
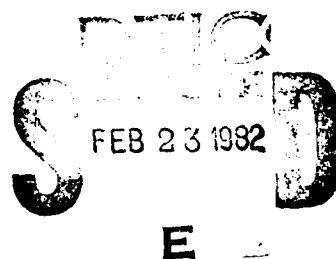
THE NUMERICAL SOLUTION OF THE NAVIER-STOKES EQUATIONS FOR INCOMPRESSIBLE TURBULENT FLOW OVER AIRFOILS

Harwood A. Hegna, Capt., USAF

Aerodynamics and Airframe Branch
Aeromechanics Division

DTIC
FEB 23 1982

E

October 1981

Final Report for Period October 1979 - February 1981

FLIGHT DYNAMICS LABORATORY
AIR FORCE WRIGHT AERONAUTICAL LABORATORIES
AIR FORCE SYSTEMS COMMAND
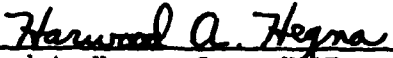WRIGHT-PATTERSON AIR FORCE BASE, OHIO 45433

8202 23 056

392 662

REPORT DOCUMENTATION PAGE	READ INSTRUCTIONS BEFORE COMPLETING FORM
1. REPORT NUMBER AFWAL-TR-81-3053 2. GOVT ACCESSION NO. *AD-A111 277*	3. RECIPIENT'S CATALOG NUMBER
4. TITLE (and Subtitle) THE NUMERICAL SOLUTION OF THE NAVIER-STOKES EQUATIONS FOR INCOMPRESSIBLE TURBULENT FLOW OVER AIRFOILS	5. TYPE OF REPORT & PERIOD COVERED Final Technical Report October 1979 - February 1981 6. PERFORMING ORG. REPORT NUMBER
7. AUTHOR(s) Harwood A. Hegna, Captain, USAF	8. CONTRACT OR GRANT NUMBER(s)
9. PERFORMING ORGANIZATION NAME AND ADDRESS Computational Aerodynamics Group Aerodynamics and Airframe Branch Wright-Patterson Air Force Base, Ohio 45433	10. PROGRAM ELEMENT, PROJECT, TASK AREA & WORK UNIT NUMBERS 2307N603
11. CONTROLLING OFFICE NAME AND ADDRESS Flight Dynamics Laboratory AF Wright Aeronautical Laboratories, AFSC Wright-Patterson Air Force Base, Ohio 45433	12. REPORT DATE October 1981 13. NUMBER OF PAGES 151
14. MONITORING AGENCY NAME & ADDRESS(if different from Controlling Office)	15. SECURITY CLASS. (of this report) Unclassified 15a. DECLASSIFICATION/DOWNGRADING SCHEDULE

16. DISTRIBUTION STATEMENT (of this Report)

Approved for public release; distribution unlimited.

17. DISTRIBUTION STATEMENT (of the abstract entered in Block 20, if different from Report)

18. SUPPLEMENTARY NOTES

19. KEY WORDS (Continue on reverse side if necessary and identify by block number)

Aerodynamics
Airfoils
Viscous Flow
Navier-Stokes
Numerical Methods

20. ABSTRACT (Continue on reverse side if necessary and identify by block number)

Numerical solutions are obtained for two-dimensional incompressible turbulent viscous flow over airfoils of arbitrary geometry. An algebraic eddy viscosity turbulence model based on Prandtl's mixing length theory is modified for separated adverse pressure gradient flows. Finite difference methods for solving the inviscid stream function equation and the incompressible laminar Navier-Stokes equations are used. A finite difference method for solving the Reynolds averaged incompressible turbulent two-dimensional Navier-Stokes equations is employed.

DD FORM 1473 1 JAN 73   EDITION OF 1 NOV 65 IS OBSOLETE

Block 20 (ABSTRACT)

The inviscid stream function equation and the Navier-Stokes equations
are transformed using a curvilinear transformation. A body-fitted coor-
dinate system with a constant coordinate line defining the airfoil section
surface is transformed to a rectangular coordinate system in the trans-
formed or computational plane. An elliptic partial differential Poisson
equation for each coordinate is used to generate the coordinate system in
the physical plane for arbitrary airfoils.

The two-dimensional time dependent Reynolds averaged incompressible
Navier-Stokes equations in the primitive variables of velocity and pressure
and a Poisson pressure equation are numerically solved. Turbulence is
modelled with an adverse pressure gradient eddy viscosity technique. An
implicit finite difference method is used to solve the set of transformed
partial differential equations. The system of linearized simultaneous
difference equations, at each time step, is solved using successive-over-
relaxation iteration. Far field boundary conditions are examined. Solutions
for a NACA 0012 airfoil at angles of attack varying from five to 11.5 degrees
at a chord Reynolds number of 170,000 are obtained. Velocity profiles near
the airfoil surface and surface pressure distributions are presented and
compared with experimental data. Lift and drag coefficients agree well with
experimental values. The computed lift coefficients near stall are within 5%
of the experimental measurements, and the numerical drag coefficients agree
within ten drag counts in the region of maximum lift to drag ratio. The
short laminar separation bubble near the suction pressure peak is numerically
determined. The variation of bubble length and turbulent transition length
with angle of attack are similar to experimental trends.

PREFACE

This report is the result of the work performed by Captain Harwood A. Hegna, AFWAL/FIMM, under Project Number 2307N603, Computational Fluid Dynamics. This work is based on the author's Ph D Dissertation at the Air Force Institute of Technology which was sponsored by the Flight Dynamics Laboratory, Air Force Wright Aeronautical Laboratories, Wright-Patterson Air Force Base, Ohio.

The author is very grateful for the encouragement and support provided by both Dr. Wilbur Hankey, Technical Manager, and Dr. Joseph Shang. The professionalism displayed by the members of the Computational Aerodynamics Group is also acknowledged.

Accession For	
NTIS GRA&I	☒
DTIC TAB	☐
Unannounced	☐
Justification	
By	
Distribution/	
Availability Codes	
Dist	Avail and/or Special
A	

AFWAL-TR-81-3053

TABLE OF CONTENTS

TABLE OF CONTENTS (Concluded)

LIST OF ILLUSTRATIONS

LIST OF ILLUSTRATIONS (Concluded)

LIST OF TABLES

LIST OF SYMBOLS

SYMBOL

a	Radius of cylinder in the far field boundary condition
A	Coefficient matrix in Reynolds stress model; constant in inner eddy viscosity relaxation factor; cross-section area for two-dimensional contour integrals; and coefficient matrix for finite difference equations
A_k	The kth amplification factor at a ξ line in the coordinate attraction technique
A^+	Laminar sublayer relaxation distance
A1,A2,A3	Constants occurring in the surface point distribution method
ALFA	Modified grid transformation coefficient α/J^2
b	Column matrix of "constants" in finite difference equations expression
$\underline{b}$	Body force per unit mass
B	Constant in the inner eddy viscosity relaxation factor; and coefficient of p_{ij} denoting a combination of grid transformation quantities in Equation E-4
BETA	Modified grid transformation coefficient $-\beta/2J^2$
c	Airfoil chord
c_1,c_2	The x and y components of unit outward normal vector from the body surface
C_b,C_f	Contours which define the body surface and far field boundary
C_n	Coefficients in Blasius' series
C_1,C_2	Contours which define the cut in the physical plane
C_{fx},C_{fy}	The x and y components of the force coefficients
C_{MP}	Counterclockwise moment coefficient about point (x_p,y_p)
D	Flow field dilatation or divergence

LIST OF SYMBOLS (Continued)

<u>SYMBOL</u>

D_L	Laminar sublayer damping factor
D_1, D_2	Combinations of grid transformation quantities defined by Equations A-4 and A-5
$D(\xi)$	Coordinate attraction damping factor
E	Convergence error criteria
f	Inner eddy viscosity relaxation factor; and maximum airfoil thickness as a fraction of the chord
<u>f</u>	Force per unit length of span exerted by the fluid on the airfoil
$f(\sigma)$	Blasius' series solution
$f(\xi, n)$	General function in the computational plane
F_1, F_2	The x and y components of a general vector function $\underline{F}(x, y, t)$.
<u>F</u>	Force exerted by the fluid on a body
F(s)	Airfoil thickness function
$\underline{F}(x,y,t)$	General vector function
$g(\xi, n)$	General function in the computational plane
G	An empirical constant in the model for the gradient diffusion term
GAMA	Modified grid transformation coefficient γ / J^2
H_{12}	Local shape factor δ^* / Θ.
$H(n, n_k)$	Difference function used in the coordinate attraction method given by Equation 21.
i	Complex number
$\hat{i}$	Unit vector in the x coordinate direction
I	Numerical index for the ith ξ location
IC1, IV1	Numerical upwind difference designators for i-1.

xi

LIST OF SYMBOLS (Continued)

SYMBOL

IC2, IV2	Numerical upwind difference designators for i-2
IMAX	Numerical designator for the maximum number of ξ lines
$\hat{j}$	Unit vector in the y coordinate direction
J	Jacobian of the grid transformation; and numerical index for the jth η location
JC1, JV1	Numerical upwind difference designators for j-1
JC2, JV2	Numerical upwind difference designators for j-2
JMAX	Numerical designator for the maximum number of η lines
k	Turbulent kinetic energy; and summation index
$\hat{k}$	Unit vector in the direction perpendicular to the x-y plane
k_1, k_2, k_3	Inner, outer, and far wake parameters in the turbulence eddy viscosity model
k_{1i}, k_{1f}	The initial and final values for the parameter k_1 in the inner eddy viscosity relaxation factor
$K(\xi)$	Number of points specified in the boundary-layer using the coordinate attraction method
L	Turbulence length scale; and a characteristic length in the contour integral force calculation method
L_B	Length of the calculated laminar separation bubble
M	Pressure gradient parameter $-\theta^2 Re \, du_e/ds$
n	Summation index; designates the nth time step; and a normal coordinate direction
$\hat{n}$	Unit vector in the n coordinate direction; and a unit outward normal vector for a closed contour
n_1, n_2	The x and y components of the unit outward normal vector of the body surface
N	The sum of the laminar and turbulent viscosity coefficients in a rate equation approach to turbulence

LIST OF SYMBOLS (Continued)

SYMBOL

N_Q — Specified constant or function in a model for the turbulent gradient diffusion term

p — Fluid static pressure variable

p^* — Current value of the fluid static pressure obtained from the finite difference equation

$P(\xi,\eta)$ — Attraction function for ξ lines

q — Turbulence velocity scale defined by $(\overline{u_i' u_i'})^{\frac{1}{2}}$

Q — Coefficient of u_{ij} denoting a combination of grid transformation quantities used in Equation E-2

Q_k — Velocity characteristic of large eddy motions in a model for the turbulent gradient diffusion term

$Q(\xi,\eta)$ — Attraction function for η lines

r — Constructive grid parameter; and radius in the far field boundary condition model

$\underline{r}$ — Position vector relative to origin in the physical plane

R — Region in the physical plane

$\underline{R}$ — Vector representation for the convective and viscous terms in the momentum equation

$R(r)$ — Radial stretching function in the constructive grid method

Re — Freestream Reynolds number $U_\infty c/\nu$

Re_t — Turbulent Reynolds number defined by Equation 37

Re_δ^* — Reynolds number based on the local boundary-layer displacement thickness and defined as $u_e \delta^*/\nu$

Re_Θ — Reynolds number based on the local boundary-layer momentum thickness and defined as $u_e \Theta/\nu$

RHS — Time dependent and nonlinear terms in the Poisson pressure equation

s — Arclength or surface tangent coordinate; and generalized airfoil chord direction variable

LIST OF SYMBOLS (Continued)

<u>SYMBOL</u>

s_d	Delay distance in the inner eddy viscosity relaxation factor
s_r	Relaxation distance in the inner eddy viscosity relaxation factor
s_η	General contour which enclosed a two-dimensional body
$s_\eta(\xi)$	Function which specifies the rate of change of arclength with η at the body surface
S_b	General body contour in the contour integral method
sgn	Sign function
t	Constructive grid parameter; time variable; and the maximum airfoil thickness
T	Characteristic time period c/U_∞
$\overline{\overline{T}}$	Traction stress tensor
u	Variable which denotes the local x component of flow field velocity
u*	Current value of the u component of velocity obtained from the finite difference equation
$\tilde{u}$	Tangential field velocity component relative to the body surface tangential direction
U	Column matrix representation of the variables at the grid point locations for the system of finite difference equations
U_∞	Magnitude of the freestream velocity
UC	Quantity which is proportional to the component of the local fluid velocity in the ξ direction
UV	Combination of grid transformation coefficients $-\tau/2J^2$.
UX,UY	The derivative of the local u velocity with respect to x and y evaluated in the computational plane
v	Variable which denotes the local y component of the flow field velocity

LIST OF SYMBOLS (Continued)

<u>SYMBOL</u>

v^* — Current value of the v velocity component obtained from the finite difference equation

$\tilde{v}$ — Normal field velocity component relative to the surface normal direction

V — Control volume

v_k, V_k — The kth velocity component in indicial notation

VC — Quantity which is proportional to the component of the local fluid velocity in the η direction

VV — Combination of grid transformation coefficients $-\sigma/2J^2$.

VX, VY — The derivative of the local v velocity component with respect to x and y evaluated in the computational plane

w_o — Function which gives the maximum velocity defect in the wake at each location downstream

W — Nondimensional complex valued velocity u-iv

$\tilde{W}$ — Complex valued velocity U_∞ (u-iv)

WL_1 — Non-interacting length in the near wake measured from the trailing edge of the airfoil

WL_2 — Turbulent interaction length in the near wake measured from the trailing edge of the airfoil

WL_{av} — Average value of WL_1 and WL_2

x — Coordinate in the physical plane defining the airfoil chord axis; and a local tangential coordinate in the boundary-layer turbulence model

x_k — The kth coordinate in indicial notation

x_L — Turbulent transition length measured along the body surface

x_p — The x coordinate of a location in the physical plane about which a moment is computed; and a new x coordinate location obtained by the interpolation of adjacent ξ grid lines

LIST OF SYMBOLS (Continued)

<u>SYMBOL</u>

x_R The x coordinate which locates the position of the shear layer reattachment which forms the bubble in the numerical solution

x_t The x coordinate which locates the start of transition to turbulence on the upper airfoil surface in the numerical solution

x_T The x coordinate which locates where fully turbulent flow first occurs downstream of the leading edge on the upper airfoil surface in the numerical solution

XETA   Modified grid transformation metric $x_\eta/2J$

XXI   Modified grid transformation metric $x_\xi/2J$

y Coordinate in the physical plane normal to the airfoil chord; a local normal coordinate in the boundary-layer turbulence model

y_k Computed location of the kth point within the boundary-layer for equal velocity increments in the coordinate attraction method

y_p The y coordinate of a location in the physical plane about which a moment is computed; a new y coordinate location obtained by the interpolation of adjacent ξ grid lines

$y_t(x)$ Airfoil thickness function for NACA four digit airfoil sections

YETA   Modified grid transformation metric $y_\eta/2J$

YXI   Modified grid transformation metric $y_\xi/2J$

z Input axis variable for calculating x coordinates of the final distributed surface points

Z Nondimensional complex variable x+iy in the far field boundary condition model

$\tilde{Z}$ Complex variable c(x+iy) in the far field boundary condition model

α Geometric angle of attack; and a grid transformation coefficient $x_\eta^2 + y_\eta^2$.

LIST OF SYMBOLS (Continued)

SYMBOL

α_L	Geometric angle of attack
α_1	The value $f''(0)$ in the Blasius' series.
β	Grid transformation coefficient $x_\xi x_\eta + y_\xi y_\eta$
γ	Grid transformation coefficient $x_\xi^2 + y_\xi^2$; and the intermittency factor defined in Equation 63
Γ	Clockwise circulation around a body
$\Gamma(x)$	Turbulent transition factor function
δ	Local boundary-layer thickness
δ_w	Local wake half width
δ^*	Local displacement thickness defined by Equation 64
δ_{ji}	Kronecker Delta
Δy_∞	Input displacement in the last two y positions at the outer boundary in the coordinate line attraction method
ϵ	Dissipation rate of turbulent energy
ϵ_i	Inner layer eddy viscosity
ϵ_M	Turbulent eddy viscosity
ϵ_o	Outer layer eddy viscosity
ϵ_w	Wake value of the eddy viscosity
ϵ_{ic}	Inner layer eddy viscosity for comparison in limiting technique
ϵ_{ow}	Far wake eddy viscosity value
η	Coordinate in the computational plane which is used to define the body surface

LIST OF SYMBOLS (Continued)

<u>SYMBOL</u>

η_k	Summation parameter defined as $(k-1)\Delta\eta$
η_p	A selected contour integral path around the body
Θ	Local momentum thickness; and the angular coordinate in complex polar variables
$\Theta(\xi)$	Function which specifies the angle that the incoming ξ lines make with the body surface coordinate
Λ	Transition distance defined as the distance required to vary $\Gamma(x)$ from 1/4 to 3/4
Λ_R	Turbulent reattachment criteria defined as $(\Theta/u_e) \, du_e/ds$
μ	Dynamic viscosity coefficient
μ_D	Potential doublet strength
ν	Kinematic viscosity μ/ρ
ξ	Coordinate in the computational plane which emanates from the body surface grid points and is orthogonal to η in the computational plane
π	Ratio of circumference to diameter of a circle
ρ	Fluid density
σ	Similarity parameter in Blasius' series of Equation 16; and a grid transformation coefficient defined by Equation A-7
σ_B, σ_η	Inner and outer control volume surfaces
τ	Grid transformation coefficient defined by Equation A-8
τ_{ij}	Element of the viscous stress tensor
τ_{tij}	Element of the turbulent stress tensor
τ_{Tij}	Element of the total stress tensor, $\tau_{ij} + \tau_{tij}$
ϕ_d	Transonic small disturbance potential doublet function

LIST OF SYMBOLS (Continued)

<u>SYMBOL</u>

ϕ_v Transonic small disturbance potential vortex function

Φ Acceleration parameter for pressure iteration given by Equation 40 defined as $2\omega_{pb}J^2 / ((\alpha + \gamma)\Delta t)$

ψ Inviscid stream function

ω Magnitude of the local flow field vorticity, curl $\underline{v}$; and a local acceleration parameter

ω_p Acceleration parameter for the field pressure finite difference equations

ω_{pb} Acceleration parameter for the surface pressure iteration

ω_{uv} Acceleration parameter for the u and v velocity component finite difference equations

<u>Subscript</u>

b   Denotes a location on the body surface

e   Denotes a location at the edge of the boundary-layer or wake

f   Denotes a location on the computational far field boundary

i   Denotes the ξ coordinate location in the computational plane for finite difference equations; and an indicial notation index in differential equations

j   Denotes the η coordinate location in the computational plane for finite difference equations; and an indicial notation index in differential equations

k   A component index in indicial notation

max,min   Denote the maximum and minimum values of a variable

S   Denotes a value at the laminar separation point which defines the beginning of the bubble

w   Denotes a value in the wake region

x,xx   Denote differentiation with respect to x

LIST OF SYMBOLS (Concluded)

SYMBOL

y,yy	Denote differentiation with respect to y
$\eta,\eta\eta$	Denote differentiation with respect to η
$\xi,\xi\xi$	Denote differentiation with respect to ξ
___	Denotes a vector quantity

Superscript

$*$	Denotes a quantity in the transformed plane
___	Denotes a turbulence time averaged quantity
$'$	Denotes a turbulent fluctuating quantity
$\sim$	Denotes a temporary nondimensional variable definition
s	Iteration number in the successive-over-relaxation iteration procedure
η	Pertaining to η contours
ξ	Pertaining to ξ contours

Prefix

d	Derivative operator
D	Substantial derivative operator ($D/Dt = \partial-/\partial t + \underline{v}\cdot\underline{\nabla}-$)
Δ	Increment
Σ	Summation
$\underline{\nabla}$	Del-operator defined as $\hat{i}\,\dfrac{\partial}{\partial x} + \hat{j}\,\dfrac{\partial}{\partial y}$
∂	Partial derivative operator

SECTION I

INTRODUCTION

Much effort has been expended by the aeronautical community in determining the aerodynamic characteristics of airfoils. Linear methods are extensively used in design work for studying configurations at small angles of attack with negligible flow separation. Experimental wind tunnel investigations are used to determine the characteristics near stall where separation phenomena become important. Recent developments in numerical techniques have stimulated research on another approach, namely the numerical solution of the Navier-Stokes equations. These equations model the viscous effects which contribute to airfoil stall. For this reason, numerical Navier-Stokes methods offer the possibility of determining the aerodynamic characteristics for airfoils experiencing stall. Numerical methods can also complement experimental methods by efficiently extending the range of parameters under investigation. Furthermore, numerical methods eliminate model support interference and wall interference effects found in wind tunnel testing.

The purpose of this investigation is to develop a numerical Navier-Stokes method that will accurately determine the aerodynamic characteristics of incompressible turbulent viscous flow over two-dimensional airfoils near stall.

The development of a numerical method for turbulent flow requires a suitable technique for distributing points throughout the flow field and a model which describes the behavior of turbulence within specific regions of the flow field. A survey of numerical grid generating techniques and available turbulence models is presented. The quantity of literature concerned with the Navier-Stokes equations is extensive. Therefore a summary of the literature, which describes formulations of the Navier-Stokes equations and their numerical solving techniques applied to flows over airfoils, is given. The research objectives for this work are then discussed, and a summary of the remaining sections is presented.

Body-fitted curvilinear coordinate systems greatly enhance the application of numerical methods to practical boundary value problems involving partial differential equations. The representation of a boundary surface as a coordinate line reduces the difficulties associated with numerically specifying boundary conditions by interpolation in finite difference methods. In the physical (x,y) plane, values for one computational coordinate ξ are specified at selected points on both the body surface and the outer boundary. Constant values for the other computational coordinate η are specified on both the body surface and the outer flow boundary. The transformed computational (ξ,η) plane then becomes a rectangular region with an orthogonal grid. Winslow (Reference 1) and Chu (Reference 2) introduced the concept for two-dimensional regions interior to a closed boundary. Their transformed coordinates are solutions of Laplace's equation in the physical plane and define a triangular mesh system in the physical plane. Amsden and Hirt (Reference 3) took the physical coordinates to be solutions of a modified Laplace's equation in the transformed plane.

Thompson, Thames, and Mastin (References 4,5,6) generalized the method for the automatic generation of body-fitted coordinates for any two-dimensional, multi-connected region. They also introduced the use of forcing functions in a Poisson equation which provides mesh control in regions with large gradients. Hodge (Reference 7) developed an automated grid line attraction method based on boundary-layer theory which determines the coefficients in his forcing function. Hodge assumed a Blasius boundary-layer profile and distributed his grid points at approximately equal velocity increments in the boundary-layer. Steger and Sorenson (Reference 8) introduced auxiliary conditions for the forcing functions which provide angle and distance control at the inner boundary surface. The angle with which a ξ line intersects the body surface is specified by a function $\Theta(\xi)$, and the rate of change of arclength with η on a ξ line at the body surface is prescribed by $s_\eta(\xi)$. Sorenson (Reference 9) later imposed similar conditions on an outer computational boundary. These auxiliary conditions are used to

solve for coefficients in the chosen exponential forcing functions. The geometric conditions hold exactly only in the limit as Δn approaches zero. Sorenson reported that numerical instabilities occur for large changes in the coefficients during successive iterations and for boundaries with sharp corners. He implemented a limit function which damped the change of the value for each coefficient over one iteration; and at sharp corners ne computed average values of each coefficient from data at the neighboring boundary points. Mastin and Thompson (Reference 10) have also extended the elliptic body-fitted coordinate generation technique to three dimensions for simple geometries.

Some other specific grid generation techniques which use properties of elliptic differential equations have also been reported. Meyder (Reference 11) constructed an orthogonal curvilinear coordinate system by using electric field theory. He solved the potential equation twice with different sets of mixed Dirichlet and Neumann boundary conditions for the electric potential and electric force lines, respectively. These solutions, however, were obtained in the physical plane using interpolation and became the curvilinear coordinate lines in the physical plane. The coordinate metrics were then used to formulate a finite difference equation which was also solved in the physical plane. Conformal mapping techniques which employ the Theodorsen-Garrick (Reference 12) transformation have been examined by Ives (Reference 13). He introduced the use of fast Fourier transform methods and developed a new class of transformations which map the flow field of a two-element airfoil onto the region between two concentric circles. Conformal techniques are not capable of being extended to three-dimensional geometries (Reference 4). Neither of these approaches offers a convenient means for mesh control in regions of large flow gradients.

Recently, a geometric grid generation technique has been introduced by Gibeling, Shamroth, and Eiseman (Reference 14). The technique parameterizes (t) the body and outer boundary surfaces and uses a stretching function $R(r)$ for mesh attraction along constructed lines

perpendicular to the body surface. Unit increments for ordered pairs (t,r) generate the corresponding computational plane. Further refinements which provide angle and arclength variation control at a body surface have subsequently been developed by Eiseman (References 15,16,17).

The search for an accurate and universal turbulence model has paralleled the development of body-fitted grid generation techniques. In principle, the Navier-Stokes equations completely describe the turbulent fluctuating fluid motion. The required mesh resolution, necessary to resolve the turbulent eddies with varying length scales, when translated into computer resources presently make this approach unfeasible. Many quantities of engineering interest in turbulent flows involve a mean value taken over a time interval. The time interval is sufficiently long to include many fluctuations while small compared with the characteristic time of the mean flow. The Navier-Stokes equations can then be reformulated using these mean flow variables. This Reynolds averaging procedure introduces the mean of terms involving fluctuating quantities. The Reynolds stress components $-\overline{\rho u_i' u_j'}$ are the most common terms of this type. To solve the averaged form of the Navier-Stokes equations, "turbulence closure" must be achieved by suitably modelling these additional terms. This approach to turbulence has led to models which introduce auxiliary relationships ranging from algebraic equations to several partial differential equations. These models are commonly categorized and are now summarized according to the number of additional partial differential equations which comprise the model.

The algebraic or zero equation models have their origins in Boussinesq's (Reference 18) eddy viscosity hypothesis and Prandtl's (Reference 19) mixing length model. The local turbulent stresses are assumed proportional to the local mean flow strain rates with the proportionality constant defined as an equivalent or eddy viscosity. The eddy viscosity models of Cebeci-Smith (Reference 20), Mellor-Herring (Reference 21), and Patankar-Spalding (Reference 22) represent this approach. The boundary-layer in each method is divided into an inner

near wall layer and an outer wake layer with separate expressions for the eddy viscosity coefficient. In the Cebeci-Smith and Patanker-Spalding models the inner mixing length varies as a linear function of the normal distance from the wall modified with a Van Driest (Reference 23) laminar sublayer correction. The Cebeci and Mellor models both base the outer length scale on the displacement thickness while the Patanker-Spalding model uses the boundary-layer thickness directly. These models have been successfully extended and applied (Reference 24) to a wide variety of boundary-layer flow geometries involving compressibility, heat and mass transfer, and curvature effects. In addition, the mean flow models are computationally efficient. Launder and Spalding (Reference 25) point out that these models predict a vanishing eddy viscosity where the velocity gradient is zero and have not been successful for large separated recirculating flows.

The one equation turbulence model introduced by Prandtl (Reference 26) is an extension of the algebraic technique. In this approach the solution of the partial differential turbulent kinetic energy equation usually provides a local velocity scale given by $q^2 = \overline{u'_i u'_i}$ where summation is implied. The length scale L is prescribed by an algebraic expression as before. Terms involving fluctuating quantities other than q must still be modelled. Glushko (Reference 27), Mellor and Herring (Reference 28), and Wolfshtein (Reference 29) model the gradient diffusion term $-(\overline{(u'_k \, p/\rho\,) + u'_k \, (u'_i \, u'_i\,)}/2)$ with a gradient of q^2 given as $N_Q \, \epsilon_M \, \partial_k \, (q^2/2)$ where N_Q is a specified constant or function and ϵ_M is the eddy viscosity. The Reynolds stress is related to the mean flow as in the algebraic approach except that the eddy viscosity is assumed proportional to qL. Bradshaw, et al (Reference 30) model the gradient diffusion term with an expression $G \, q^2 \, Q_k$ where G is an empirical constant or function and Q_k is a velocity characteristic of large eddy motions. They also write the Reynolds stress directly as a function of q in the form $\tau_{tij} = A_{ij} \, q^2$. In each model the isotropic dissipation is modelled by a form q^3/L. Nee and Kovasznay (Reference 31)

5

use a rate equation for the total viscosity $N = \mu + \epsilon_M$ in place of the

kinetic energy equation. They formulated expressions for the generation
and dissipation terms involving various constants and the length scale.
Launder and Spalding (Reference 25) observe that the one differential
equation models require a moderate increase in computer resources but do
not in general provide more accurate results than the results obtained
from algebraic methods.

Kolmogorov (Reference 32) introduced the somewhat more complex type
of turbulence model which uses two partial differential equations. A
form of the turbulent kinetic energy equation provides a local velocity
scale. The local length scale is obtained from a second equation. Ng
and Spalding (Reference 33) formalized this approach by introducing the
energy-length equation derived by Rotta (Reference 34). They also used
the Glushko closure model in the turbulent energy equation. This class
of two equation models is named the k - kL turbulence model where the
eddy viscosity is proportional to $k^{\frac{1}{2}} L$. Saffman (Reference 35) has used
a transport equation for the mean vorticity ω together with the turbulent
kinetic energy. The eddy viscosity becomes proportional to k/ω in this
k - ω class of closure models for turbulence. The local length scale
is assumed to be proportional to $k^{\frac{1}{2}}/\omega$. Wilcox and Rubesin (Reference
36) have modified this approach for compressible flows and generalized
the constitutive equation. Jones and Launder (Reference 37) use a
transport equation for the rate of dissipation of turbulent energy ϵ
along with the turbulent kinetic energy equation. Glushko type closure
models are assumed for the terms involving fluctuating quantities in
both equations. This k - ϵ class of two equation models has a local

length scale proportional to $k^{3/2}/\epsilon$ with the eddy viscosity proportional
to k^2/ϵ. The two equation models have been applied to various boundary-
layer and free shear layer flows with a variety of constants and closure
models. The two equation models require significant increases in
computational resources and have not led to a model of universal
applicability (References 24,25).

The search for a more general turbulence model has led to the use of
the transport equations for the Reynolds stresses. In this approach the
eddy viscosity concept is discarded. However, closure models are still
required for the terms containing fluctuating quantities other than the
Reynolds stresses. Donaldson (Reference 38) introduces closure models
which express the fluctuating terms as functions of the Reynolds stress
and chosen length scales. Hanjalic and Launder (Reference 39) introduce
closure models which use the Reynolds stress and retain the equations for
turbulent kinetic energy k and turbulent dissipation ε. Only cases with
the simplified two-dimensional boundary-layer approximations have been
investigated. The extensive computational resources and initial state
of development of these models preclude this type of approach from practical
consideration as a turbulence model for a complex flow field computation.

Theoretical turbulence models of further complexity have appeared.
Kolovandin and Votutin (Reference 40) introduced a statistical theory
where additional equations are obtained for other correlations of the
fluctuating quantities. Ferziger (Reference 41) took a meteorological
viewpoint of turbulent flows by numerically simulating large scale eddies
while modeling the small scale structures with an eddy viscosity technique.
This approach is a first step toward numerically solving a turbulent flow
field with the instantaneous equations of motion.

The review of available turbulence models provides the basis for
selecting a suitable approach for use in the numerical solution. The
algebraic and the two equation eddy viscosity models appear to be
realistic choices. As previously reported (Reference 25), the one
equation techniques yield unimproved results compared with algebraic
methods and at additional cost in computer resources. The two equation
methods require the solution of additional partial differential equations.
In these methods, terms involving fluctuating quantities, except the
Reynolds stresses, must still be modelled using additional coefficients.
For these reasons, the simpler algebraic eddy viscosity technique, which
requires considerably less computer resources, is employed. If the
physical phenomena associated with separated adverse pressure gradient

flows can be included in the turbulence model, then the accurate calculation of the aerodynamic characteristics may be accomplished with an algebraic technique.

A survey of the previous research involving numerical solutions of the Navier-Stokes equations for flow over airfoils establishes the prediction level of computational methods and also reviews the numerical algorithms. The grid generation technique and turbulence model employed, when applicable, are also included.

Early numerical solutions of the Navier-Stokes equations for flow over airfoils used the vorticity-stream function formulation with an automated grid generation technique (Reference 4). Walker (Reference 42) applied the method to the laminar flow over a flat plate and compared the numerical solution with Blasius' (Reference 43) solution. Thames (Reference 44) used body-fitted coordinates with the vorticity-stream function approach and solved the Navier-Stokes equations for various bodies in doubly connected regions. He obtained solutions for the flow over airfoils at chord Reynolds numbers less than 10^4. Problems mainly attributed to wall vorticity developed for solutions of airfoils at angle of attack.

Mehta and Lavan (Reference 45) also used a vorticity-stream function method in studying the laminar starting vortex and separation bubbles for impulsively started incompressible laminar flow over a Joukowski airfoil at Reynolds numbers less than 10^4. They used three point backward time differences and centered spatial differences. The computational grid was obtained through a conformal transformation followed by a radial stretching transformation.

Reddy and Thompson (Reference 46) applied an integro-differential, vorticity-velocity field method for the solution of incompressible flow in doubly connected regions. Backward time, centered spatial (BTCS) differences were applied to the Navier-Stokes equations. The difference equations were solved using successive-over-relaxation (SOR) iteration.

They also employed the coordinate mesh attraction technique with a time dependent expanding mesh system. Symmetric airfoils at zero angle of attack with a Reynolds number less than 10^6 were considered. At the higher Reynolds numbers, the calculation of surface vorticity required a large number of grid points on the surface which greatly increased the required computer time. A steady state solution was not obtained.

The vorticity-velocity field formulation has been applied by Sankar and Wu (Reference 47) to the case of incompressible laminar flow about an oscillating airfoil. They used a 12% thick Joukowski airfoil at a Reynolds number of 1000. Triangular finite elements were constructed near the airfoil surface and a rectangular mesh was used away from the airfoil. A conformal transformation was used to map the airfoil in the physical plane onto a unit circle in the computational plane. Sankar and Tassa (Reference 48) investigated this same problem with a compressible flow formulation of the Navier-Stokes equations. They used a conformal transformation followed by an algebraic radial stretching transformation. The alternating-direction-implicit (ADI) finite difference method of Briley and McDonald (Reference 49) was used to obtain solutions for Reynolds numbers less than 10^4 and a Mach number of 0.2. In a separate research effort, Sugavanam and Wu (Reference 50) attempted to use a two equation k-ε turbulence model with a vorticity-velocity formulation. A conformal transformation for a 12 percent thick Joukowski airfoil was used. They experienced difficulties in obtaining a converged solution even after eight hours of CYBER 74 CPU time were expended. Variations for both lift and drag of the order of 50 percent occurred.

The use of the primitive variables of velocity and pressure for incompressible flow was introduced by Harlow and Welch (Reference 51) in the explicit forward time, centered spatial (FTCS) Mark-and-Cell (MAC) method. They included a Poisson equation for pressure which is obtained by taking the divergence of the momentum equation. They also found that the velocity divergence terms in the momentum equations were required for the pressure field calculation. Hirt and Harlow (Reference 52) further developed the method. Hodge (Reference 53) considered the case

9

of laminar incompressible viscous flow for an airfoil at angle of attack.
He used a form of the Thompson, et al (Reference 4) body-fitted grid
transformation and applied an implicit BTCS differencing method to the
Navier-Stokes equations. The system of difference equations was solved
with SOR iteration. Various methods of calculating the pressure field
were investigated. Hodge concluded that the momentum equations should
retain the velocity divergence terms and that a Poisson pressure equation
should be used to satisfy continuity. Ghia, Hankey, and Hodge (Reference
54) applied a Poisson pressure equation and the primitive variables form
of the Navier-Stokes equations to study incompressible driven flow in a
square cavity for Reynolds numbers under 1000. They used an alternating-
direction-implicit (ADI) finite difference technique for the momentum
equations and SOR iteration for the pressure equation. A Neumann boundary
condition derived from the normal component of the momentum equations was
employed to compute the wall pressure.

The Poisson pressure equation has been further examined by Chien
(Reference 55) for internal flows. He observed that the calculation of
pressure by direct integration of the momentum equations can be inaccurate
when large velocity variations are present. He found that forms of the
pressure equation were more suitable for computing the pressure field
near boundaries. Recently, Hodge, et al (Reference 7) applied an implicit
backward time finite difference method with both upwind and centered
spatial differences to the Navier-Stokes equations in primitive variables
form. A Poisson pressure equation was used to obtain a solution for
laminar flow over airfoils at angle of attack with a Reynolds number of
order 10^5. The solution contains a large oscillating separated region
which gives approximate trends in lift but very poor agreement with
available drag data (Reference 56).

Early numerical Navier-Stokes investigations of turbulent flow over
airfoils considered two-dimensional transonic viscous flow at small angles
of attack. Deiwert (Reference 57) applied MacCormack's explicit method
(Reference 58) with a 50x38 rectangular based exponentially stretched

mesh. He used 20 uniformly spaced points to define the upper airfoil surface and imposed the Neumann boundary-layer condition $\partial p/\partial n = 0$ on the surface. Steger (Reference 59) used the implicit Beam-Warming method (Reference 60) with a 71x33 grid obtained from a modified Thompson transformation (Reference 4). He calculated the solution on the branch cut with a linear extrapolation procedure and evaluated surface pressures using the momentum equations for the direction normal to the surface. Walitt, et al (Reference 61) applied the first order method of Trulio (Reference 62) coupled with a boundary-layer technique used near the airfoil leading edge. They used a 130x68 mesh system but did not capture the full suction pressure on the upper surface near the airfoil nose. Each investigation used a Cebeci-Smith (Reference 63) type algebraic eddy viscosity model and the Reynolds averaged compressible Navier-Stokes equations.

Recently, Shamroth and Gibeling (Reference 64) used the Briley-McDonald (Reference 49) implicit finite difference formulation with a constructive type 81x30 grid system to compute turbulent flow over an airfoil at an angle of attack of six degrees and Reynolds number of 10^6. They first tried a two equation k-ε turbulence model but experienced convergence problems near the leading edge and far field flow regions. They reported obtaining large or negative values for the turbulent viscosity in essentially laminar regions. The turbulent kinetic energy equation with an algebraically prescribed length scale was then used. Major discrepancies occurred for the mean pressure distribution solution in the suction peak and trailing edge regions of the airfoil surface. They also noted that the constructive grid technique caused a crossing of grid lines of the same family for highly cambered airfoils.

The examination of existing numerical solutions of the Navier-Stokes equations for two-dimensional flow over airfoils reveals Reynolds number and angle of attack restrictions. As a result, numerical Navier-Stokes methods for the accurate computation of the flow field and resulting aerodynamic characteristics for an airfoil near stall are unavailable.

The development of such a numerical method for solving incompressible two-dimensional turbulent flow over airfoil sections near stall does constitute a significant contribution in computational aerodynamics. The fulfillment of this research goal requires the formulation of an adequate turbulence model for use in both leading and trailing edge separated regions. The far field boundary conditions for incompressible flows must also be examined.

The selection of a suitable numerical approach for incompressible turbulent flows is based on several considerations. An implicit technique is preferred because of the required small grid spacing near the body surface necessary to resolve viscous stresses. Stability criteria of explicit methods would impose a small time step restriction as a result of the grid size. The numerical method should be capable of predicting laminar flow for Reynolds numbers approaching turbulent flow conditions since regions of laminar flow may occur. The use of primitive variables is readily extended to three dimensions and provides for the direct calculation of the pressure field. These criteria are satisfied by an implicit finite difference procedure developed by Hodge (References 53,7) which uses primitive variables and successive-over-relaxation iteration. The implicit finite difference method is employed in this investigation.

The remaining sections of this research effort discuss the techniques employed in achieving the defined research goal. In Section II a form of the Thompson numerically generated body-fitted coordinate system is described. The methods of attracting grid lines to the body surface and distributing surface points are also discussed. The governing equations for incompressible two-dimensional turbulent flow in primitive variables are presented in Section III. Boundary and initial conditions are discussed. An algebraic eddy viscosity turbulence model formulated for adverse pressure gradient separated flows is described. An algebraic type of turbulence model has been chosen because of the previous computational successes for other turbulent flow problems and the definite computational efficiency obtained by this approach. The method for evaluating force coefficients exerted on the body by the flow field is

then discussed. The numerical techniques used in obtaining a solution
are presented in Section IV. First, the finite difference method for
numerically generating the grid is given. The Navier-Stokes equations
are then written in finite difference form. The numerical method used
to implement the boundary and initial conditions is described. The
computational procedure for introducing turbulence is discussed next.
The finite difference and numerical integration techniques for calculating
the force coefficients are then presented. The formal discussion of the
numerical solutions and comparisons with experimental data are given in
Section V. The conclusions derived from this research work and
recommendations for future work are set forth in Section VI.

SECTION II

BODY-FITTED CURVILINEAR COORDINATE SYSTEM

In this section the technique is described which numerically generates body-fitted curvilinear coordinate systems as previously developed by Thompson, Thames, and Mastin (References 4,5). Coordinate lines are attracted to the body surface with a method introduced by Hodge (Reference 7). The distribution of grid points which define the body surface is discussed.

1. TRANSFORMATION

The doubly-connected, two-dimensional region R bounded by closed contours C_b and C_f of arbitrary shape is to be transformed into a rectangular domain R^* as shown in Figure 1. The general transformation from the physical (x, y) plane to the transformed or computational (ξ, η) plane is given by

$$\xi = \xi\ (x,y) \qquad \eta = \eta\ (x,y) \tag{1}$$

The inverse transformation, if it exists, can be expressed as

$$x = x(\xi,\ \eta) \qquad y = y(\xi,\ \eta) \tag{2}$$

The related Jacobian is given as

$$J = x_\xi\ y_\eta - x_\eta\ y_\xi \tag{3}$$

where the subscripts denote differentiation.

The existence of the inverse transformation has been studied by Thames (Reference 44). He showed that if the functions of Equation 1 are continuously differentiable at a point and the Jacobian is nonsingular, then the general transformation has an inverse in a disk about the point.

14

In addition, if the ξ and η transformation functions are harmonic, then a weak maximum principle is obeyed. Then, no extrema will exist in region R and consequently the Jacobian J will not be zero there.

Partial derivatives are transformed using the chain rule and inverse transformation relations. For a sufficiently differentiable function f of x and y, the derivatives transform as follows:

$$f_x = (y_\eta f_\xi - y_\xi f_\eta)/J \tag{4}$$

$$f_y = (-x_\eta f_\xi + x_\xi f_\eta)/J \tag{5}$$

Higher order derivatives are similarly derived.

The system of elliptic coordinate generating equations is chosen to be

$$\xi_{xx} + \xi_{yy} = P(\xi, \eta) \tag{6a}$$

$$\eta_{xx} + \eta_{yy} = Q(\xi, \eta) \tag{6b}$$

with the boundary conditions on curve C_b

$$\xi = \xi_b(x, y) \qquad \eta = \eta_b \tag{7}$$

and on curve C_f

$$\xi = \xi_f(x, y) \qquad \eta = \eta_f \tag{8}$$

where $\xi_b(x, y)$ and $\xi_f(x, y)$ are prescribed functions and η_b and η_f are prescribed constants. The other two sides C_1^* and C_2^* in the rectangular region are transformed from the branch cut $C_1 - C_2$. The functions $x(\xi, \eta)$ and $y(\xi, \eta)$ and all derivatives are continuous

across this cut. These boundary conditions ensure that the body and the far field boundaries are defined by constant η lines. The generalized functions P and Q are utilized in attracting the coordinate lines in various regions.

The rectangular grid system in the transformed plane is used for the computations. The mesh generating system (Equations 6a and 6b) is transformed to the computational plane and becomes

$$\alpha x_{\xi\xi} - 2\beta x_{\xi\eta} + \gamma x_{\eta\eta} = -J^2[x_\xi P(\xi, \eta) + x_\eta Q(\xi, \eta)] \tag{9a}$$

$$\alpha y_{\xi\xi} - 2\beta y_{\xi\eta} + \gamma y_{\eta\eta} = -J^2[y_\xi P(\xi, \eta) + y_\eta Q(\xi, \eta)] \tag{9b}$$

where

$$\alpha = x_\eta^2 + y_\eta^2 \tag{10}$$

$$\gamma = x_\xi^2 + y_\xi^2 \tag{11}$$

$$\beta = x_\xi x_\eta + y_\xi y_\eta \tag{12}$$

The boundary conditions (Equations 7 and 8) similarly become on curve C_b^*

$$x = f_b(\xi, \eta_b) \qquad y = g_b(\xi, \eta_b) \tag{13}$$

and on curve C_f^*

$$x = f_f(\xi, \eta_f) \qquad y = g_f(\xi, \eta_f) \tag{14}$$

The functions f_b, f_f, g_b, and g_f are determined by the known contours C_b and C_f and the functions ξ_b and ξ_f.

2. COORDINATE LINE ATTRACTION

The resolution of viscous terms near the body surface requires a fine mesh spacing in this region. The forcing functions P and Q are used to attract ξ and η lines, respectively. In this work the ξ line spacing is accomplished by specifying the boundary condition function $\xi_b(x, y)$.

The η line spacing is adjusted through the use of the Q function proposed by Thompson (Reference 4) and modified by Hodge (Reference 7).

$$Q(\xi, \eta) = - \sum_{k=1}^{K(\xi)} A_k(\xi) \exp[-D(\xi)|\eta - \eta_k|] \qquad (15)$$

where A_k are the amplification factors, D is the damping factor, K is the number of terms, and $\eta_k = (k - 1)\Delta\eta$. The amplification and damping factors are determined by requiring that the tangential velocity $\bar{u}$ be a linear function of η. In this case, the second and higher order derivatives with respect to η become zero thereby minimizing the truncation error of $\bar{u}$ in the transformed plane.

Hodge (Reference 7) has developed a technique which approximately satisfies the above criterion. The required point distribution on a ξ line is determined using Blasius' flat plate boundary-layer solution. The similarity series solution (Reference 43) is given by

$$f(\sigma) = \sum_{n=0}^{\infty} (-\tfrac{1}{2})^n \frac{C_n \alpha_1^{n+1}}{(3n + 2)!} \sigma^{3n+2} \qquad (16)$$

where the similarity variable $\sigma = y[u_e/\nu x]^{\frac{1}{2}}$. u_e is the edge boundary-layer velocity and ν is the kinematic viscosity. Differentiating Equation 16 with respect to σ gives an expression for the tangential velocity u in the boundary-layer

$$f'(\sigma) = \frac{u}{u_e} = \sum_{n=0}^{\infty} (-\tfrac{1}{2})^n \frac{C_n \alpha_1^{n+1}}{(3n + 1)!} \sigma^{3n+1} \qquad (17)$$

17

The first four coefficients of the Blasius series are $C_0 = 1$, $C_1 = 1$, $C_2 = 11$, and $C_3 = 375$. Also, from Equation 17 the factor α_1 is related to f by $\alpha_1 = f''(0)$ which is 0.33206. Equation 17 is conveniently written as

$$f'(\sigma) - \frac{u}{u_e} = 0 \tag{18}$$

Then, for a given ξ line (which determines x) and a selected number of points in the boundary-layer, values for σ which give equal tangential velocity increments are calculated from Equation 18. The corresponding y distances are computed by using the definition of σ which yields

$$y = \sigma \left[\frac{\nu x}{u_e} \right]^{\frac{1}{2}} \tag{19}$$

These computed y distances become the desired points near the body for the η line intersections with the specified ξ line.

The second part of the boundary-layer grid line attraction technique involves calculating values of A_k and D which when used in Q give the desired η line spacing. Near the body surface, the η transformation equation (Equation 6b) can be written

$$\left(\eta_{yy_b} \right) \overset{\sim}{=} Q(\xi, \eta) \tag{20}$$

where variations with respect to x are neglected. If the expression for the forcing function Q in Equation 15 is substituted into Equation 20, then Equation 20 can be integrated with respect to η to obtain

$$\left(\frac{d\eta}{dy} \right)^2 = \sum_{k=1}^{K} 2(A_k/D) \{ \exp[-D\, H(\eta, \eta_k)] + H(\mathrm{sgn}(\eta_k - \eta),\, 0.)$$

$$[1 - \exp(-D|\eta - \eta_k|)] \} \tag{21}$$

where the difference function H and sgn function are defined as follows

18

$$H(\eta, \eta_k) = \begin{cases} 0 & \text{if } \eta \leq \eta_k \\ \eta - \eta_k & \text{if } \eta > \eta_k \end{cases}$$

$$\text{sgn}(\eta_k - \eta) = \begin{cases} 1 & \text{if } \eta_k - \eta \geq 0 \\ -1 & \text{if } \eta_k - \eta < 0 \end{cases}$$

Now evaluate the expression for $(d\eta/dy)^2$ (Equation 21) at $\eta = 0$ and $\eta = \eta_{max} - \frac{1}{2}\Delta\eta$ which gives the approximate expressions written in Equations 22 and 23, respectively.

$$\frac{1}{2}\left(\frac{d\eta}{dy}\right)^2 \bigg|_{\eta=0} \doteq \frac{1}{D} \sum_{k=1}^{K} A_k \tag{22}$$

$$\frac{1}{2}\left(\frac{d\eta}{dy}\right)^2 \bigg|_{\eta=\eta_{max} - \frac{1}{2}\Delta\eta} \doteq \frac{1}{D}\left(\sum_{k=1}^{K} A_k\right) \exp[-D|\eta_{max} - \frac{1}{2}\Delta\eta - \eta_K|] \tag{23}$$

The derivative in Equation 22 can be evaluated using the y values obtained previously. The derivative in Equation 23 can be specified by choosing an η_{max} based on the placement of the outer boundary. Then Equations 22 and 23 can be combined to give the following equation for the damping factor D:

$$D = \ln\left\{2\left(\frac{d\eta}{dy}\right)^2\bigg|_{\eta=0} \left(\frac{d\eta}{dy}\right)^{-2}\bigg|_{\eta=\eta_{max} - \frac{1}{2}\Delta\eta}\right\} / |\eta_{max} - \frac{1}{2}\Delta\eta - \eta_K| \tag{24}$$

With the damping factor D known, the analytic expression (Equation 21) can be evaluated on each interval of successive y values obtained from the Blasius solution along with the last $\Delta\eta$ interval near the outer boundary. This procedure gives a system of K equations for the K unknowns A_k which are then solved. Therefore, values for the amplification factors and damping factor are obtained at each ξ line which are used to compute a body fitted grid system.

3. BODY SURFACE POINT DISTRIBUTION

The body surface can be defined by either a given set of points or by an analytical expression. The body surface grid points can then be determined by either interpolation or evaluation of the analytical expression.

The NACA 0012 airfoil section is used in this investigation. This airfoil has been used in several investigations (Reference 65) and is an AGARD (Reference 66) designated test airfoil section. The NACA four digit series airfoils have an analytic description of the body surface given by (Reference 67)

$$y_t(x) = 5t\{0.2969x^{\frac{1}{2}} - 0.126x - 0.3516x^2 + 0.2843x^3 - 0.1015x^4\} \qquad (25)$$

where x is the distance along the chord (nondimensionalized by chord), y_t is the upper surface ordinate, and t is the thickness given as a fraction of the chord. For the NACA 0012 airfoil, t = 0.12. The thickness function given by Equation 25 does not close the body at the trailing edge (x=1). A circular arc is used to close the body. The arc is constructed to have a center on the chord line, to have points of tangency with the upper and lower airfoil surfaces near x = 0.99, and to intersect the chord line at x = 1.0.

The distribution of grid points on the airfoil surface is based on both resolving streamwise flow field gradients and defining the surface curvature. These criteria require the clustering of points in the leading edge and trailing edge regions of the airfoil. The following analytic transformation is used to obtain the desired clustered distribution of x abscissa values

$$x = \left\{ \frac{\tanh(\frac{z - A1}{A2}) - \tanh(-\frac{A1}{A2})}{\tanh(\frac{1 - A1}{A2}) - \tanh(-\frac{A1}{A2})} \right\}^{A3} \qquad (26)$$

where z represents the input set of equally incremented values $(0 \le z \le 1)$,

20

x represents the clustered set of abscissae ($0 \leq x \leq 1$), and A1, A2, and A3 are arbitrary constants. The constant A1 determines the center of the hyperbolic function and is used to cluster points toward one end. The constant A2 varies the slope of the function at the center and thus determines the distribution near mid chord. The exponent A3 can also affect the clustering of points at the ends. If A3 > 1, more points occur near x = 0; while if A3 < 1, points are clustered more at x = 1.

SECTION III

GOVERNING EQUATIONS

The time dependent incompressible viscous Navier-Stokes equations for two-dimensional flows are presented. The primitive variables of fluid velocity and pressure are used. The Reynolds averaged Navier-Stokes equations are obtained. Boundary and initial conditions are given. A modified turbulence model based on Prandtl's mixing length theory is described which expresses the Reynolds stresses in terms of mean flow quantities for separated adverse pressure gradient flows. An expression for the force exerted by the flow field on the body is derived. The equations and boundary conditions are transformed by the curvilinear transformation discussed in Section II and written in the computational plane.

1. BASIC EQUATIONS OF MOTION

The time dependent incompressible Navier-Stokes equations, which describe conservation of linear momentum, in orthonormal indicial notation are given by

$$\rho \{ \frac{\partial V_i}{\partial t} + \partial_j (V_j V_i) \} = -\partial_i p + \partial_j \tau_{ji} \tag{27}$$

where ρ is the fluid density, p is the fluid static pressure, V_i are the components of fluid velocity, and τ_{ji} is the viscous stress tensor. The subscript $i = 1$ corresponds to the x direction and $i = 2$ to the y direction. Conservation of mass for an incompressible flow is given by

$$\partial_j V_j = 0 \tag{28}$$

Turbulent flow is introduced by assuming that the flow quantities can be described in terms of mean and fluctuating quantities in the form

$$V_i = \overline{V}_i + V_i' \qquad\qquad p = \overline{p} + p' \qquad\qquad \tau_{ji} = \overline{\tau}_{ji} + \tau'_{ji}$$

22

where the bar (-) indicates a mean quantity and the prime (') indicates a fluctuating quantity. In this form, a time average of a fluctuating quantity is assumed to be zero. Substitute these expressions into Equations 27 and 28 and time average each equation to obtain the Reynolds averaged Navier-Stokes equations for two-dimensional incompressible turbulent flow given below.

$$\rho\{\frac{\partial \overline{V}_i}{\partial t} + \partial_j(\overline{V}_j \overline{V}_i)\} = -\partial_i\overline{p} + \partial_j\{\overline{\tau}_{ji} - \rho \overline{V'_j V'_i}\} \quad (29)$$

$$\partial_j \overline{V}_j = 0 \quad (30)$$

The term $-\rho \overline{V'_j V'_i}$ is known as the turbulent Reynolds stress. The incompressible form of the constitutive equation which relates the stress as a function of the rate of strain is now introduced as

$$\overline{\tau}_{ji} = \mu(\partial_j \overline{V}_i + \partial_i \overline{V}_j) \quad (31)$$

where μ is the dynamic viscosity coefficient. The turbulent Reynolds stress is similarly modelled with an algebraic eddy viscosity approach based on Prandtl's mixing length theory. The corresponding expression is

$$- \rho\overline{V'_j V'_i} = \varepsilon_M(\partial_j \overline{V}_i + \partial_i \overline{V}_j) \quad (32)$$

where ε_M is the turbulent eddy viscosity. In this way, the additional unknown $-\rho\overline{V'_j V'_i}$ is expressed in terms of the mean flow variables. This turbulence closure requires an expression for the eddy viscosity. Models for the eddy viscosity are examined in Section III.3.

The expressions for the viscous laminar and turbulent stresses, (Equations 31 and 32) are substituted into Equation 29 to obtain the

simplified turbulent incompressible Navier-Stokes equations

$$\frac{\partial \overline{V}_i}{\partial t} + \partial_j(\overline{V}_j \, \overline{V}_i) = -\frac{1}{\rho} \partial_i \, \overline{p} + \frac{(\mu + \epsilon_M)}{\rho} \{\partial_j \partial_j \, \overline{V}_i + \partial_i \, \partial_j \, \overline{V}_j\} \qquad (33)$$

The following nondimensional variables are introduced:

$$\tilde{x}_i = \frac{x_i}{c} \quad , \quad \tilde{V}_i = \frac{\overline{V}_i}{U_\infty} \quad , \quad \tilde{p} = \frac{\overline{p} - p_\infty}{\rho \, U_\infty^2} \quad , \quad \tilde{t} = \frac{t U_\infty}{c} \qquad (34)$$

where c is the airfoil chord, U_∞ is the freestream velocity, and p_∞ is the freestream static pressure. Substituting these nondimensional variables into Equations 30 and 33, with the time average and nondimensional symbols understood, gives the following set of equations

$$D = \partial_j \, V_j = 0 \qquad (35)$$

$$\frac{\partial V_i}{\partial t} + \partial_j(V_j V_i) = -\partial_i \, p + \frac{1}{Re_t} (\partial_j \partial_j V_i + \partial_i \partial_j V_j) \qquad (36)$$

where D is the divergence of velocity and Re_t is the turbulent Reynolds number. The turbulent Reynolds number is defined as

$$Re_t = \frac{Re}{1 + \dfrac{\epsilon_M}{\mu}} \qquad (37)$$

where $Re = \rho U_\infty c/\mu$, the Reynolds number.

Another simplification would be to apply Equation 35 into Equation 36. The divergence D is contained in both the convective and viscous terms. Although analytically correct, the velocity divergence is in

24

general not identically zero in a numerical result. The approach used by Hodge (Reference 53) and developed by Harlow and Welch (Reference 51) is to keep the divergence D in the convective term as a correction term. This approach is used here so that the viscous divergence term is set equal to zero in Equation 36. Since the convective term is important throughout the flow field while the viscous term is important only near the airfoil surface, it appears reasonable to drop the viscous divergence term and keep the convective divergence term as a correction term. Thus, the appropriate set of equations becomes

$$\frac{\partial V_i}{\partial t} + \partial_j (V_j V_i) = - \partial_i p + \frac{1}{Re_t} (\partial_j \partial_j V_i) \tag{38}$$

$$D = \partial_j V_j \tag{39}$$

The calculation of pressure in the primitive variables formulation must be carefully handled. The pressure does not appear in the continuity equation nor does a time derivative of pressure occur. Two approaches have been extensively used to overcome this difficulty. Both techniques compute the pressure by utilizing the velocity divergence D as a correction factor. The calculated pressure is made to satisfy continuity. The first method, introduced by Chorin (Reference 68), computes pressure using an iteration procedure with D as the correcting term. The expression is

$$p^{(s+1)} = p^{(s)} - \Phi D \tag{40}$$

where s denotes the iteration number and Φ is an acceleration parameter which can be either a constant or can be related to a successive-over-relaxation (SOR) solution of a Poisson equation for pressure as shown by Hodge (Reference 53). The second method uses a Poisson equation for pressure derived from the divergence of the momentum equation expressed

25

in Equation 38. The form of the equation is shown in Equation 41.

$$D_t = \nabla \cdot \underline{R} - \nabla^2 p \qquad (41)$$

where $\underline{R}$ represents the convective and viscous terms. If the $\underline{R}$ expression is algebraically simplified with D used wherever possible, the following simplified incompressible Poisson pressure equation is obtained

$$D_t = - \{ (uD)_x + (vD)_y + u_x^2 + 2v_x u_y + v_y^2 + uD_x + vD_y \}$$

$$+ \frac{1}{Re_t} (D_{xx} + D_{yy}) - (p_{xx} + p_{yy}) \qquad (42)$$

This equation contains both spatial and time derivatives of the velocity divergence as well as the fluid velocities and pressure. Again, continuity is used as a correcting factor for calculating pressure. Further simplification can occur if small variations in the velocity divergence are assumed. In this case, the spatial derivatives of D are set to zero in Equation 42 and the result becomes

$$D_t + (u_x^2 + 2v_x u_y + v_y^2) = - (p_{xx} + p_{yy}) \qquad (43)$$

Hodge (Reference 53) used both Equations 42 and 43 and found no apparent difference in the flow field solutions for his case of laminar flow. Also, Chorin's method of Equation 40 is related to the pressure Equation 43. Hodge (Reference 53) showed that the Chorin technique is approximately related to a solution of the Poisson pressure equation using SOR iteration on a coarse grid of twice the spacing. The Poisson pressure equation technique is chosen for the interior flow field because of the increased coupling which occurs in a finite difference representation. However, the body surface pressure is calculated using the iteration technique of Equation 40. Here mass conservation is imposed directly and the difficulty of evaluating the Laplacian of pressure at the body surface in Equation 43 is avoided.

The following set of equations taken from Equations 38, 39, and 43 becomes the system used for the solution of incompressible turbulent viscous two-dimensional flow over airfoils:

$$u_t + uu_x + vu_y + uD = -p_x + \frac{1}{Re_t}(u_{xx} + u_{yy}) \tag{44}$$

$$v_t + uv_x + vv_y + vD = -p_y + \frac{1}{Re_t}(v_{xx} + v_{yy}) \tag{45}$$

$$D_t + u_x^2 + 2v_x u_y + v_y^2 = -(p_{xx} + p_{yy}) \tag{46}$$

$$D = u_x + v_y \tag{47}$$

The numerical solution of the governing equations is obtained by performing the computations in the computational plane obtained with the curvilinear transformation discussed in Section II. This method requires that *the equations are transformed to the computational plane*. The governing equations (Equations 44 through 47) are transformed using the relations given in Section II and Appendix A. The resulting set of corresponding transformed equations becomes:

$$u_T + \frac{u}{J}(y_\eta u_\xi - y_\xi u_\eta) + \frac{v}{J}(x_\xi u_\eta - x_\eta u_\xi) + uD =$$

$$- \frac{1}{J}(y_\eta p_\xi - y_\xi p_\eta) + \frac{1}{Re_t}\left\{\frac{(\alpha u_{\xi\xi} - 2\beta u_{\xi\eta} + \gamma u_{\eta\eta})}{J^2}\right.$$

$$+ u_\eta(\frac{\sigma}{J^2}) + u_\xi(\frac{\tau}{J^2})\} \tag{48}$$

$$v_T + \frac{u}{J}(y_\eta v_\xi - y_\xi v_\eta) + \frac{v}{J}(x_\xi v_\eta - x_\eta v_\xi) + vD =$$

$$- \frac{1}{J}(x_\xi p_\eta - x_\eta p_\xi) + \frac{1}{Re_t}\left\{\frac{(\alpha v_{\xi\xi} - 2\beta v_{\xi\eta} + \gamma v_{\eta\eta})}{J^2}\right.$$

$$+ v_\eta(\frac{\sigma}{J^2}) + v_\xi(\frac{\tau}{J^2})\} \tag{49}$$

$$D_T + \frac{1}{J^2} \{ (y_\eta u_\xi - y_\xi u_\eta)^2 + 2(y_\eta v_\xi - y_\xi v_\eta)(x_\xi u_\eta - x_\eta u_\xi)$$

$$+ (x_\xi v_\eta - x_\eta v_\xi)^2 \} = - \{ \frac{\alpha p_{\xi\xi} - 2\beta p_{\xi\eta} + \gamma p_{\eta\eta}}{J^2}$$

$$+ p_\eta (\frac{\sigma}{J^2}) + p_\xi (\frac{\tau}{J^2}) \} \tag{50}$$

$$D = (y_\eta u_\xi - y_\xi u_\eta) + (x_\xi v_\eta - x_\eta v_\xi) \tag{51}$$

2. BOUNDARY AND INTIAL CONDITIONS

The complete definition of the flow problem requires the specification of sufficient boundary and initial conditions. The Navier-Stokes equations are coupled, nonlinear, first order in time, second order in space, elliptic partial differential equations. The elliptic nature of the equations for velocity requires boundary conditions at each boundary. The first order derivatives of pressure require a boundary condition describing the free-stream pressure. The time derivative terms require initial conditions on velocity and pressure throughout the flow field.

Boundary conditions on the airfoil surface are considered `rst. The continuum no slip boundary condition for a viscous fluid at a stationary solid surface is imposed on the tangential velocity at the surface. In addition, the normal component of velocity must be zero for a stationary surface with no transpiration. These conditions are met by the specification of the Dirichlet boundary conditions

$$u_b = 0 \qquad\qquad v_b = 0 \tag{52}$$

where the subscript b denotes body surface. The pressure on the airfoil surface is computed, and no body boundary condition is required by the first derivative pressure terms.

The far field boundary conditions for velocity and pressure specify the freestream flow field. Let $\underline{r}$ be a position vector in the flow field with the origin at the airfoil mid-chord. Then, as the distance $|\underline{r}|$ from the airfoil becomes large the fluid velocity and pressure approach their nondimensional freestream values as follows:

$$\lim_{|\underline{r}| \to \infty} (u\hat{i} + v\hat{j}) = \cos \alpha \; \hat{i} + \sin \alpha \; \hat{j} \tag{53}$$

$$\lim_{|\underline{r}| \to \infty} p = 0 \tag{54}$$

where α is the angle of attack of the airfoil chord with respect to the freestream.

The first order time derivative terms require initial conditions for the velocity and pressure in the field. From a theoretical viewpoint, since the asymptotic steady solution is desired, any continuous initial specification of velocity and pressure (subject to the prescribed boundary conditions) is permissible.

The boundary conditions and initial conditions are also transformed to the computational plane. The values for each condition remain unaltered and are thus not repeated here. The location in the transformed plane depends on the specific transformation chosen to generate the computational grid. This matter is discussed in Section IV where the numerical procedures are described. The sensitivity analysis of the outer boundary location is addressed in Appendix F.

3. TURBULENCE MODEL

Turbulence modelling is of considerable interest in theoretical, experimental, and computational research work. Many aerodynamic problems

29

of practical interest contain regions of turbulent flow. Several models
have been developed which vary in complexity from Prandtl's mixing length
theory to techniques employing auxiliary differential equations for mixing
lengths, viscosity coefficients, and turbulent kinetic energies. The
accuracy of each model varies with both the geometry and the flow field
quantity used for comparing results. In computational work, the ability
to translate the turbulence model into numerical procedures and the computer
resources required are additional factors which need to be considered.

In this investigation, turbulence is modelled with an algebraic eddy
viscosity approach based on Prandtl's mixing length theory. The basic
concept of this method is that the turbulent Reynolds stresses, $-\rho \overline{V_j' V_i'}$,
can be related to the strain rate of the mean flow in a way analogous to
that for laminar viscous stresses. The fundamental expression was previously
introduced in Equation 32 to obtain the simplified turbulent incompressible
Navier-Stokes equation (Equation 33). The algebraic eddy viscosity has
been used extensively in obtaining numerical solutions for a variety of
aerodynamic problems (References 24,25,69).

The eddy viscosity model for turbulent flow with zero pressure gradient
near a solid surface, which incorporates the modifications of Cebeci and
Smith (Reference 63), Van Driest (Reference 23), and Deiwert (Reference
57), is given below and then discussed.

$$\epsilon_i = \rho (k_1 y D_L)^2 (u_y^{-2} + v_x^{-2})^{\frac{1}{2}} \tag{55}$$

$$\epsilon_o = \rho k_2 \bar{u}_e \delta^* \gamma \tag{56}$$

$$D_L = 1 - \exp\left\{-\frac{y}{\nu A} \left(\frac{|\bar{\tau}_b|}{\rho}\right)^{\frac{1}{2}}\right\} \tag{57}$$

$$\gamma = \{1 + 5.5 (y/\delta)^6\}^{-1} \tag{58}$$

$$\delta^* = \int_0^\delta \left(1 - \frac{\bar{u}}{\bar{u}_e}\right) dy \tag{59}$$

30

The tangential surface direction is given by x and the normal surface direction by y. The inner and outer eddy viscosities, ϵ_i and ϵ_o, model the Law of the Wall and Law of the Wake (Reference 70) regions. The inner mixing length is assumed proportional to the distance y from the surface. k_1 is the Von Karman constant. The Van Driest (Reference 23) damping factor models the laminar sublayer region where τ_b is the surface shear stress and A^+ is the decay constant. The displacement thickness δ^* defined by Equation 59 is the outer layer length scale. The intermittency factor γ, defined in Equation 58, models the decrease of the turbulence intensity from a fully turbulent region to the inviscid region away from the body surface. The intermittency is a function of the normal distance from the wall nondimensionalized by the local boundary-layer distance δ. The local edge boundary-layer velocity u_e is the outer layer characteristic velocity. The standard Cebeci-Smith (Reference 63) values for the constants are k_1 = .41, k_2 = .0168, and A^+ = 26. Continuity of the eddy viscosity distribution is achieved by switching from the inner to the outer model whenever ϵ_i first exceeds ϵ_o.

Recently, Jobe and Hankey (Reference 71) compared this eddy viscosity model given by Equations 55 through 59 with experimental data for several constant adverse pressure gradient attached flows. They varied the k_1, k_2, and A^+ parameters in a numerical turbulent boundary-layer program until the solutions matched the experimental boundary-layer velocity profiles and skin friction coefficients. These parameters had substantially different values than the previously cited values obtained for zero pressure gradient flows. They found that when the flow encounters an adverse pressure gradient the inner eddy viscosity parameters rapidly adjust to the values of k_1 = .65 and A^+ = 52. The outer eddy viscosity constant appears to linearly increase with distance measured from the start of the adverse pressure gradient. Thus, Jobe and Hankey (Reference 71) found that k_2 can vary from a value of .0168 to values of .03 or greater given that the adverse pressure gradient exists for a sufficient length downstream.

The use of an eddy viscosity model similar in form to the one given in Equations 55 through 59 for an airfoil at angle of attack requires examination of the typical flow field characteristics. The upper surface of the airfoil has a pressure distribution which includes a region of low pressure, the suction peak, near the airfoil leading edge. The suction peak is followed by an adverse pressure gradient region. The pressure gradient tends to decrease as the flow recovers toward the trailing edge. The turbulence model that is used for an upper surface turbulent boundary-layer should include the effects of this adverse pressure gradient. The inner eddy viscosity parameters take on the Jobe and Hankey (Reference 71) values of $k_1 = .65$ and $A^+ = 52$ in this region. The outer eddy viscosity parameter k_2 may also change in the adverse pressure gradient region.

However, the rate of change is affected by the pressure gradient and downstream distance. The pressure gradient does decrease rapidly as the flow proceeds downstream. Any tendency for k_2 to increase is probably offset by the decreasing adverse pressure gradient. Thus, the value of k_2 is kept at the equilibrium value of .0168.

The eddy viscosity model with the discussed adverse pressure gradient modifications is now written in terms of the nondimensional variables introduced in Equations 34 and 37. All length quantities are nondimensionalized with respect to the airfoil chord. The mean and nondimensional quantities are henceforth implied. The eddy viscosity model becomes

$$\frac{\varepsilon_i}{\mu} = (k_1 y D_L)^2 \, (u_y^2 + v_x^2)^{\frac{1}{2}} \, Re \tag{60}$$

$$\frac{\varepsilon_o}{\mu} = k_2 u_e \delta^* \, Re \tag{61}$$

$$D_L = 1 - \exp \left\{ -\frac{y}{A^+} \, (|u_{yb}| Re)^{\frac{1}{2}} \right\} \tag{62}$$

$$\gamma = \{1 + 5.5 \, (y/\delta)^6\}^{-1} \tag{63}$$

$$\delta^* = \int\limits_0^\delta \left(1 - \frac{u}{u_e}\right) dy \tag{64}$$

where k_1, k_2, and A^+ are considered adverse pressure gradient parameters.

The eddy viscosity model must also represent the physical characteristics in large separated regions which occur during airfoil stall. Trailing edge stall occurs when the turbulent boundary-layer separation moves toward the leading edge of the airfoil as the angle of attack increases. The pressure distribution in a trailing edge separated region has small gradients (Reference 72). This observation motivates another change to the eddy viscosity model. The inner eddy viscosity parameter is relaxed back toward the equilibrium value of .41. The separation point, which precedes the return to zero pressure gradient, is selected as the point to start the exponential decay. The following relaxation form with distances nondimensionalized by the chord is used

$$f = A\{1 + B \exp(-\frac{s - s_d}{s_r})\} \qquad s \geq s_d$$

$$f = 1 \qquad\qquad\qquad\qquad s < s_d \tag{65}$$

where f is the relaxation factor which multiplies the initial value of k_1^2, k_{1i}^2, s is the distance downstream from the trailing edge separation point, s_d is the delay distance, s_r is the relaxation distance, and A and B are constants. The constants A and B are determined by applying the conditions $f = 1$ at $s = s_d$ and $f = k_{1f}^2/k_{1i}^2$ as s approaches infinity where k_{1f} is the asymptotic value of k_1 downstream. Thus, A and B become

$$A = k_{1f}^2/k_{1i}^2 \qquad\qquad B = A^{-1} - 1 \tag{66}$$

Measurements of Bachalo (Reference 73) and Baker (Reference 74) in the trailing edge separation region indicate the presence of a lower but finite turbulent intensity when compared with the separated turbulent shear layer. The velocity derivative terms in the inner eddy viscosity and damping factor expressions (Equations 60 and 62) can approach zero in a region near a velocity inflection point. In this case, a zero eddy viscosity is permitted in a turbulent separated region which is contrary to the apparent flow structure. This same zero eddy viscosity behavior can also occur in the case of shedding separation bubbles from the airfoil surface. In order to prevent the appearance of laminar regions within the turbulent, adverse pressure gradient, separated flow field during airfoil stall, a limiting technique is employed. The inner eddy viscosity is prevented from decreasing in value as the normal distance from the surface increases. This restriction simulates the uniform turbulent intensities measured (References 73,74) in the trailing edge separated region. The inner eddy viscosity is further limited by imposing a condition of no decrease in the downstream direction. This limit provides for a finite turbulent intensity in separated regions which may develop in the turbulent boundary layer. The limit is initiated by obtaining the distribution of eddy viscosity in the attached boundary-layer near the leading edge of the airfoil. This distribution ε_{ic} is compared with the distributions calculated by the model at downstream locations. The outer eddy viscosity, which has no velocity derivative, is not limited in any way. The "limiting" technique is passive in the sense that the locally computed value for the inner eddy viscosity is used whenever possible. Numerical experiments without the "limiting" technique displayed unphysical results because the conventionally modelled eddy viscosity is divergent. The inception of separated flow decreased the eddy viscosity thereby causing futher separation. The "limiting" concept is necessary to prevent this unphysical result.

The transition from laminar flow to fully turbulent flow is modelled using the transition model of Dhawan and Narasimha (Reference 75). The expression for the transition factor Γ is given below

$$\Gamma = 1 - \exp\{- .412(\frac{x - x_t}{\Lambda})^2\} \tag{67}$$

where x is the tangential direction coordinate on the body surface, x_t is the location where transition starts, and $\Lambda = x_{\Gamma=3/4} - x_{\Gamma=1/4}$ defines the distance required to proceed from $\Gamma = 1/4$ to $\Gamma = 3/4$.

Some of the expressions in the turbulent boundary-layer eddy viscosity model are conveniently expressed in terms of quantities in the transformed plane described in Section II. The velocity derivatives in the inner eddy viscosity model are formulated by determining the tangential and normal components of velocity, $\bar{u}$ and $\bar{v}$ respectively, to the body surface $\eta = \eta_1$ at a position ξ

$$\bar{u}(\xi, \eta) = c_2 u(\xi, \eta) - c_1 v(\xi, \eta) \tag{68}$$

$$\bar{v}(\xi, \eta) = c_1 u(\xi, \eta) + c_2 v(\xi, \eta) \tag{69}$$

where c_1 and c_2 are components of the unit outward normal to the body surface at position (ξ, η_1) given by

$$c_1 = -y_\xi/\sqrt{\gamma} \qquad\qquad c_2 = x_\xi/\sqrt{\gamma}$$

Then, the directional derivative definition is used to obtain the surface normal derivative of $\bar{u}$ and the surface tangential derivative of $\bar{v}$ expressed as

$$\frac{\partial \bar{u}}{\partial n} = \{c_1(y_\eta \bar{u}_\xi - y_\xi \bar{u}_\eta) + c_2(x_\xi \bar{u}_\eta - x_\eta \bar{u}_\xi)\}/J \tag{70}$$

$$\frac{\partial \tilde{v}}{\partial s} = \{c_2(y_\eta \tilde{v}_\xi - y_\xi \tilde{v}_\eta) - c_1(x_\xi \tilde{v}_\eta - x_\eta \tilde{v}_\xi)\}/J \tag{71}$$

which correspond to the u_y and v_x derivatives of the Cartesian eddy viscosity model expressions (Equations 60 through 64).

The turbulence structure in the far wake is modelled with an eddy viscosity expression similar to the outer eddy viscosity model in the turbulent boundary-layer. The model is based on the assumption of a self-preserving, equilibrium turbulent wake with constant pressure in incompressible flow. The approach has been experimentally investigated by Narasimha and Prabhu (Reference 76) who obtained the following expression

$$\varepsilon_w = \rho k_3 w_0 \delta_w \tag{72}$$

where $w_0(x) = \max \{U_\infty - u(x,y)\}$ is the maximum velocity defect in the wake, δ_w is a half wake width defined where the velocity defect becomes one half the maximum value, and k_3 is a constant equal to .065. If the experimentally integrated value of the wake defect function is used, then Equation 72 can be written in terms of the parameters of edge velocity and displacement thickness similar to boundary-layers as follows:

$$\frac{\varepsilon_w}{\mu} = k_3 u_e \delta_w^* Re \tag{73}$$

where u_e is the nondimensional velocity at the edge of the wake, δ_w^* is the nondimensional displacement thickness for the half wake as defined by Equation 64, and k_3 becomes .0634. This expression has been utilized by Green, et al (Reference 77) in an integral method for predicting two-dimensional incompressible and compressible turbulent wakes of lifting airfoils. For an incompressible, constant pressure wake the momentum integral equation reduces to a statement that the momentum thickness is a constant. These conditions exist in the far wake of an airfoil. In addition, in the far

36

wake the displacement and momentum thicknesses become equal as shown by
the experimental results of Narasimha and Prabhu (Reference 76). Thus
the far wake eddy viscosity is approximately constant. The transition
in the wake from the turbulent core region to the inviscid freestream
region on each side of the wake is modelled with the intermittency factor
of Equation 63 where δ is now the wake half width and y is the normal
distance from the wake center.

The turbulent near wake region mixing rates where the wall boundary-
layers merge and eventually become the far wake are not well understood
from either an analytical or experimental viewpoint. In the flow regime
under consideration, a laminar boundary-layer from the lower airfoil surface
mixes with a turbulent boundary-layer from the upper surface. An eddy
viscosity model similar to that used in the outer turbulent boundary-layer
and the far wake is used. Inouye, et al (Reference 78) applied the
Cebeci-Smith (Reference 63) outer layer model in the near wake of a flat
plate and obtained good agreement for the mean velocity profiles. They
allowed the constant k_2 to reach twice the equilibrium value of .0168
over a length of one chord from the trailing edge. The computed eddy
viscosity was still about 50% low when compared with experiment at the
one chord distance. Later, Burggraf (Reference 79) compared several
turbulence models for various near wake flows and concluded that the
Cebeci-Smith model adequately predicted the mean velocity profiles.

The merging of the upper and lower surface boundary-layers is modelled
with a simplified interaction hypothesis approach introduced by Bradshaw
(Reference 80). The two layers are initially allowed to develop downstream
a distance WL_1 without interaction. At this point the eddy viscosity is
increased exponentially in the adjacent laminar boundary-layer from a

zero value to the far wake calculated value ε_{ow} at a distance WL_2 from the trailing edge. This eddy viscosity variation is formulated as follows

$$\varepsilon = 1/2\, \varepsilon_{ow} \{1 + \tanh (8\, \frac{s - WL_{av}}{WL_2 - WL_1})\} \qquad s > WL_1$$

$$\varepsilon = 0 \qquad\qquad\qquad\qquad\qquad\qquad s \leq WL_1 \qquad (74)$$

where WL_{av} is the distance from the trailing edge to a location half way between the distances WL_1 and WL_2 and s is the local distance from the trailing edge. The coefficient 8 is selected so that $\varepsilon \approx 0$ at $s = WL_1$ and $\varepsilon \approx \varepsilon_{ow}$ at $s = WL_2$ because at $s = WL_2$ the hyperbolic tangent function becomes equal to 0.9993 while at $s = WL_1$ it becomes - 0.9993. The eddy viscosity profile in the turbulent boundary-layer near the trailing edge is extended into the near wake.

4. FORCE COEFFICIENTS

The force which is exerted on the body by the moving fluid around the body can be determined from the Cauchy integral equation for conservation of linear momentum applied at the body surface or on a closed path surrounding the body. The basic expressions for the force coefficients formulated in the (x,y) physical plane coordinate system are given by Equations D-12a and D-12b derived in Appendix D for an incompressible turbulent viscous flow.

Consider first the body surface where the components of velocity are identically zero from the no slip boundary conditions. In this case, the equations become

$$C_{fx} = \int_{S_b} \{- 2n_1 p + \frac{1}{Re} (4n_1 \frac{\partial u}{\partial x} + 2n_2 (\frac{\partial u}{\partial y} + \frac{\partial v}{\partial x}))\}\, ds \qquad (75)$$

$$C_{fy} = \int_{S_b} \{-2n_2 p + \frac{1}{Re} (2n_1 (\frac{\partial u}{\partial y} + \frac{\partial v}{\partial x}) + 4n_2 \frac{\partial v}{\partial y})\}\, ds \qquad (76)$$

where the integration is over the body contour denoted by S_b. The first

term in each expression is the contribution caused by pressure forces while the second term is the viscous stress contribution.

The force coefficients (Equations 75 and 76) determined at the body surface can be transformed to the computational plane by using the relations for the outward normal vector to an η contour, line integrals and derivatives given in Appendix A. The transformed equations become

$$C_{fx} = 2 \int_{\xi_{min}}^{\xi_{max}} \{y_\xi p + \frac{1}{ReJ} (\gamma u_\eta + y_\xi(y_\xi u_\eta - x_\xi v_\eta))\} d\xi \tag{77}$$

$$C_{fy} = 2 \int_{\xi_{min}}^{\xi_{max}} \{-x_\xi p + \frac{1}{ReJ} (\gamma v_\eta - x_\xi(y_\xi u_\eta - x_\xi v_\eta))\} d\xi \tag{78}$$

where the no slip boundary condition which implies $u_\xi = v_\xi = 0$ on the body surface is used. The viscous stress terms are further simplified by using continuity at the body surface and the vorticity ($\vec{\nabla} \times \underline{v}$) Equation A.14 on the body surface to obtain

$$C_{fx} = \int_{\xi_{min}}^{\xi_{max}} \{2y_\xi p - \frac{2x_\xi \omega}{Re}\} d\xi \tag{79}$$

$$C_{fy} = \int_{\xi_{min}}^{\xi_{max}} \{-2x_\xi p - \frac{2y_\xi \omega}{Re}\} d\xi \tag{80}$$

where the vorticity on the body surface ω is given by

$$\omega = - (y_\xi v_\eta + x_\xi u_\eta)/J \tag{81}$$

The corresponding moment (positive counterclockwise) about a point P located within the body cross-section with coordinates (x_p, y_p) is given as

$$C_{MP} = \int_{\xi_{min}}^{\xi_{max}} \{(x - x_p)(-2x_\xi p - \frac{2y_\xi \omega}{Re}) - (y - y_p)(2y_\xi p - \frac{2x_\xi \omega}{Re})\}d\xi \quad (82)$$

Next consider again the more general case of a closed path around the body whose force coefficients are given by Equations D-12a and D-12b. Assume that the closed path is an η contour. Then, using the transformed expressions in Appendix A for the outward normal vector to an η contour, integrals, and derivatives, the force coefficients for the body in terms of quantities on a constant η_p line in the flow field become

$$C_{fx} \int_{\xi_{min}}^{\xi_{max}} \{2y_\xi p + \frac{2}{Re_t J} [u_\eta(x_\xi^2 + 2y_\xi^2) - u_\xi(x_\xi x_\eta + 2y_\xi y_\eta) + v_\xi(x_\xi y_\eta)$$

$$-v_\eta(x_\xi y_\xi)] + 2u(uy_\xi - vx_\xi)\} \, d\xi - \frac{\partial}{\partial t} \int_{\eta_b}^{\eta_p} \int_{\xi_{min}}^{\xi_{max}} 2u|J|d\xi d\eta \quad (83)$$

$$C_{fy} \int_{\xi_{min}}^{\xi_{max}} \{-2x_\xi p + \frac{2}{Re_t J} [v_\eta(2x_\xi^2 + y_\xi^2) - v_\xi(2x_\xi x_\eta + y_\xi y_\eta) + u_\xi(x_\eta y_\xi)$$

$$- u_\eta(x_\xi y_\xi)] + 2v(uy_\xi - vx_\xi)\} \, d\xi - \frac{\partial}{\partial t} \int_{\eta_b}^{\eta_p} \int_{\xi_{min}}^{\xi_{max}} 2v|J|d\xi d\eta \quad (84)$$

where $\eta_b \le \eta_p \le \eta_{max}$. The terms in the line integral represent in order pressure forces, viscous forces, and convective outflows of linear momentum. The area integral term is the time rate of increase of linear momentum contained in the control volume bounded by the body η_b contour and the selected η_p contour.

The corresponding lift and drag coefficients are then calculated using Equations D-13 and D-14.

40

SECTION IV

NUMERICAL METHOD

The numerical methods used to obtain solutions for incompressible
turbulent flow over airfoils are presented. The numerical finite difference
procedure which yields the grid transformation is first discussed. The
implicit finite difference method for obtaining approximate solutions to
the unsteady, incompressible, turbulent Navier-Stokes equations is next
described. Numerical boundary conditions and initial conditions are con-
sidered. The numerical procedure for incorporating the turbulent eddy
viscosity model is discussed. The computation of the force coefficients
on the body is then presented.

1. GRID TRANSFORMATION

The numerical solution of the governing equations for the transforma-
tion is carried out in the transformed or computational plane on a square
mesh (ξ, η) system. The body contour C_b and the far field boundary C_f
become constant η contours (Figure 1). The far field boundary is usually
used to approximate infinity in incompressible flow problems. Constant η
contours in the physical plane are required to transform to equi-spaced η
coordinate lines with unit step size in the transformed plane. The spacing
of η contours in the physical plane is controlled by the set of elliptic
equations. The ξ contour spacing on the body surface and outer boundary
in the physical plane is determined by the chosen point distribution on
each surface. The constant ξ contours are also required to transform to
equi-spaced ξ coordinate lines with unit step size in the transformed
plane. The ξ lines are denoted by the subscript i with range $1 \leq i \leq IMAX$
where IMAX is the number of ξ lines. Similarly, the η lines are identified
by a subscript j with range of $1 \leq j \leq JMAX$ where JMAX is the number of η
lines. The values $j = 1$ and $j = JMAX$ are the body and outer boundary
surfaces, respectively. The constant ξ lines $i = 1$ and $i = IMAX$ denote
the branch cut in the physical plane and are therefore identical.

The governing elliptic transformation equations (Equations 9a and 9b) are written with finite differences in quasi-linearized form for the location (i, j). Second order accurate central differences given in Appendix B are used for evaluating each term. The highest order derivative contains the unknown at location (i, j) while the transformation coefficients, which contain lower order derivatives, are evaluated with previous values of the variables x and y. The difference expressions are given below where the indices i and j are understood when omitted.

$$x_{ij} = \{\alpha(x_{i+1} + x_{i-1}) - \frac{\beta}{2}(x_{i+1\ j+1} - x_{i+1\ j-1} + x_{i-1\ j-1} - x_{i-1\ j+1})$$

$$+ \gamma(x_{j+1} + x_{j-1}) + \frac{J^2}{2}[(x_{i+1} - x_{i-1})P + (x_{j+1} - x_{j-1})Q]\}/2(\alpha + \gamma) \tag{85}$$

$$y_{ij} = \{\alpha(y_{i+1} + y_{i-1}) - \frac{\beta}{2}(y_{i+1\ j+1} - y_{i+1\ j-1} + y_{i-1\ j-1} - y_{i-1\ j+1})$$

$$+ \gamma(y_{j+1} + y_{j-1}) + \frac{J^2}{2}[(y_{i+1} - y_{i-1})P + (y_{j+1} - y_{j-1})Q]\}/2(\alpha + \gamma) \tag{86}$$

The i index near the branch cut is adjusted as follows:

when i = 1	then i - 1 = IMAX - 1
when i = IMAX - 1	then i + 1 = 1
when i = IMAX	then i = 1

The set of finite difference equations has the range of indices given by $1 \leq i \leq IMAX - 1$ and $2 \leq j \leq JMAX - 1$ which results in (IMAX-1)(JMAX-2) equations for the unknown values of x and y at the interior grid points.

The system of difference equations is solved using successive over relaxation (SOR) iteration. For a general function f, an approximate solution for f using SOR iteration has the form

$$f^{(s+1)} = \omega f^* + (1 - \omega)f^{(s)} \tag{87}$$

where s represents the iterate number, ω is an acceleration parameter, and * represents the current value of f calculated from the difference equation. The acceleration parameter is always one for the first iteration. The system of linearized difference equations given by Equations 85 and 86 obtained from the elliptic generating differential equations is consistently ordered (Reference 81). Thus, local optimum acceleration parameters ω_{ij} can be calculated from matrix theory (Reference 81) and are given by Hodge (Reference 53). Convergence of the iteration procedure is determined by comparing the absolute value of the difference in successive iterates with a prescribed error criteria E.

The SOR iteration technique requires an initial guess for the solution. Geometric contours with a shape similar to the outer computational boundary are used for constant η lines and straight lines which emanate from the body center are used for ξ lines. A similar approach has been successfully used by Thames (Reference 44) and Hodge (Reference 53).

The forcing function $Q(\xi, \eta)$ defined by Equation 15 is evaluated throughout the (ξ, η) plane following the procedure described in Section II.2. The similarity parameter values σ (which give equal increments of tangential velocity for a specified number of boundary-layer points) are calculated from Equation 18 using Newton-Raphson iteration. The equivalent y values at a given $x(\xi$ line) are found from the similarity relation (Equation 19). The η derivatives given by Equations 22 and 23

are then approximated using the above values for y and the specified η differences as follows:

$$\left(\frac{d\eta}{dy}\right)^2 \doteq (y_2 - y_1)^{-2} \qquad \text{at } \eta = 0$$

(88)

$$\left(\frac{d\eta}{dy}\right)^2 \doteq (\Delta y_\infty)^{-2} \qquad \text{at } \eta = \eta_{max} - 1/2$$

where $\Delta\eta = 1$, y_i are the boundary-layer y values, and Δy_∞ is the specified far field y difference between the last two points on the given ξ line. Then the damping factor D is found using Equation 24. Next, the analytical expression for $d\eta/dy$ in Equation 21 is evaluated on the far field interval Δy_∞ and on each boundary-layer Δy interval determined by the y_i values.

This system of equations for $A_k(\xi)$ is solved using Gauss elimination. Thus, for a given ξ line, values for A_k and D are calculated for use in evaluating the $Q(\xi, \eta)$ forcing function. This function is then used during the SOR iteration for the transformation values of x and y.

Additional ξ contours can be added in the wake region by using the interpolating technique given in Appendix C.

2. NAVIER-STOKES FINITE DIFFERENCE EQUATIONS

Approximate solutions of the unsteady (Reynolds averaged, incompressible, turbulent, and Navier-Stokes) equations are obtained by using an implicit finite difference procedure. Explicit numerical methods can be used to obtain approximate solutions by advancing the time by small increments. The allowable time increments are constrained by numerical stability criteria. Implicit finite difference methods can also provide *approximate solutions by marching in time with small time steps*. Implicit methods usually do not have numerical stability constraints imposed on the time step. However, at each time step a large system of simultaneous difference equations must be solved. A matrix iterative technique such as SOR iteration is an attractive solution method because of the large matrix size. Convergence criteria are thus introduced in place of stability criteria.

44

The implicit method consists of both a linearization of the equations and the application of finite differences to those equations. The x component, transformed, momentum equation given by Equation 48 is considered first. Rearranging the convective terms, the equation becomes

$$u_T + u_\xi(u\frac{y_\eta}{J} - v\frac{x_\eta}{J}) + u_\eta(v\frac{x_\xi}{J} - u\frac{y_\xi}{J}) + uD = -p_\xi\frac{y_\eta}{J} + p_\eta\frac{y_\xi}{J}$$

$$+ \frac{1}{Re_t} \{\frac{\alpha u_{\xi\xi} - 2\beta u_{\xi\eta} + \gamma u_{\eta\eta}}{J^2} + u_\xi (\frac{\tau}{J^2}) + u_\eta (\frac{\sigma}{J^2})\} \qquad (89)$$

Equation 89 is now written in quasi-linear form where lower order derivatives of the variables occur in "coefficients". The current value for the unknown variable at location (i, j) occurs in the highest order derivative of each term while the "coefficients" are evaluated with the last available values for the variables u, v, and p. In this form, the coefficient of u_ξ in the convective terms, $\frac{1}{2}(uy_\eta - vx_\eta)/J$, is proportional to the component of velocity in the ξ direction. Similarly, the coefficient of u_η in the convective terms, $\frac{1}{2}(vx_\xi - uy_\xi)/J$, is proportional to the component of velocity in the η direction. These quantities are designated UC and VC, respectively.

Finite difference expressions given in Appendix B are used to approximate the terms in Equation 89. First order accurate backward differences are used for the time derivative. The first derivatives of pressure are approximated with second order accurate central differences. Likewise, second order central difference expressions are used for the second derivatives of velocity in the viscous terms. Second order accurate upwind differencing is used for the velocity first derivatives in the convective terms. The quantities UC and VC determine the sign of the local velocity in the ξ and η directions. If UC $\geq$ 0, then backward upwind differencing is used for the ξ derivatives while UC < 0 dictates forward upwind differencing. Also, backward upwind differencing for η derivatives occurs if VC $\geq$ 0 while forward upwind differencing is used

if VC < 0. Second order accurate upwind differences are also used for the
velocity first derivatives in the viscous terms. The direction is determined
by the sign of the coefficients. Points on the J = 2 and J = JMAX - 1
contours use first order upwind differences for η first derivatives if
the velocity direction indicates flow from the body surface (J=1) or the
outer boundary (J = JMAX). Near the body surface the grid spacing is
extremely small, and velocity gradients are small near the outer boundary.
Thus, in both cases the associated artificial viscosity has a negligible
effect. The transformation derivatives in Equation 89 are evaluated with
second order central differences. The velocity derivatives in the velocity
divergence term are also evaluated using central differences.

Difference equations are written with the following convenient
conventions. Terms which contain unknowns at location (i,j) are fully
subscripted. The finite difference expression for location (i, j) as
described previously is understood when only the term is given. The
subscripts (i, j) and superscript n are assumed when omitted. The
resulting difference equation for Equation 89 becomes

$$\frac{u_{ij} - u_{ij}^{n-1}}{\Delta t} + (3u_i - 4u_{IC1} + u_{IC2})|UC| + (3u_j - 4u_{JC1} + u_{JC2})|VC| + uD$$

$$= -\frac{y_\eta}{2J}(p_{i+1} - p_{i-1}) + \frac{y_\xi}{2J}(p_{j+1} - p_{j-1})$$

$$+ \frac{1}{Re_t}\{\frac{\alpha}{J^2}(u_{i+1} - 2u_{ij} + u_{i-1}) + \frac{\gamma}{J^2}(u_{j+1} - 2u_{ij} + u_{j-1})$$

$$- \frac{\beta}{2J^2}(u_{i+1\ j+1} - u_{i-1\ j+1} + u_{i-1\ j-1} - u_{i+1\ j-1})$$

$$- (3u_i - 4u_{IV1} + u_{IV2})|UV| - (3u_j - 4u_{JV1} + u_{JV2})|VV|\} \qquad (90)$$

where

	for UC $\geq$ 0	for UC < 0
	IC1 = i - 1	IC1 = i + 1
	IC2 = i - 2	IC2 = i + 2
	for VC $\geq$ 0	for VC < 0
	JC1 = j - 1	JC1 = j + 1
	JC2 = j - 2	JC2 = j + 2

and UV $\equiv -\tau/2J^2$ and VV $\equiv -\sigma/2J^2$

where

	for UV $\geq$ 0	for UV < 0
	IV1 = i - 1	IV1 = i + 1
	IV2 = i - 2	IV2 = i + 2
	for VV $\geq$ 0	for VV < 0
	JV1 = j - 1	JV1 = j + 1
	JV2 = j - 2	JV2 = j + 2

The difference equation for conservation of mass (Equation 51) for location (i, j) is given by

$$D = \frac{y_\eta}{2J} (u_{i+1} - u_{i-1}) - \frac{x_\eta}{2J} (v_{i+1} - v_{i-1}) - \frac{y_\xi}{2J} (u_{j+1} - u_{j-1})$$

$$+ \frac{x_\xi}{2J} (v_{j+1} - v_{j-1}) \tag{91}$$

The following finite difference definitions are introduced for the transformation derivatives and coefficients at location (i, j):

$$\text{XETA} = x_\eta/2J \qquad \text{XXI} = x_\xi/2J$$

$$\text{YETA} = y_\eta/2J \qquad \text{YXI} = y_\xi/2J$$

$$\text{ALFA} = \alpha/J^2 \quad \text{GAMA} = \gamma/J^2 \quad \text{BETA} = -\beta/2J^2$$

With these definitions, Equation 90 can be written to provide an expression for u_{ij}^n given by

$$u_{ij}^* = \{u_{ij}^{n-1} + \Delta t[-YETA(p_{i+1} - p_{i-1}) + YXI(p_{j+1} - p_{j-1})$$

$$+ |UC|(4u_{IC1} - u_{IC2}) + |VC|(4u_{JC1} - u_{JC2}) - uD$$

$$+ \frac{1}{Re_t} [ALFA(u_{i+1} + u_{i-1}) + GAMA(u_{j+1} + u_{j-1})$$

$$+ BETA(u_{i+1\ j+1} - u_{i+1\ j-1} + u_{i-1\ j-1} - u_{i-1\ j+1}) + |UV|\ (4u_{IV1} - u_{IV2})$$

$$+ |VV|\ (4u_{JV1} - u_{JV2})]]\}/\{1 + \Delta t[3(|UC| + |VC| + |UV| + |VV|)$$

$$+ \frac{2}{Re_t} (ALFA + GAMA)]\} \qquad (92)$$

where * denotes the value of the unknown calculated directly from the difference equation.

Several observations are made concerning the difference equation for u_{ij} given by Equation 92. The unknowns v_{ij} and p_{ij} do not appear explicitly. In fact p_{ij} does not appear at all. The y component of velocity v_{ij} does appear implicitly in the quasi-linear coefficients UC and VC as does u_{ij}. The previous value for u_{ij} occurs explicitly in the term containing the velocity divergence D. The finite difference linearization assumption requires that the latest prior values for u_{ij} and v_{ij} are used in these instances.

In an analogous manner, the y component, transformed momentum equation, (Equation 49) is written for v_{ij}^n and becomes

$$v_{ij}^* = \{v_{ij}^{n-1} + \Delta t[XETA(p_{i+1} - p_{i-1}) - XXI(p_{j+1} - p_{j-1})$$

$$+ |UC| (4v_{IC1} - v_{IC2}) + |VC| (4v_{JC1} - v_{JC2}) - vD$$

$$+ \frac{1}{Re_t} [ALFA(v_{i+1} + v_{i-1}) + GAMA(v_{j+1} + v_{j-1})$$

$$+ BETA(v_{i+1 \ j+1} - v_{i+1 \ j-1} + v_{i-1 \ j-1} - v_{i-1 \ j+1}) + |UV| (4v_{IV1} - v_{IV2})$$

$$+ |VV| (4v_{JV1} - v_{JV2})]]\}/\{1 + \Delta t[3(|UC| + |VC| + |UV| + |VV|)$$

$$+ \frac{2}{Re_t} (ALFA + GAMA]\}\tag{93}$$

Again, p_{ij} does not appear either explicitly or implicitly. The unknown u_{ij} appears implicitly in the coefficients UC and VC. Also, v_{ij} occurs implicitly in UC and VC and explicitly in the velocity divergence term. The most current previous values for u_{ij} and v_{ij} are used in these lower order coefficients.

The static pressure throughout the flow field is calculated from the Poisson pressure equation (Equation 50) derived in Section II. Second order accurate central differences are used to approximate the second derivatives of pressure in the transformed Laplacian term. The first derivatives of pressure in the Laplacian are approximated by second order accurate upwind differences. The direction is based on the sign of the coefficients σ and τ which is the same method used for the momentum equations. In this equation, a nonlinear source term occurs which is composed of transformation and velocity derivatives. The transformation derivatives are approximated with second order accurate central differences. Second

order accurate upwind differences are used for the velocity derivatives. The direction of the differences at each location is determined by the direction of the local ξ and η velocity components related to UC and VC previously defined. The time derivative of the velocity divergence is approximated with a first order accurate backward difference. The requirement that the velocity divergence at the nth time step be zero is incorporated into the difference equation by setting D^n to zero. The numerical non-zero quantity D^{n-1} is retained as a correction factor. In this way, the static pressure is found which tends to satisfy mass conservation at every location for each time step.

The following definitions are given for the finite difference representation of the source terms as described above:

$$UX = (y_\eta u_\xi - y_\xi u_\eta)/J$$

$$UY = (x_\xi u_\eta - x_\eta u_\xi)/J$$

$$VX = (y_\eta v_\xi - y_\xi v_\eta)/J$$

$$VY = (x_\xi v_\eta - x_\eta v_\xi)/J$$

If these definitions, the previous transformation coefficient definitions, and index conventions are used, the transformed pressure equation (Equation 50) is rearranged for the field static pressure p_{ij}^n given by

$$p_{ij}^* = \{- \frac{D^{n-1}}{\Delta t} + (UX)^2 + 2(VX)(UY) + (VY)^2 + ALFA\,(p_{i+1} + p_{i-1})$$

$$+ GAMA(p_{j+1} + p_{j-1}) + BETA(p_{i+1\;j+1} - p_{i+1\;j-1} + p_{i-1\;j-1}$$

$$- p_{i-1\;j+1}) + |UV|\,(4p_{IV1} - p_{IV2}) + |VV|\,(4p_{JV1} - p_{JV2})\}/\{3(|UV|$$

$$+ |VV|) + 2\,(ALFA + GAMA)\} \tag{94}$$

In this equation p_{ij} does not appear implicitly. The velocity components u_{ij} and v_{ij} are only present implicitly in the nonlinear source terms.

The three difference equations (Equations 92 through 94) form a set of equations for the flow variables u, v, and p at location (i, j) in terms of the transformation derivatives and values of the variables at neighboring points. The quasi-linearization and differencing methods have decoupled the equations with respect to the higher order terms for the unknowns at location (i, j).

The large system of finite difference equations which must be solved for the nth time step is solved using SOR iteration given by

$$u_{ij}^{(s+1)} = \omega_{uv}\, u_{ij}^{*} + (1 - \omega_{uv})\, u_{ij}^{(s)} \qquad (95a)$$

$$v_{ij}^{(s+1)} = \omega_{uv}\, v_{ij}^{*} + (1 - \omega_{uv})\, v_{ij}^{(s)} \qquad (95b)$$

$$p_{ij}^{(s+1)} = \omega_{p}\, p_{ij}^{*} + (1 - \omega_{p})\, p_{ij}^{(s)} \qquad (95c)$$

where s is the iterate number, * designates the current value obtained from the difference equation, and ω_{uv} and ω_{p} are acceleration parameters. The acceleration parameters are always unity for the first iteration.

The computation of the wall static pressure is carried out separately as discussed in Section II. The pressure iteration technique of Chorin (Reference 68), given by Equation 40, avoids the difficulty of formulating one sided differences at the body for the Laplacian of pressure. Also, at the body surface, conservation of mass is directly imposed. Second order accurate upwind differences are used for the transformation and velocity first derivatives in the velocity divergence of Equation 51. The acceleration parameter Φ, which is related to SOR iteration of the Poisson pressure equation, is given by Hodge (Reference 53) as

$$\Phi = 2\omega_{pb}/\{\Delta t(ALFA + GAMA)\} \qquad (96)$$

where ω_{pb} is an acceleration parameter for the corresponding SOR iteration of the Poisson pressure equation. For consistency, the iteration equation

is repeated as

$$p_b^{(s+1)} = p_b^{(s)} - \phi D \tag{97}$$

where s represents the iterate number and the index notation is kept as described above.

The trailing edge pressure on an airfoil can be difficult to obtain using the iteration procedure if a sufficiently fine grid is not present. Hodge (Reference 53) experienced such difficulties in his laminar flow work. The trailing edge pressure can then be calculated using an average of values obtained by linearly extrapolating the pressures calculated at the closest points on the upper and lower surfaces. For a two point linear extra-polation in the x direction, the pressure at the trailing edge becomes

$$p_1 = \frac{(x_1 - x_3) p_2 - (x_1 - x_2) p_3}{2(x_2 - x_3)}$$

$$+ \frac{(x_1 - x_{IMAX-2}) p_{IMAX-1} - (x_1 - x_{IMAX-1}) p_{IMAX-2}}{2(x_{IMAX-1} - x_{IMAX-2})} \tag{97a}$$

where the x's are the x values at the selected surface points and the surface j = 1 value is understood.

The iteration procedure follows a prescribed order at each point location (i, j). Only the body surface pressure is computed on body points. At field points, the u velocity component is computed first, then the v velocity component, and finally the field pressure p. The points are ordered by varying the $n(j)$ index from j = 1 thru j = JMAX-1 on successive ξ lines in the transformed plane. The ξ lines i = 1 thru i = IMAX-1 are traversed. Values for the variables at i = 1 are set equal to the values at i = IMAX to ensure continuity across the transformation branch cut. The i index is adjusted across the branch cut in a manner identical with that described for obtaining the transformation from Equations 85 and 86.

3. BOUNDARY AND INITIAL CONDITIONS

Boundary and initial conditions are formulated for use in the computa-
tional plane to completely define the numerical problem. Boundary condi-
tions on the body surface are conveniently specified with the body-fitted
coordinate system. The first η contour is constructed to be the body
surface. The analytical no slip boundary conditions for velocity given
by Equation 52 can be directly applied to the body surface in the
computational plane and are given by

$$u_b = 0 \qquad v_b = 0 \tag{98}$$

where the subscript b denotes the body surface η contour. The surface
pressure is calculated as discussed in Section IV.2.

The ξ lines i = 1 and i = IMAX in the computational plane define the
branch cut in the physical plane. No boundary conditions are required or
allowed on these contours. The matching of solutions on these lines, which
was described previously, provides a continuous solution across the cut.

The outer boundary in the physical plane frequently represents con-
ditions at infinity (freestream conditions) given by Equations 53 and 54.
In the body-fitted coordinate system, the outer boundary becomes the largest
η line in the computational plane. The physical outer boundary is chosen
to be a circle with a radius of 10 airfoil chords. The distribution of
points on the outer boundary is readily specified on a circle; also, the
initial input solution for obtaining the transformation as discussed in
Section IV.1 is simple to specify. Ghia and Hodge (Reference 82) applied
a numerical inviscid analysis to a Joukowski airfoil at angle of attack
using freestream boundary conditions for different outer boundaries.
They found that for a 10° angle of attack the lift coefficient differed
by less than one percent and the maximum suction pressure coefficient by
about two percent from the analytical result. Navier-Stokes solutions
using a circular outer boundary with a smaller radius are compared with
the 10 chord radius result to determine effects of boundary placement.

With the outer boundary elected to approximate the far field free-stream, the boundary conditions for velocity and pressure are specified. As pointed out by Roache (Reference 83), caution must be exercised in applying the analytical conditions (Equations 53 and 54) which are strictly valid only in the limit of large distances from the body. If these conditions are used on a boundary at a finite distance away, the result may predict no drag since a wake cannot exist at the outer boundary. This problem is avoided by applying upstream and downstream boundary conditions on the outer boundary. The upstream boundary along which conditions are fixed is defined by the semicircle in the half plane $x \leq 0$ where the x axis lies along the airfoil chord with the origin at the midchord. The downstream boundary for which some variables are permitted to be free is the semicircle in the half plane $x > 0$.

The upstream boundary conditions for the incoming undisturbed flow become

$$u_{i \ JMAX} = \cos \alpha \qquad v_{i \ JMAX} = \sin \alpha \qquad p_{i \ JMAX} = 0 \qquad (99)$$

where i ranges over all ξ contours which terminate on the upstream boundary.

The downstream boundary conditions must allow a wake downstream of a body to pass through the boundary. The no change boundary condition has been widely used (References 53,83) and meets this requirement. One approach requires no change of the velocity components in the freestream direction. Using the expressions for the directional derivative and gradient in the transformed plane, this boundary condition can be written for the u component of velocity as

$$u_\eta = u_\xi \ (x_\eta \ \sin\alpha - y_\eta \ \cos\alpha)/ \ (x_\xi \ \sin\alpha - y_\xi \ \cos\alpha) \qquad (100a)$$

where α is the geometric angle of attack. Now consider a similar downstream boundary condition where the no change condition is imposed on the velocity components along the downstream ξ contours. In a similar manner, this condition in the transformed plane becomes

$$u_\eta = 0 \qquad \qquad v_\eta = 0 \qquad (100b)$$

This boundary condition is identical with the freestream direction boundary condition of Equation 100a when the ξ contours are in the freestream direction. In this case, $\tan\alpha = y_\eta / x_\eta$ and Equation 100a becomes identical with Equation 100b. This case does occur in the downstream wake region for the transformation obtained in Section IV.1. Small changes in the velocity components are found in the far wake region of bodies. The downstream far field inviscid flow field also has negligible changes as seen in the analysis of Appendix F. Thus, the no change conditions of Equation 100b approximate the small far field downstream variations in velocity while allowing the momentum defect in a wake to exit at the outer boundary.

The downstream outer boundary condition for pressure must be considered along with the velocity conditions. Hodge (Reference 53) investigated the use of a similar no change condition for pressure, namely, $p_\eta = 0$ coupled with the velocity conditions of Equation 100b. His laminar solution developed pressure oscillations. The more restrictive condition of specifying the freestream pressure in the far wake was successfully used by Hodge (Reference 53). The specification of pressure recovery with a freely developing velocity defect in the far wake gives a set of numerical boundary conditions which can physcially represent the far wake at a finite far field downstream boundary. The downstream pressure boundary condition becomes

$$p_{i \text{ JMAX}} = 0 \tag{101}$$

The suitable description of the physics at the downstream computational boundary must be written in finite difference form. The no change condition approximated with a second order accurate central difference applied at the midpoint in the computational plane between the boundary point and first interior point on a downstream ξ contour (i index) gives

$$u_{\text{JMAX}} = u_{\text{JMAX-1}} \qquad v_{\text{JMAX}} = v_{\text{JMAX-1}} \tag{102}$$

for the downstream boundary conditions of the velocity components. An alternate formulation is obtained by approximating the no change condition

with a second order accurate upwind difference applied at the boundary point. Then, the downstream boundary conditions for the velocity components become

$$u_{JMAX} = (4u_{JMAX-1} - u_{JMAX-2})/3$$

$$v_{JMAX} = (4v_{JMAX-1} - v_{JMAX-2})/3 \tag{103}$$

These boundary conditions also follow from a second degree polynominal fit with a zero derivative imposed at the downstream boundary.

The time dependent finite difference method given previously requires a set of initial values for the velocities and pressures at all the (i, j) locations. This requirement parallels the result discussed for the differential equations in Section III.2. Two methods are used to provide initial conditions. In the first method, an inviscid solution with circulation for the flow field at the given angle of attack is obtained using SOR iteration as described in Appendix G. This solution then provides initial values for the Navier-Stokes solution. The second technique uses the Navier-Stokes solution for one angle of attack and rotates the velocities by the change in angle of attack. The set of initial values for velocity and pressure is then used to start a Navier-Stokes solution at the new angle of attack.

4. TURBULENCE MODEL

The numerical procedure which implements the eddy viscosity turbulence model described in Section III is discussed. The two-layer model near the airfoil surface is presented followed by the far wake model. The procedure used in the near wake is then described. The eddy viscosity distribution throughout the flow field is calculated at the beginning of each time step. SOR iteration is then used to determine the velocities and pressures at the new time level. The eddy viscosity distribution is not changed during the iteration process.

The inner viscosity computation from Equation 60 requires values of the tangential and normal velocity derivatives and the distance from the surface. These velocity derivatives are given by Equations 70 and 71 in the transformed plane. They are evaluated using second order accurate central differences for both the transformation derivatives and the u and v velocity component derivatives with respect to ξ and η. The inner eddy viscosity is identically zero at the surface ($\eta=1$) and need not be calculated separately. The corresponding velocity expression which is found in the exponent of the damping factor (Equation 62) must be evaluated at the airfoil surface for each ξ contour in regions of turbulence. The derivatives with respect to η are approximated by second order accurate forward differences found in Appendix B, and the derivatives with respect to ξ are evaluated using second order accurate central differences. The distance from the surface to the point (i, j) is measured along the constant ξ line represented by index i. The freestream chord Reynolds number appears throughout the model as a result of writing the equations in nondimensional form and is an input parameter.

The adverse pressure gradient turbulence model modification in the trailing edge region given by Equation 65 is implemented next. The origin of the distance s, measured along the airfoil surface from the trailing edge separation point, is determined by examining the u velocity component at points on the η contour next to the surface (j=2). The search begins on the ξ line corresponding to the 95 percent chord location and advances toward the airfoil leading edge along the second η line. The search terminates when a positive value for u_{i2} is detected which indicates attached flow. The relaxation factor τ is then evaluated for each applicable ξ line where trailing edge separation is detected. The inner eddy viscosity is multiplied by the relaxation factor which adjusts the adverse pressure gradient inner eddy viscosity constant k_1.

After the inner eddy viscosity is computed, the limiting technique
evaluates the computed value. The inner eddy viscosity is prevented from
decreasing in the outward normal and downstream tangential flow directions
by comparing the value with previously computed values as given by the
following sequence:

$$\epsilon_{ij} \geq \epsilon_{i\ j-1} \qquad \text{and} \qquad \epsilon_{ij} \geq \epsilon_{i-1\ j}.$$

The larger value is selected during each comparison. The initial inner
eddy viscosity limiting distribution is calculated in the attached boundary-
layer region with a favorable pressure gradient near the airfoil leading
edge. The first or outward direction limiting condition is imposed here
as well.

The limit value of the inner eddy viscosity is then compared with the
calculated outer layer eddy viscosity. Whenever the inner eddy viscosity
first exceeds the outer value, the outer eddy viscosity is then used for the
remaining locations outward from the surface. This switch ensures the
continuity of the eddy viscosity distribution.

The computation of the outer eddy viscosity given by Equation 61
requires values for the local boundary-layer edge velocity and the
displacement thickness defined by Equation 64. These quantities are
calculated for each ξ contour which crosses the turbulent boundary-layer.
For a ξ line, the local edge velocity u_e is defined to be the maximum
tangential velocity measured relative to the local surface tangent line.
The tangential velocity is given by Equation 68 and is evaluated as
described previously for the inner eddy viscosity. The boundary-layer
thickness δ is then the distance along the ξ line from the surface to
the first point where the tangential velocity is not less than $0.99\ u_e$.
The displacement thickness is calculated using trapezoidal integration
where the limits of integration are determined by the computed boundary-
layer thickness.

The resulting eddy viscosity distribution is modified next to simulate the transition from laminar to fully turbulent flow. The transition factor Γ, given by Equation 67, is calculated as follows. The starting location for transition on the airfoil surface must be specified. This location is specified by designating the first grid point on the surface downstream as well as the distance to that first grid point Δs. The transition distance s from the starting location to a given ξ line is calculated by adding Δs to the distance between the successive surface grid points with known locations. The relaxation factor Λ is determined from the transition factor Equation 67 and the definition of Λ. If $\Gamma = 3/4$ is specified when the transition distance equals three fourths of the total transition length, then $1/\Lambda$ is given by

$$1/\Lambda = 2.4456/x_L \tag{104}$$

where x_L is the total assumed transition length. The eddy viscosity distribution computed previously on a ξ line is multiplied by the corresponding constant Γ to obtain the revised distribution of turbulent eddy viscosity which includes the transition region.

The final modification made to the eddy viscosity distribution across the upper surface turbulent region involves the decrease of turbulence in the direction from the boundary-layer toward the far field. The intermittency factor given by Equation 63 models this behavior. The previously calculated boundary-layer thickness δ and the distance from the airfoil surface to the (i, j) location on a ξ line are used to compute the intermittency γ for that location. The previous values of the outer eddy viscosity are multiplied by the corresponding value of the intermittency factor to obtain the final eddy viscosity distribution for the turbulent region above the airfoil surface at the nth time step.

The procedure for computing the eddy viscosity distribution on a ξ line across the turbulent flow zone above the airfoil is repeated downstream for each ξ line through the 95 percent chord point. The ξ contours near the trailing edge deviate from the local normal direction in excess of 10°. For locations in this small region, the eddy viscosity is found by using the last calculated value upstream in a direction tangent to the airfoil surface.

The calculation of the far wake eddy viscosity given by Equation 73 is similar to the computation of the outer layer eddy viscosity. In the wake region the η contours are approximately orthogonal to the flow direction in the wake. The η contours are thus conveniently defined paths across the wake for use in computing wake characteristics.

On an η contour, the component of velocity in the freestream direction is computed for the grid points spanning the wake. The minimum of these directional velocity components in the wake is determined. The maximum values of the velocity components which occur on either side of the minimum value are found and designated the upper and lower edge velocities. Then the upper and lower edges of the wake are defined as the points where the local velocity component in the freestream direction first reaches 99 percent of the upper and lower edge velocities, respectively. The distances from the point of minimum velocity to the upper and lower wake edges are defined as the upper and lower wake thicknesses, respectively. These distances determine the limits of integration when calculating the upper and lower wake displacement thicknesses from Equation 64. The origin of the variable of integration is at the grid point where the minimum velocity occurs. The upper and lower wake displacement thicknesses are numerically evaluated with trapezoidal integration. The half wake displacement thickness δ_w^* is the average of the upper and lower displacement thicknesses. The far wake eddy viscosity is calculated from Equation 73 using the thickness δ_w^* and an average of the upper and lower edge velocities.

The intermittency factor for each grid point on an η contour is determined using the average value of the upper and lower wake thicknesses for δ in Equation 63. The local distance to each point is calculated from the location of minimum velocity along the η contour.

The near wake model is numerically implemented by considering the upper turbulent and lower laminar boundary-layers separately. The eddy viscosity distribution, which is calculated near the trailing edge of the airfoil at the 95 percent chord location, is extended into the near wake along a direction parallel to the airfoil surface defined by the 95 percent chord and 99 percent chord grid point locations. The chord line is the line of extension for the boundary-layers in the near wake. The ξ lines $i = 1$ and $i = \text{IMAX-1}$ define the interaction zone in the near wake. The noninteracting distance WL_1 in Equation 74 is based on the length of the lower laminar boundary-layer thickness computed at the 95 percent chord location. This boundary-layer thickenss is computed by the same method used previously for the upper surface boundary-layer. The distance WL_2 along the chord line from the trailing edge to the location where the far wake eddy viscosity model begins is also calculated as a multiple of the laminar trailing edge boundary-layer thickness. The eddy viscosity in the interaction zone is computed with the two calculated distances and the far wake eddy viscosity using Equation 74.

5. FORCE COEFFICIENTS

The forces and moments exerted on the airfoil body by the flow field are evaluated at the body surface using Equations 79, 80, and 82. The integrals are evaluated using trapezoidal integration. The product terms in the integrands of the form (fg) are integrated by using products of averages, $(f_i + f_{i+1})(g_i + g_{i+1})/4$. The ξ derivatives are evaluated using second order accurate central differences, and the η derivatives are formulated with second order accurate upwind forward differences. The lift and drag coefficients are calculated by adding the components of x and y direction force coefficients in the normal freestream (90 degrees counterclockwise) and freestream directions, respectively, using Equations D-13 and D-14.

The alternate technique based on the control volume analysis in
Appendix D for computing the forces on the airfoil body is numerically
implemented in a similar manner. The force coefficients in the x and y
directions for a two-dimensional control volume defined by an η line are
given by Equations 83 and 84, respectively. The line integrals are again
computed with trapezoidal integration using products of averages. The ξ
derivatives are evaluated with second order accurate central differences.
The η derivatives are evaluated with second order accurate central dif-
ferences on the interior η lines. Second order accurate upwind differences
are used to approximate the η derivatives on the body and outer boundary
η lines. The area integral is also evaluated using trapezoidal integration.
The Jacobian for an area element bounded by the i and i+1 ξ lines and j-1
and j η lines is calculated by taking the average of the Jacobian values
previously computed for the viscous term in the line integrals at the cor-
responding ξ segments on the j-1 and j η lines. The area integrals are
computed for both n and n-1 time intervals using the previously computed
flow field values. The time derivative is then evaluated using a first
order accurate backward difference.

SECTION V

DISCUSSION OF RESULTS

Numerical solutions for two-dimensional incompressible turbulent viscous flow over a NACA 0012 airfoil section are obtained using the implicit finite difference method previously described. The NACA 0012 airfoil section is chosen because of its widespread use as a test case in both experimental and computational work (References 65,66). The solutions are for angles of attack of 5°, 7.5°, 9.5°, and 11.5° at a chord Reynolds number of 170,000. This Reynolds number is selected for comparison with both previous NACA data (Reference 56) and Air Force F. J. Seiler Research Laboratory data (Reference 84).

The numerically generated body-fitted coordinate system which was used for each solution is presented. The successive-over-relaxation (SOR) iteration numerical parameters and convergence criteria along with the steady state convergence criteria are then discussed. The velocity and pressure fields and streamline contours obtained from the numerical solutions are examined. The calculated laminar separation bubble characteristics are compared with empirical results. The position of transition to turbulence and the transition length relative to the separation bubble location are discussed. The computed airfoil surface mean pressure distributions are compared with both an inviscid solution and experimental data. The numerically predicted lift and drag forces exerted by the flow field on the airfoil are presented along with available experimental measurements. The effects that the placement and type of imposed far field boundary conditions have on the numerical solution are discussed. The sensitivity of the numerical solution to grid size is examined.

The curvilinear body-fitted grid shown in Figure 3 is numerically generated using boundary-layer parameters for the attraction of η contours towards the airfoil surface and linear interpolation for wake resolution given by Appendix C. The Blasius series flat plate chord Reynolds number of 200,000, a nondimensionalized boundary-layer edge

velocity of 1.2, and seven grid points specified in the boundary-layer
are used in the η contour attraction technique (Reference 7). The
distribution of airfoil surface points is accomplished with Equation 26
where A1 = 0.6, A2 = 0.4, and A3 = 1.0. Seventy-one ξ or surface points
together with 44 η contours are used. The transformation difference equa-
tions (Equations 85 and 86) were then solved using SOR iteration. The
optimum local acceleration parameters varied between 0.8 and 1.5 throughout
the flow field with essentially no change in the local values after 25
iterations. After 350 iterations, the maximum errors in the solution
for both x and y were less than $|10^{-4}|$ and occurred near the outer boundary
above the airfoil. Additional ξ lines were added in the airfoil wake
region using the interpolation method described in Appendix C. Eight
grid points (four at a time) were inserted on the rounded trailing edge.
Table C-1 gives the ξ and η indexing for the final 79x44 grid shown in
Figure 3 and the equivalent indices for the 71x44 original grid.

The airfoil is thus defined by a total of 79 points. Eleven grid
points define the first 5% chord nose region and 17 points are used to
define the rounded trailing edge. The maximum distance between successive
surface grid points is 5% of the chord. The ξ lines intersect the surface
η contour within 10° of the local normal direction except in the last 5%
chord region near the trailing edge.

The SOR iteration parameters and convergence criteria which are
required by the numerical implicit procedure are similar for each angle
of attack solution. The acceleration parameters had values of 1.0 for the
velocity components, 0.9 for the surface pressure, and 1.10 or 1.15 for
field pressures. The larger value of ω_p was used at 9.5° and 11.5° angles
of attack. The convergence criteria for the SOR iteration required that
the maximum change in the relative magnitudes of u, v, and p for all
locations be less than 1%. This criteria was relaxed to 5% for the 9.5°
and 11.5° cases. Three iterations per time step were the maximum
necessary during most of each computed case. For the 9.5° case, the
approach to the steady state solution was re-run with ω_{pb} = 0.95 and ω_p =
1.10 for two characteristic times. An additional iteration per time step

was required to maintain the same error tolerance. Computed values of lift and drag were virtually identical.

Although implicit SOR methods have been shown by linear stability analyses to be unconditionally stable, convergence at a given time required a small time step $\Delta t < 0.001$. The analysis in Appendix E based on linear matrix theory indicates that the diagonal dominance of the set of finite difference equations given by Equations 92 and 93 has a definite dependence on $1/\Delta t$. Diagonal dominance is a necessary and sufficient condition for convergence (Reference 81) of constant coefficient linear systems using SOR iteration. Although this system of equations has lower order nonlinearities and variable coefficients, the order of magnitude study of Appendix E indicates convergence if the most stringent requirement $\Delta t \lesssim 0.0003$ is applied. A constant time step equal to 0.0005 was used for each solution. No convergence problems were encountered.

The finite difference method described in Section IV is a time dependent technique. The solution is advanced in time by Δt increments. The numerical solution was considered to have reached a steady state when changes in the computed values of the lift and drag coefficients were less then 1% over one characteristic or nondimensional time period. Each steady state solution required three to six characteristic time periods and from two to four hours of CPU time on a CDC CYBER 750 computer.

The numerical solution of the mean flow field near the airfoil section at each angle of attack is presented by using streamline contours, velocity field vectors, and pressure contours. The mean streamline contours are shown in Figures 4 through 7. A small laminar separation bubble on the upper surface with negligible trailing edge separation is seen in Figure 4 for $\alpha = 5°$. For an increased angle of attack equal to 7.5°, the separation bubble has decreased in size and moved forward toward the leading edge of the airfoil. Figure 5 also shows the turbulent trailing edge separation region which has also moved forward. The trailing edge separation region has grown significantly and has progressed to the

quarter chord position when the angle of attack has reached 11.5°. This behavior is typically observed during trailing edge stall (Reference 72).

The velocity field vector plots presented in Figures 8 through 11 also illustrate the phenomena discussed previously. In addition, a small scale clockwise rotational motion is observed in the rear portion of the trailing edge separation region. A circulatory flow pattern within the laminar separation bubble is seen for $\alpha = 5°$ in Figure 8. The boundary-layer near the leading edge for each angle of attack contains at least five grid points along each ξ contour while approximately 10 points resolve the lower surface laminar boundary-layer near the trailing edge. This number of points should be sufficient to resolve the primary features. The pressure contours near the airfoil in Figures 12 through 15 clearly show expanding regions of low pressure above the airfoil and high pressure below the airfoil as the angle of attack increases. The large pressure variations in the upper surface suction peaks are also observed. The pressure fields indicate that only small pressure variations occur in the wake for each angle of attack. The smooth and continuous numerical solution for the pressure field is in sharp contrast to the large oscillatory results obtained by Hodge (Reference 7) for laminar flow.

For a moderately thick airfoil with a smooth surface in a flow with a low freestream turbulence intensity, the laminar boundary-layer near the leading edge can separate upon encountering a strong adverse pressure gradient. Subsequently, shear layer instabilities can cause transition to turbulence. The increased mixing may reattach the shear layer and thereby form a separation bubble. The formation of separation bubbles and their relationship with the stalling characteristics of airfoils at various Reynolds numbers have been investigated by Gault (Reference 85), Gaster (Reference 86), Hoad, et al (Reference 87), and Arena and Mueller (Reference 88). The laminar separation bubble has been observed experimentally by Gregory and O'Reilly (Reference 89) for the NACA 0012 airfoil over a large range of Reynolds numbers. These experimental and empirical results will be used to compare with the numerical solutions.

In this investigation, the beginning of turbulent transition on
the upper surface of the airfoil and the transition length have been based
on the closure of the laminar separating shear layer. The surface mean
pressure coefficients for $\alpha = 5°$ and $7.5°$ presented in Figures 16 and
17 clearly show the laminar bubble constant pressure region, downstream
of the suction peak, followed by a rapid recovery. Transition in the
numerical solution occurs near the downstream side of the bubble where
the steep pressure recovery begins. This phenomenon has been reported by
Wallis (Reference 90) and Arena and Mueller (Reference 88). The chord
locations for the start of transition x_t and full turbulence x_T relative
to the separation and reattachment points of the bubble, x_S and x_R
respectively, are given in Table 1. For the smaller angles of attack,
reattachment occurred prior to attaining fully turbulent flow. This
behavior has been experimentally observed by Arena and Mueller (Reference
88) in their low Reynolds number flow study.

The computed values of several parameters at separation for both
$\alpha = 5°$ and $\alpha = 7.5°$ cases agree with empirical results and are presented
in Table 2. The pressure gradient parameter $M = - \Theta^2 \, Re \, du_e/ds$ in
nondimensional variables, where Θ is the momentum thickness and s is
arclength, compares favorably with the laminar separation criteria of
Curle and Skan (Reference 91) given by $M \geq 0.09$. The shape parameter
$H_{12} = \delta*/\Theta$ takes on values of 3.1 and 3.2 at laminar separation compared
with an average value of 3.5 reported by Curle and Skan. The Reynolds
number at separation based on the displacement thickness ($Re_{\delta*S}$) has a
value greater than 500 and predicts a short bubble using the Owen-Klanfer
(Reference 92) criteria confirmed by Gault (Reference 85) and Crabtree
(Reference 93). The bubble length L_B is of the order $10^2 \, \delta*_S$ and decreases
rapidly with increased angle of attack as seen in Table 2. This relation-
ship also indicates a short bubble (References 90,93) whereas long bubbles
have lengths of the order $10^4 \, \delta*_S$ (References 85,86). The assumption
that laminar separation precedes turbulent transition is verified with

TABLE 1

COMPUTED CHARACTERISTICS OF TURBULENCE NEAR THE AIRFOIL LEADING EDGE ($x = -0.5$)

α (Deg)	x_S	x_t	x_R	x_T
5.0	− 0.42	− 0.24	− 0.15	− 0.09
7.5	− 0.47	− 0.42	− 0.38	− 0.35
9.5	−	− 0.48	−	− 0.46
11.5	−	− 0.49	−	− 0.48

TABLE 2

COMPUTED LAMINAR SEPARATION BUBBLE CHARACTERISTICS

α (Deg)	M_S	H_{12S}	$Re_{\delta*S}$	$Re_{\Theta S}$	δ^*_S	L_B	Λ_R
5	.124	3.1	680	220	.0025	.27	−.002
7.5	.091	3.2	540	168	.0013	.09	−.002

the computed Reynolds number at separation based on momentum thickness $Re_{\Theta S}$. Crabtree's (Reference 94) criteria indicates that transition has occurred if $Re_{\Theta S} > 780$ when M_S first reaches 0.09. Thus, the solutions correctly predict that laminar separation occurs before transition to turbulence. The turbulent reattachment criterion for the bubble given by Roberts (Reference 95) is $\Lambda_R = (\Theta / u_e)\, du_e/ds \geq - 0.0059$. This criterion is also satisfied as shown in Table 2.

The trends discussed previously for M_S, Λ_R, and both boundary-layer Reynolds numbers continue at the higher angles of attack. However, at angles of attack near stall the bubble length decreases to about 1% chord (Reference 90) which is the order of the ξ contour spacing near the leading edge. The numerical solutions at $\alpha = 9.5°$ and $\alpha = 11.5°$ consequently do not resolve the bubble, as seen in Figures 18 and 19. The solutions become very sensitive to small changes in the turbulent transition length x_L and starting location x_t. For example, at $\alpha = 9.5°$ with an initial transition location of $x_t = -0.48$, a change in transition length from 0.022 to 0.025 produced shedding of bubbles, large pressure oscillations, and a significant 30% increase in average drag compared with the steady state solution. The experimental pressure data were measured with diaphragm transducers capable of measuring frequencies well beyond 5000 Hz. No dominant frequency was observed. Hoad, et al (Reference 87) recently observed a small scale unsteadiness in a short region near the surface of a NACA 0012 airfoil at angle of attack. The laser velocimeter mean velocity histograms for a certain region near the leading edge exhibited dominant and small secondary mean velocities. Hoad, et al suggest that this behavior may indicate an unsteadiness within the laminar separation bubble. However, the remaining flow field was steady.

The numerical solutions presented for each angle of attack are the result of a parametric study where the upper surface transition length and location were varied to close the bubble and maintain steady flow. In each case, a further increase in the transition length or movement downstream of the start of transition resulted in a nonphysical oscillatory

motion propagated downstream with an accompanied large increase in drag. The good agreement between the calculated and empirical separation bubble characteristics indicates that the origin of turbulence on the upper surface is satisfactorily modelled.

Computed boundary-layer velocity profiles at four stations on the upper surface are compared with two sets of hot wire anemometry data (Reference 84) in Figures 20 through 23. The profiles were measured and computed at the same locations on constant ξ lines located approximately at 18%, 50%, 69%, and 92% chord. The profiles are nondimensionalized by the locally computed boundary-layer thickness which is defined as the normal distance from the surface to where the tangential velocity first attains 99% of the local edge velocity. Significant RMS fluctuations for each angle of attack were detected experimentally at the inner data point locations for stations two through four which indicate the presence of a turbulent boundary-layer. No fluctuations were observed in the lower surface boundary-layer at the 90% chord location. This result provides experimental evidence for the assumption that the lower surface boundary-layer remains laminar in the presence of the favorable pressure gradient at the Reynolds number under investigation. The calculated boundary-layer becomes thicker downstream compared with the experimental profiles. This result could be caused by grid boundary-layer resolution errors propagated downstream or by deficiencies in the turbulence model. The hot wire data have an estimated experimental error of 5%.

The boundary-layers on the upper and lower surfaces merge to form the wake downstream of the airfoil. Wake mean velocity profiles at chord locations of 0.58, 0.79, and 1.54 for each angle of attack are shown in Figures 24 through 27. The trailing edge is located at $x = 0.5$. The profiles are measured along constant η lines with the origin on the extended chordline. The thicker numerical upper surface boundary-layer propagates downstream. The computed large variations of velocity near the lower edge of the wake, which come from the lower surface boundary-layer, are in good agreement with the hot wire anemometry measurements.

The measurements were obtained at grid points using the original 71x44
grid while the numerical solutions were obtained from the 79x44 grid system
described previously. The computed values of the wake displacement and
momentum thicknesses approach approximately constant values within 15%
of each other at a location of one chord downstream of the trailing edge.
They were computed using second order accurate trapezoidal integration
and are given in Table 3.

TABLE 3

COMPUTED FAR WAKE CHARACTERISTICS

α (Deg)	δ_w^*	Θ_w
5.0	0.011	0.010
7.5	0.019	0.017
9.5	0.028	0.026
11.5	0.038	0.033

The Reynolds stress $\overline{u'v'}$, nondimensionalized by U_∞^2, was computed
and contour plots are shown in Figures 28 through 31. The geometric
pattern is qualitatively similar to the experimental data obtained by
Coles and Wadcock (Reference 96) for a NACA 4412 airfoil which are
shown in Figure 32. Some experimental measurements were made during the
hot wire anemometry study (Reference 84) of the velocity profiles.
This data also illustrates the rapid variation of negative and positive
stresses in the upper and lower portions of the near wake, respectively.
Magnitudes of the order 0.01 have been observed (References 84,96) in
the near wake and were also obtained numerically where the contour values
vary from -0.01 to +0.01 in Figures 28 through 31.

The computed surface mean pressure distributions for all four angles
of attack, presented in Figures 16 through 19, favorably compare with
the experimental data (Reference 84) which have an estimated error of

5 to 8%. An inviscid solution with imposed Kutta condition was computed using the approach outlined in Appendix G and is also shown. The computed Navier-Stokes laminar suction peak is well defined and increases rapidly with angle of attack. The lower surface pressure peak both moves downstream and becomes broader as the angle of attack increases. This behavior is also seen in the experimental data. A separation bubble is observed in the experimental data where the curvature rapidly changes. The bubble occurs further downstream when compared with the Navier-Stokes computation. This difference is probably caused by freestream turbulence which can delay separation and the subsequent formation of the bubble. The experimental data were measured in a wind tunnel with a freestream turbulence intensity of approximately 0.5% compared with the unperturbed freestream of the numerical solution. Some disagreement occurs in the trailing edge region where the computed result has a more pronounced flat trailing edge stall characteristic.

The computed inviscid surface pressure distribution consistently predicts both a larger suction peak on the upper surface and a larger pressure peak on the lower surface. The discrepancies increase with angle of attack. The inviscid solutions predict complete recovery at the trailing edge with a stagnation point and C_p = 1.0. The large pressure gradients in the inviscid and viscous solutions near the airfoil nose are resolved which indicates an adequate grid point distribution in the region.

An examination of the experimental and inviscid surface pressure distributions for zero angle of attack given in Figure 33 provides *additional information. The inviscid pressure distributions,* obtained with the SOR finite difference technique in Appendix G, for the upper and lower surfaces are indistinguishable. This physically correct symmetric result came directly from the numerical solution and was not specified as a boundary condition. Furthermore, the numerical inviscid result is virtually identical with an inviscid solution (Reference 67) using the method of Theodorsen (Reference 12). The experimental data for

both surfaces agree well with the inviscid results which indicates the small effect that viscosity has on the pressure distribution for a streamlined symmetric airfoil at zero angle of attack. This agreement also provides evidence that the experimental airfoil section does approximate the NACA 0012 configuration. Viscous effects on the pressure distribution do occur (as was previously mentioned) as the angle of attack is increased even for small α. A comparison between the experimental data for the two surfaces reveals a slight suction peak on the lower surface. The suction peak suggests that the experimental zero angle of attack may actually be slightly negative. A small deviation in angle is plausible since the experimental zero was determined by manually adjusting the airfoil attitude until the pressure distributions on both surfaces appeared identical.

The lift coefficients obtained from the present turbulent Navier-Stokes solution, inviscid results, and two sets of experimental data are compared in Figure 34. The experimental results shown have been corrected for angle of attack. The effective experimental zero angle of attack for a symmetric airfoil section is defined to be the angle where the lift coefficient is zero. For the Seiler Laboratory results (Reference 84), the effective zero was found to be 0.5°. This small correction is in accord with the analysis of the nominal zero angle of attack pressure distribution results already presented. Therefore, the experimental data have been translated 0.5° in the negative α direction in Figure 34. The NACA results (Reference 56) were similarly published in corrected form. Other common two-dimensional wind tunnel corrections including solid blocking, wake blocking, and streamline curvature effects were investigated. Empirical low-speed wind tunnel correction factors (Reference 97) using the Seiler Laboratory 2'x3' tunnel geometry were applied to the experimental data at 11.5° to account for blockage and wall interference. The corrected values for the lift coefficient and angle of attack became 98% of the uncorrected lift coefficient and + 0.1°, respectively. Neither data set given in Figure 34 have been so corrected since the changes are small.

73

The two sets of experimental data contain some contrasts. The
NACA data (Reference 56) maintain an approximately linear behavior over a
greater range of angles of attack when compared with the more recent data
(Reference 84). The NACA lift curve then flattens more rapidly near stall.
These minor differences may be explained by a larger freestream turbulence
level in the NACA results which tends to delay the turbulent trailing
edge separation. Also, the major variation of the lift curve at small
angles of attack occurs for Reynolds numbers less than 10^6 (References
56,89). Freestream turbulence can cause more rapid transition and result
in an apparent freestream Reynolds number greater than the nominal
turbulence-free value.

The computed turbulent Navier-Stokes lift coefficients for the
four angle of attack cases are in excellent agreement with the experi-
mental data as shown in Figure 34. The force components were computed
using trapezoidal integration to sum the total surface stresses obtained
from the flow field solution. The numerical results exhibit a gradual
decrease in slope with increased angle of attack similar to the Seiler
Laboratory data. This behavior is consistent with the data because the
numerical solution has a quiescent incoming freestream with a correspond-
ing smaller apparent Reynolds number. The significant effect that the
viscous separation in the trailing edge region has on the lift coefficient
for angles of attack greater than 8° is observed. The computed values
are within 5% of the experimental results. The lift coefficient was also
computed for each angle of attack using the contour momentum integral
method described in Appendix D. The calculated values differ by less
than 1% for n contour paths within one-half chord of the airfoil surface.
This result demonstrates the near flow field consistency in resolving the
lift force. The time dependent terms in Equations 83 and 84 always con-
tributed less than 0.5% of the total computed lift which indicates again
a converged steady solution.

Two inviscid flow predictions for the lift coefficient are shown in
Figure 34 for comparison. The numerical inviscid finite difference results
were computed with the second order accurate trapezoidal integration

technique used in the viscous calculations. The linear airfoil theory
2π slope is included. The inviscid flow results overestimate lift by
25% at an angle of attack of 5°. This discrepancy increases with angle
of attack because the viscous effects which induce stall are not pre-
sent in an inviscid calculation.

The computed drag coefficients for the four cases are compared with
available experimental data (Reference 56) in Figure 35. The force com-
ponents were computed using trapezoidal integration to sum the total
surface stresses obtained from the flow field solution. The drag compo-
nent is in the direction of the incoming freestream flow. The rapid
increase in the drag coefficient which accompanies the smaller increase
in lift at higher angles of attack near stall is observed. Jacobs and
Sherman (Reference 56) acknowledged that the experimental drag data in
this Reynolds number region have error greater than the estimated ±0.001
for the larger Reynolds number results. The agreement between the present
numerical solution and the experimental data is within 10 drag counts
in the region of the maximum lift to drag ratio.

The presented numerical solutions for two-dimensional incompressible
turbulent viscous flow over airfoils were obtained with several parametric
studies. The effects associated with varying the turbulence transition
values and the SOR iteration parameters including time step size have
already been discussed. The influence of other turbulence model para-
meters, far field boundary conditions, and grid fineness on the numerical
solutions have also been investigated.

The turbulence model contains several parameters which can vary.
The effects that changes in these parameters have on the flow field near
the airfoil surface and on the values of lift and drag were examined.
The value of the nominal inner eddy viscosity parameter k_1 was increased
by 20% at a 5° angle of attack. The lift coefficient subsequently
increased by 2% while the drag coefficient increased by 5% or six drag

2 OF 2
AD
A111279

END
DATE
FILMED
3-82
DTIC

counts. These integrated effects are caused by the observed small increase
of velocity in the inner boundary-layer on the upper surface. The outer
eddy viscosity parameter k_2 was next increased by 50%. The result was an
increase in turbulent mixing with a corresponding thicker boundary-layer.
The velocities near the edge of the upper surface boundary-layer decreased
which caused an 8% loss of lift with no apparent effect on the calculated
drag.

Values for the constants in the inner eddy viscosity parameter k_1
relaxation factor given by Equation 65 were obtained from a parametric
study at an angle of attack of 11.5°. This angle of attack was chosen
because the effects of the relaxation are significant only for angles of
attack near stall. A solution was initially computed without the relaxa-
tion factor f. The laminar separation bubble remained closed with
trailing edge separation beginning at mid-chord. The calculated values
for the lift and drag coefficients were 0.98 and 0.064, respectively. An
examination of the lift curve in Figure 34 reveals that this solution
exhibits the character of leading edge stall where an approximate linear
behavior is sustained until separation abruptly occurs. Leading edge stall
does occur for the NACA 0012 airfoil for Reynolds numbers greater than
about 500,000 (References 56, 89). Thus the mechanism for leading edge stall seems
present within the modified turbulence model. A numerical solution was
next obtained using the relaxation factor with a relaxation distance s_r =
0.25 and a delay distance s_d = 0. in nondimensional distances. The laminar
bubble remain closed, but the trailing edge separation region was signifi-
cantly larger and moved to within the 20% chord location (x = - 0.3). The
lift coefficient decreased substantially to a value of 0.8 while the drag
coefficient increased moderately to a value of 0.074. The final solution
which has been previously discussed was calculated using distances s_r =
0.5 and s_d = 0.1. The computed lift and drag coefficients became 0.84
and 0.068, respectively, and are in agreement with the experimental data.
The sensitivity of the numerical solution to these parameters has thus
been obtained. The last set of distance parameters was used in calcu-
lating the solutions for the other angles of attack. The onset of

trailing edge separation for the 5° and 7.5° solutions, seen in Figures 4 and 5, indicates that the relaxation factor was not activated. Thus, the relaxation model for parameter k_1 affects the flow field only near stall where the pressure gradient approaches zero over a large portion of the upper surface.

The relaxation distance WL_2 in the near wake turbulence model given by Equation 74 was also investigated. Numerical solutions were obtained at 5° angle of attack for relaxation distances equal to 5 and 100 times the lower surface boundary-layer thickness near the trailing edge. No changes in either the surface pressure distribution or the integrated force coefficients were observed. In two recent near wake calculations with similar relaxation models, Waskiewicz (Reference 98) used a value of 30 trailing edge boundary-layer thicknesses and Hasen (Reference 99) used 10 boundary-layer thicknesses. The relaxation distance of five boundary layer thicknesses was retained since the agreement of the Reynolds stress field discussed previously was improved for this choice.

The effect on the solution of the placement and type of far field boundary conditions should be considered in any computational work. In this investigation, two types of boundary conditions at different locations were examined. The four angle of attack solutions that have been discussed were computed using the freestream far field boundary conditions described in Sections III.2 and IV.3 at a circular outer boundary of radius 10 chords. The effect of the far field boundary placement on an inviscid solution for Joukowski airfoils was previously accomplished (Reference 82). This analysis indicated that a radius of 10 chords was sufficient as discussed in Section IV.3. The effect of the boundary placement on the present viscous solution was examined by using an alternate outer boundary. The $J = 40$ η contour with a semi-major x axis of 4.77 and semi-minor y axis of 4.64 was chosen as the new outer boundary because it approximates a circle with half the previous radius. The numerical solution was then obtained for $\alpha = 5°$ and compared with the solution using the 10 chord radius outer boundary. The average values for the

77

lift and drag coefficients were identical. The solution with the closer far field boundary had a small oscillatory behavior with variations in the lift and drag coefficients of 1% and 2%, respectively. Further examination of the near surface flow field revealed that the laminar separation bubble had a small scale unsteadiness which locally affected the pressure field.

The far field potential flow boundary condition model developed in Appendix F was next applied with the outer boundary locations of 10 chords and about five chords in turn. This model approximates the small perturbations from the freestream conditions for the velocity and pressure fields at a large but finite distance caused by the presence of a body in the flow field. In this approach, the upstream boundary conditions for both velocity and pressure became the calculated values from the inviscid potential flow model. The downstream boundary condition for pressure also became the corrected value rather than the freestream value. The no change downstream boundary condition for the velocity components was retained. The solution was calculated with the revised far field boundary conditions at the 10 chord radius circular outer boundary. The boundary conditions were initially updated every 200 time steps (0.2T) by using the latest calculated value of the circulation. After three characteristic time periods T, the mean values of the lift and drag coefficients were virtually identical with the previous freestream boundary condition results. However, while the lift coefficient had variations of less than 1% from the mean value, the calculated drag coefficient was periodic with a period of 0.4T and variations of $\pm$ 10%. Since the period of the oscillations was twice the period of the boundary condition update and the circulation was essentially a constant at this time, the outer boundary conditions (except the no change downstream condition) were kept at the current values and the solution was advanced 1.5 characteristic time periods. At this time, the lift coefficient had a steady value of 0.425 and the drag coefficient became 0.011 $\pm$ 2% (two drag counts). These computed results are within 1% of the corresponding coefficients calculated from the solution using the simple freestream conditions.

Thus the more accurate boundary condition which includes the effect of a finite distance from the body induces very small changes in the computed flow field near the airfoil.

The modified far field potential flow boundary, conditons were also used at the near-circular five chord radius outer boundary defined previously to obtain a solution again for $\alpha = 5°$. After two characteristic times, the outer modified freestream boundary conditions were held constant since the lift coefficient had small variations less than 1%. The solution exhibited a small oscillatory behavior similar to the freestream boundary condition result even after four characteristic time periods. The lift coefficient had a mean value within 1% of the freestream boundary condition value with variations below 1%. The drag coefficient had the same average value as the previous result, but the oscillations were larger with a deviation from the mean of approximately $\pm$ 10% (10 drag counts). The unsteadiness was again observed to emanate from the laminar separation bubble. Small pressure oscillations propagated downstream on the upper surface of the airfoil and were eventually damped out near the trailing edge. In each case no changes were made in any of the turbulence or other parameters during the computations. Small changes in the turbulence transition near the bubble would probably prevent the unsteadiness.

The far field boundary condition study has indicated that the use of the freestream boundary conditions at the large but finite distance from the airfoil surface is sufficient for the computation of the near surface flow field and force coefficients. Variations in the outer boundary placement and the use of a more accurate far field boundary condition had negligible effects on the present numerical solution.

The numerical implementation of the downstream no change boundary condition was also investigated. Second order accurate central spatial and upwind differences were used in separate solutions for an angle of attack of 7.5°. No difference ($\pm$0.01%) was observed in the surface pressure distributions or computed force coefficients between the two boundary conditions. The computed velocities at locations across the wake on

the outer boundary for the two cases differed by less than 1%. The upwind
difference formulation was chosen because of the associated convective
properties.

The sensitivity of the numerical solution to the fineness of the
grid was examined. The 7.5° angle of attack case was chosen because
both the laminar separation bubble and a region of separated flow near
the trailing edge are present. A coarse grid was obtained from the 79x44
grid by deleting the odd numbered η contours except for the body contour.
The coarse 79x23 grid was a subset of the full coordinate system and was
used to study the effect of boundary-layer resolution on the numerical
solution. The turbulence parameters and SOR acceleration parameters were
unchanged from the previous solution. The coarse grid computation was
carried out over four characteristic time periods. The calculated values
for the lift and drag coefficients approached a "steady" periodic state
after two characteristic times with a period of 0.6T. The mean value of
the lift coefficient, averaged over the last two characteristic times,
became 0.606 $\pm$ 2% compared with the full grid solution value of 0.606.
The computed mean drag coefficient was 0.0260 $\pm$ 15% compared with the
79x44 grid solution result of 0.0240. Values for the wake velocities in
the freestream direction along the outer boundary for each solution
compared within 1%. The unsteadiness was found to originate from the
oscillating laminar separating shear layer which forms the front portion
of the bubble. The edge of the boundary-layer varied between the J=3
and J=4 η contours, as defined by the 79x23 grid system, at the 1% chord
location. This motion also caused the bubble to vary in length and produced
pressure oscillations along the upper surface. This unsteadiness is
probably attributed to the reduced resolution of the bubble in the η
direction. Similar sensitivity has already been discussed concerning
the resolution of the extremely short bubble in the ξ direction at
larger angles of attack.

The computed flow field near the airfoil and the calculation of the force coefficients using the coarse grid are in agreement with the results for the complete 79x44 grid. A quadratic Richardson's extrapolation on the computed drag coefficients indicates an error of +0.0007. This agreement indicates that the solution obtained with the full 79x44 coordinate system is adequate to obtain ±10 drag counts and therefore sufficiently approximates the limiting numerical solution obtained from an extremely fine grid. The coarse grid computation further indicates that the numerical multi-grid approach (Reference 100) may be implemented for complex flows using general grid transformations. The use of only one-half the grid points, for instance, during most of the time marching procedure, would significantly reduce the computer time required for an equivalent numerical solution.

SECTION VI

CONCLUSIONS AND RECOMMENDATIONS

Numerical solutions have been obtained for two-dimensional incompressible turbulent flow over airfoils near stall. The time dependent Reynolds averaged incompressible Navier-Stokes equations in the primitive variables of velocity and pressure together with a Poisson pressure equation are numerically solved. An algebraic eddy viscosity approach is modified for separated adverse pressure gradient flows and used to model turbulent closure of the laminar separation bubble and the subsequent turbulent boundary-layer. A deficiency in the standard model is detected and corrected by using a "limiting" technique. A body-fitted coordinate system is numerically transformed to a rectangular grid in the computational plane. The set of transformed partial differential equations is solved with an implicit finite difference method. Successive-over-relaxation iteration is used to solve the system of linearized difference equations at each time step.

Numerical solutions are presented for a NACA 0012 airfoil near stall at a chord Reynolds number of 170,000. A short laminar separation bubble located near the upper surface suction pressure peak is obtained. Computed laminar separation bubble characteristics including the criteria for separation, bubble type, and turbulent transition agree with empirical results. Surface mean pressure distributions are presented and found to compare favorably with experimental data. The separation bubble is observed for angles of attack of 5° and 7.5°. For larger angles of attack, the small bubble essentially disappeared within the numerical resolution of the streamwise grid spacing. The steep leading edge suction pressure peak is well defined for each angle of attack. Velocity profiles at four stations along the upper airfoil surface are compared with experimental results. The experimental data were obtained at similar grid point locations so that interpolation was not required. The calculated lift and drag coefficients are in excellent agreement with the experimental data. The lift coefficients are within 5% of the experimental values

82

near stall, and the computed drag coefficients are within ten drag counts in the region of maximum lift to drag ratio. The effects of viscous separation on the lift coefficient curve which produces a maximum value are seen and contrasted with a numerically obtained inviscid potential solution with Kutta condition. The observed phenomena of trailing edge stall is predicted where the rear separation point moves forward with increasing angle of attack.

The sensitivity of the numerical solution has been examined in several areas. A far field potential flow boundary condition which modifies the freestream conditions for use at a large but finite distance from the airfoil was considered for two outer boundary placements. The study showed that the use of the infinite freestream conditions at an outer circular boundary of radius ten chords produces negligible influence on the near flow field and calculated values for the force coefficients. A coarse 79x23 grid, compared with the 79x44 grid, was used to evaluate truncation error. An analysis of convergence for successive-over-relaxation iteration predicts an upper limit on the time increment for the implicit finite difference method. Numerical experiments confirmed this upper bound. Several parameters within the turbulence model were systematically varied. The only significant sensitivity occurred near the downstream side of the laminar separation bubble. Small changes in turbulent transition length and location were found to significantly change the flow field. This sensitivity may be related to incipient turbulent separation which results in failure to close the separation bubble. This leading edge stall phenomena is observed at higher Reynolds numbers for the NACA 0012 airfoil.

The agreement between the numerical solutions and the experimental data and empirical results indicates that the eddy viscosity approach modified for separated adverse pressure gradient flows adequately models the turbulence on the upper airfoil surface. The near stall airfoil aerodynamic characteristics are consequently accurately predicted by the numerical method.

The results of this investigation have suggested areas for further research. A more exhaustive study of the laminar separation bubble should be accomplished to better understand the phenomena of leading edge stall. The computation of a geometry with detailed experimental results for this purpose is desirable. Further research in adapting the multi-grid technique would significantly increase the computational efficiency and appears feasible as a result of the coarse grid calculation. Turbulence modelling is an area of substantial interest and should be pursued in conjunction with experimental investigations. The improved accuracy of current computational aerodynamics also indicates that the errors in experimental measurements should be analyzed in a more rigorous manner so that comparisons can be better evaluated. The method should also be employed in time dependent problems to further exploit the time marching technique.

REFERENCES

1. Alan M. Winslow, "Numerical Solution of the Quasilinear Poisson Equation in a Nonuniform Triangle Mesh," _J. Comp Phys._, 1 (1966), 149.

2. Wen-Hwa Chu, "Development of a General Finite Difference Approximation for a General Domain, Part I: Machine Transformation," _J. Comp. Phys._, 8 (1971), 392.

3. A. Amsden and C. Hirt, "A Simple Scheme for Generating General Curvilinear Grids," _J. Comp. Phys._, 11 (1973), 348.

4. J. F. Thompson, F. C. Thames, and C. W. Mastin, "Automatic Numerical Generation of Body-Fitted Curvilinear Coordinate System for Fields Containing Any Number of Arbitrary Two-Dimensional Bodies," _J. Comp. Phys._, 15 (1974), 299.

5. J. F. Thompson, F. C. Thames, and C. W. Mastin, "Boundary-Fitted Curvilinear Coordinate Systems for Solution of Partial Differential Equations on Fields Containing Any Number of Arbitrary Two-Dimensional Bodies," NASA-CR-2729, 1977.

6. J. F. Thompson, F. C. Thames, and C. W. Mastin, "TOMCAT- A Code for Numerical Generation of Boundary-Fitted Curvilinear Coordinate Systems on Fields Containing Any Number of Arbitrary Two-Dimensional Bodies," _J. Comp. Phys._, 24 (1977), 274.

7. J. K. Hodge and A. L. Stone, "Numerical Solution for Airfoils Near Stall in Optimized Boundary-Fitted Curvilinear Coordinates," _AIAA J._ 17 (1979), 458.

8. J. L. Steger and R. L. Sorenson, "Automatic Mesh-Point Clustering Near a Boundary in Grid Generation with Elliptic Partial Differential Equations," _J. Comp. Phys._, 33 (1979), 405.

9. R. L. Sorenson, "A Computer Program to Generate Two-Dimensional Grids About Airfoils and Other Shapes by the Use of Poisson's Equation," NASA-TM-81198, 1980.

10. C. W. Mastin and J. F. Thompson, "Three-Dimensional Body-Fitted Coordinate Systems for Numerical Solution of the Navier-Stokes Equations," AIAA Paper 78-1147, 1978.

11. R. Meyder, "Solving the Conservation Equations in Fuel Rod Bundles Exposed to Parallel Flow by Means of Curvilinear-Orthogonal Coordinates," _J. Comp. Phys._, 17 (1975), 53.

12. T. Theodorsen and I. E. Garrick, "General Potential Theory of Arbitrary Wing Sections," NACA-TR-452, 1933.

13. David C. Ives, "A Modern Look at Conformal Mapping Including Multiply Connected Regions," AIAA J., 14 (1976), 1006.

14. H. J. Gibeling, S. J. Shamroth, and P. R. Eiseman, "Analysis of Stong-Interaction Dynamic Stall for Laminar Flow on Airfoils," NASA-CR-2969, 1978.

15. Peter R. Eiseman, "A Coordinate System for a Viscous Transonic Cascade Analysis," J. Comp. Phys., 26 (1978), 307.

16. Peter R. Eiseman, "A Multi-Surface Method of Coordinate Generation," J. Comp. Phys., 33 (1979), 118.

17. Peter R. Eiseman, "Coordinate Generation with Precise Controls," ICASE Rept 80-16, 1980.

18. J. Boussinesq, "Theorie de l'ecoulement tourbillant," Mem. Pres. Acad. Sci. XXIII, 46 (1877).

19. L. Prandtl, "Bericht über Untersuchungen zur ausgebildeten Turbulenz," ZAMM, 5 (1925), 136.

20. T. Cebeci and A. M. O. Smith, article from Computation of Turbulent Boundary Layers, AFOSR-IFP Conf., 1 (1968), Stanford Univ. Press, 346.

21. G. L. Mellor and H. J. Herring, "Two Methods of Calculating Turbulent Boundary Layer Behavior Based on Numerical Solutions of the Equations of Motion", Computations of Turbulent Boundary Layers, AFOSR-IFP Conf., 1 (1968), Stanford Univ. Press, 331.

22. S. V. Patankar and D. B. Spalding, article from Computations of Turbulent Boundary Layers, AFOSR-IFP Conf., 1 (1968), Stanford Univ. Press, 356.

23. E. R. Van Driest, "On Turbulent Flow Near a Wall," J. Aerospace Sci., 23 (1956), 1007.

24. T. Cebeci and A. M. O. Smith, Analysis of Turbulent Boundary Layers, Academic Press, NY, 1974.

25. B. E. Launder and D. B. Spalding, Mathematical Models of Turbulence, Academic Press, NY, 1972.

26. L. Prandtl, "Über ein neues Formelsystem für die ausgebildete Turbulenz," Nachrichten von der Akad. der Wissenshaften in Gottingen, (1945), 6.

27. G. S. Glushko, "Turbulent Boundary Layer on a Flat Plate in an Incompressible Fluid," NASA-TM-F-10080, 1966.

28. G. L. Mellor and H. J. Herring, article from Computations of Turbulent Boundary Layers, AFOSR-IFP Stanford Conf., 1 (1968), Stanford Univ. Press, 247.

29. M. Wolfshtein, "The Velocity and Temperature Distribution in One-Dimensional Flow with Turbulence Augmentation and Pressure Gradient," Int. J. Heat Mass Transfer, 12 (1969), 301.

30. P. Bradshaw, D. Ferriss, and N. Atwell, "Calculation of Boundary-Layer Development Using the Turbulence Energy Equation," J. Fluid Mech., 28 (1967), 593.

31. V. Nee and L. Kovasznay, "Simple Phenomenological Theory of Turbulent Shear Flows," J. Phys. Fluids, 12 (1969), 473.

32. A. N. Kolmogorov, "Equations of Turbulent Motion in an Incompressible Fluid," IZV Akad. Nauk. SSSR, Ser. Fiz., 6 (1942), 56.

33. K. H. Ng and D. B. Spalding, "Turbulence Model for Boundary Layer Near Walls," J. Phys. Fluids, 15 (1972), 20.

34. J. C. Rotta, "Statistiche Theorie nichthomogener Turbulenz," Z. Phys., 129 (1951), 546.

35. P. Saffman, "A Model for Inhomogeneous Turbulent Flow," Proc. Roy. Soc. London, 317 (1970), 417.

36. D. Wilcox and M. Rubesin, "Progress in Turbulence Modeling for Complex Flow Fields Including Effects of Compressibility." NASA-TP-1517, 1980.

37. W. Jones and B. Launder, "The Prediction of Laminarization with a Two-Equation Model of Turbulence." Int. J. Heat Mass Transfer, 15 (1972), 301.

38. C. Donaldson and H. Rosenbaum, "Calculation of Turbulent Shear Flows Through Closure of the Reynolds Equations by Invariant Modeling," NASA-CR-128172, 1968.

39. K. Hanjalic and B. Launder, "A Reynolds Stress Model of Turbulence and its Application to Thin Shear Layers," J. Fluid Mech., 52 (1972), 609.

40. B. Kolovandin and I. Vatutin, "Statistical Transfer Theory in Non-homogeneous Turbulence," Int. J. Heat Mass Transfer, 15 (1972), 2371.

41. J. Ferziger, "Large Eddy Numerical Simulations of Turbulent Flows," AIAA J., 15 (1977), 1261.

42. R. Walker, "Numerical Solution of the Navier-Stokes Equations for Incompressible Viscous Laminar Flow Past a Semi-Infinite Flat Plate," MS Thesis, Mississippi State University, 1974.

43. Shih Pai, Viscous Flow Theory, Part I Laminar Flow, D. Van Nostrand, NY, 1956.

44. F. Thames, "Numerical Solution of the Incompressible Navier-Stokes Equations about Arbitrary Two-Dimensional Bodies," Ph D Dissertation, Mississippi State University, 1975.

45. U. Mehta and Z. Lavan, "Starting Vortex, Separation Bubbles, and Stall: A Numerical Study of Laminar Unsteady Flow Around an Airfoil," J. Fluid Mech., 67 (1975), 227.

46. R. Reddy and J. Thompson, "Numerical Solution of Incompressible Navier-Stokes Equations in the Integro-Differential Formulation Using Boundary-Fitted Coordinate Systems," AIAA Paper 77-650, 1977.

47. N. Sankar and J. C. Wu, "Viscous Flow Around Oscillating Airfoils - A Numerical Study," AIAA Paper 78-1225, 1978.

48. N. Sankar and Y. Tassa, "Reynolds Number and Compressibility Effects on Dynamic Stall of a NACA 0012 Airfoil," AIAA Paper 80-0010, 1980.

49. W. Briley and H. McDonald, "Solution of the Multidimensional Compressible Navier-Stokes Equations by a Generalized Implicit Method," J. Comp. Phys., 24 (1977), 372.

50. A. Sugavanam and J. Wu, "Numerical Study of Separated Turbulent Flow Over Airfoils," AIAA Paper 80-1441, 1980.

51. F. Harlow and J. Welch, "Numerical Calculation of Time-Dependent Viscous Incompressible Flow of Fluid with Free Surface," Phys. of Fluids, 8 (1965), 2182.

52. C. Hirt and F. Harlow, "A General Corrective Procedure for the Numerical Solution of Initial Value Problems," J. Comp. Phys., 2 (1967), 114.

53. J. K. Hodge, "Numerical Solution of Incompressible Laminar Flow About Arbitrary Bodies in Body-Fitted Curvilinear Coordinates," Ph D Dissertation, Mississippi State University, 1975.

54. K. Ghia, W. Hankey, and J. Hodge, "Study of Incompressible Navier-Stokes Equations in Primitive Variables Using Implicit Numerical Technique," AIAA Paper 77-0648, 1977.

55. J. Chien, Vorticity-Stream Function Formulation of Compressible and Incompressible Turbulent Internal Flows, AEDC-TR-79-13, 1979.

56. E. Jacobs and A. Sherman, Airfoil Characteristics as Affected by Variations of the Reynolds Number, NACA Rept 586, 1937.

57. G. Deiwert, "Numerical Simulation of High Reynolds Number Transonic Flows," AIAA J., 13 (1975), 1354.

58. R. W. MacCormack and A. Paullay "Computational Efficiency Achieved by Time Splitting of Finite Difference Operators," AIAA Paper 72-154, 1972.

59.   J. Steger, "Implicit Finite Difference Simulation of Flow About Arbitrary Two-Dimensional Geometries", AIAA J., 16 (1978), 679.

60.   R. Beam and R. Warming, "An Implicit Finite Difference Algorithm for Hyperbolic Systems in Conservative-Law-Form," J. Comp. Phys., 22 (1976), 87.

61.   L. Walitt, L. King, and C. Liu, "Computation of Viscous Transonic Flow About a Lifting Airfoil," AIAA Paper 77-679, 1977.

62.   J. Trulio, Theory and Structure of the AFTON Codes, AFWL-TR-66-19, 1966.

63.   T. Cebeci, A. M. O. Smith and G. Mosinskis, "Calculations of Compressible Adiabatic Turbulent Boundary Layers," AIAA J., 8 (1970), 1974.

64.   S. Shamroth and H. Gibeling, "A Compressible Solution of the Navier-Stokes Equations for Turbulent Flow About an Airfoil," NASA-CR-3183, 1979.

65.   K. McAlister, L. Carr, and W. McCroskey, Dynamic Stall Experiments on the NACA 0012 Airfoil, NASA-TP-1100, 1978.

66.   S. Bland, AGARD Two-Dimensional Aeroelastic Configurations, AGARD-AR-156, 1979.

67.   I. Abbott and A. Von Doenhoff, Theory of Wing Sections, Dover Pub., NY, 1959.

68.   A. Chorin, "Numerical Solution of the Navier-Stokes Equations," Math. Comp., 22 (1968), 745.

69.   J. Shang, W. Hankey, and D. Dwoyer, Compressible Turbulent Boundary Layer Solutions Employing Eddy Viscosity Models, ARL 73-0041, 1973.

70.   D. Coles, "The Law of the Wake in the Turbulent Boundary Layer," J. Fluid Mech., 1 (1956), 191.

71.   C. Jobe and W. Hankey, "Turbulent Boundary Layer Calculations in Adverse Pressure Gradient Flows," AIAA Paper 80-136, 1980.

72.   G. McCullough and D. Gault, Examples of Three Representative Types of Airfoil Section Stall at Low Speed, NACA-TN-2502, 1951.

73.   W. Bachalo and D. Johnson, "An Investigation of Transonic Turbulent Boundary Layer Separation Generated on an Axisymmetric Flow Model", AIAA paper 79-1479, 1979.

74.   A. Baker and J. Orzechowski, An Interaction Algorithm for Prediction of Mean and Fluctuating Velocities in Two-Dimensional Aerodynamic Wake Flows, NASA-CR-3301, 1980.

75. S. Dhawan and R. Narasimha, "Some Properties of Boundary-Layer Flow During the Transition from Laminar to Turbulent Motion," J. Fluid Mech., 3 (1958), 418.

76. R. Narasimha and A. Prabhu, "Equilibrium and Relaxation in Turbulent Wakes," J. Fluid Mech., 54 (1972), 1.

77. J. Green, D. Weeks, and J. Brooman, Prediction of Turbulent Boundary Layers and Wakes in Compressible Flow by a Lag-Entrainment Method, ARC-R/M-3791, 1977.

78. M. Inouye, J. Marvin, and Y. Sheaffer, "Turbulent-Wake Calculations with an Eddy-Viscosity Model," AIAA J., 10 (1972), 216.

79. O. R. Burggraf, Comparative Study of Turbulence Models for Boundary Layers and Wakes, ARL-74-31, 1974.

80. P. Bradshaw, R. Dean, and D. McEligot, "Calculation of Interacting Turbulent Shear Layers: Duct Flow," Trans. ASME, Series I: J. Fluids Eng., 95 (1973), 214.

81. R. Varga, Matrix Iterative Analysis, Prentice-Hall, New Jersey, 1962.

82. U. Ghia, J. Hodge, and W. Hankey, An Optimization Study for Generating Surface-Oriented Coordinates for Arbitrary Bodies in High-Re Flow, AFFDL-TR-77-117, 1977.

83. P. Roache, Computational Fluid Mechanics, Hermosa Publishers, NM, 1976.

84. Harwood A. Hegna, "The Numerical Solution of Incompressible Turbulent Flow Over Airfoils," Ph D Dissertation, AF Institute of Technology, 1981.

85. D. Gault, An Experimental Investigation of Regions of Separated Laminar Flow, NACA-TN-3505, 1955.

86. M. Gaster, The Structure and Behavior of Laminar Separation Bubbles, ARC-R/M-3595, 1969.

87. D. Hoad, W. Young, and J. Meyers, Velocity Measurements about a NACA 0012 Airfoil with a Laser Velocimeter, NASA Langley Rept, 1978.

88. A. Arena and T. Mueller, "Laminar Separation, Transition, and Turbulent Reattachment Near the Leading Edge of Airfoils," AIAA J., 18 (1980), 747.

89. N. Gregory and C. O'Reilly, Low-Speed Aerodynamic Characteristics of NACA 0012 Airfoil Section, Including the Effects of Upper-Surface Roughness Simulating Hoar Frost, ARC-R/M-3726, 1973.

90.   R. Wallis, "Boundary-Layer Transition at the Leading Edge of Thin Wings and its Effect on General Nose Separation," ICAS 2nd Congress, Zurich, 1960.

91.   N. Curle and S. Skan, "Approximate Methods for Predicting Separation Properties of Laminar Boundary Layers," Aero. Quarterly, 8 (1957), 257.

92.   P. Owen and L. Klanfer, On the Laminar Boundary Layer Separation from the Leading Edge of a Thin Aerofoil, RAE Rept 2508, 1953.

93.   L. Crabtree, The Formation of Regions of Separated Flow on Wing Surfaces, ARC-R/M-3122, 1957.

94.   L. Crabtree, "Prediction of Transition in the Boundary Layer on an Aerofoil," J. Royal Aero. Soc., 62 (1958), 525.

95.   W. Roberts, "Calculation of Laminar Separation Bubbles and Their Effect on Airfoil Performance," AIAA J., 18 (1980), 25.

96.   D. Coles and A. Wadcock, "A Flying-Hot-Wire Study of Two-Dimensional Mean Flow Past a NACA 4412 Airfoil at Maximum Lift," AIAA Paper 78-1196, 1978.

97.   A. Pope and J. Harper, Low Speed Wind Tunnel Testing, John Wiley and Sons, NY, 1966.

98.   J. Waskiewicz, J. Shang, and W. Hankey, "Numerical Simulation of Near Wakes Utilizing a Relaxation Turbulence Model", AIAA Paper 79-148, 1979.

99.   G. Hasen, "Navier-Stokes Solutions for an Axisymmetric Nozzle with a Thick Base Annulus in Supersonic Flow," Ph D Dissertation, Air Force Institute of Technology, to be published.

100.   A. Brandt, "Multi-Level Adaptive Computations in Fluid Dynamics," AIAA Paper 79-1455, 1979.

101.   E. B. Klunker, Contribution to Methods for Calculating the Flow About Thin Lifting Wings at Transonic Speeds - Analytic Expressions for the Far Field, NASA-TN-D-6530, 1971.
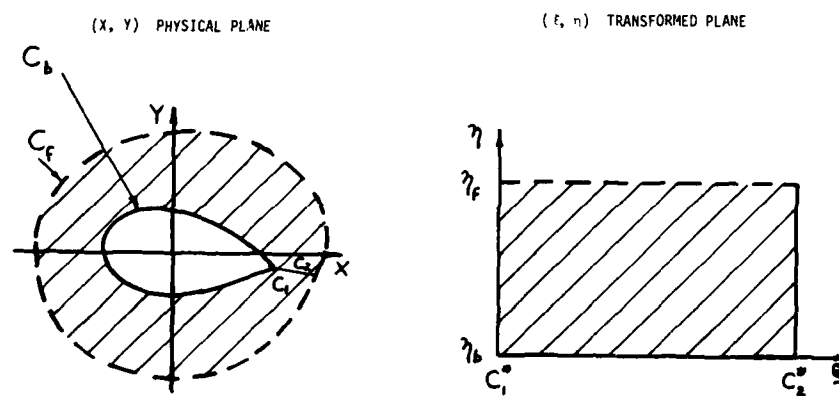
Figure 1. Physical and Transformed Planes
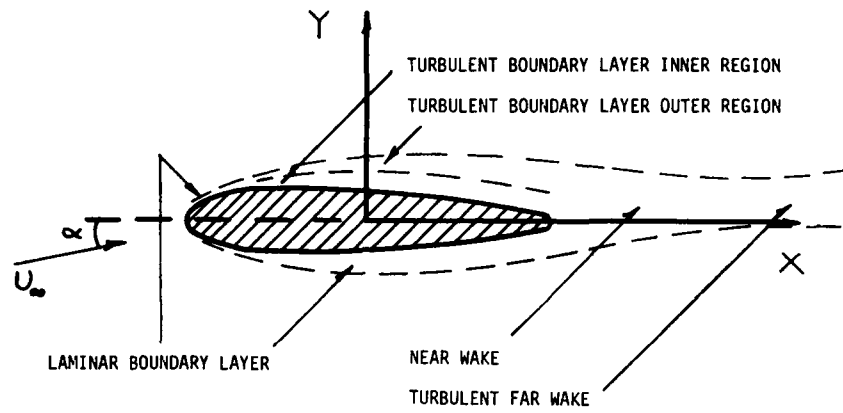
Figure 2. Regions of Turbulent Flow
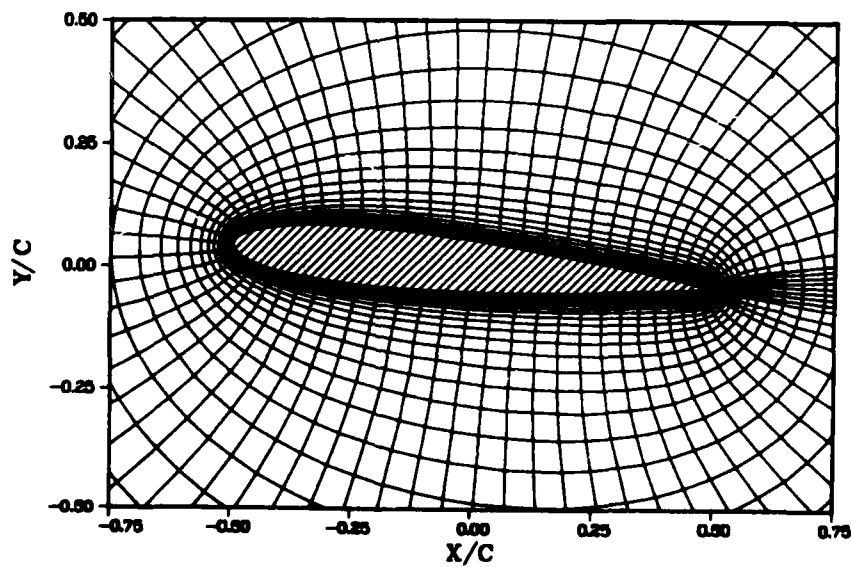
Figure 3. Portion of 79x44 Body-Fitted Grid (First 30
Constant η Lines)

93
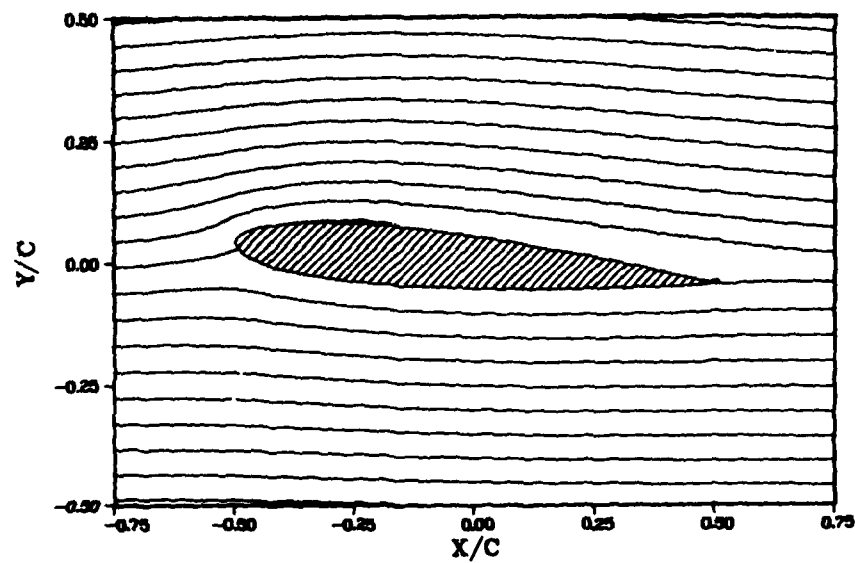
Figure 4. Mean Flow Streamline Contours ($\alpha = 5°$)
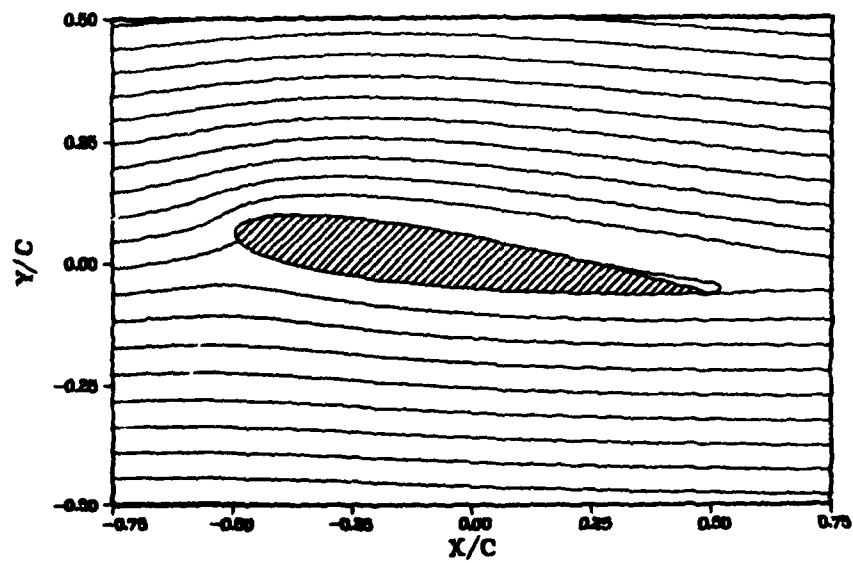
Figure 5. Mean Flow Streamline Contours ($\alpha = 7.5°$)
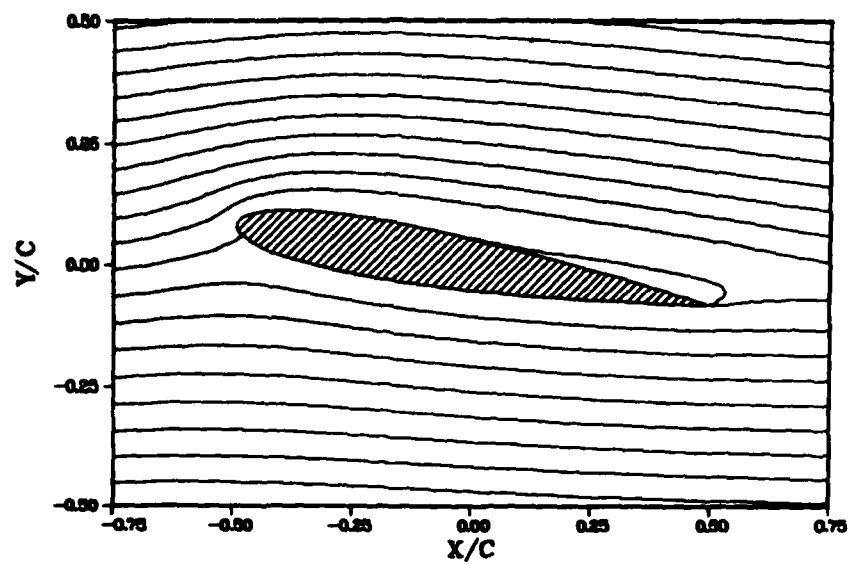
Figure 6.   Mean Flow Streamline Contours (α = 9.5°)
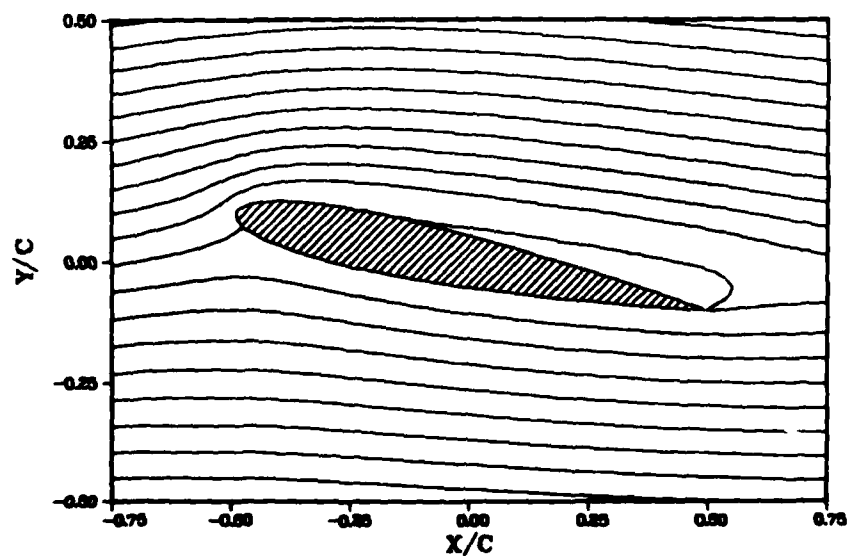
Figure 7.   Mean Flow Streamline Contours (α = 11.5°)
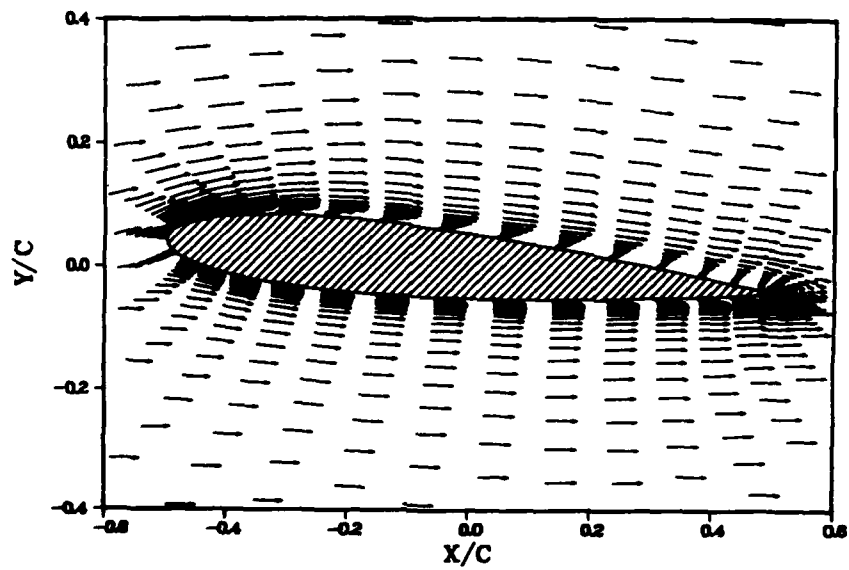
Figure 8. Mean Flow Velocity Field ($\alpha = 5°$)
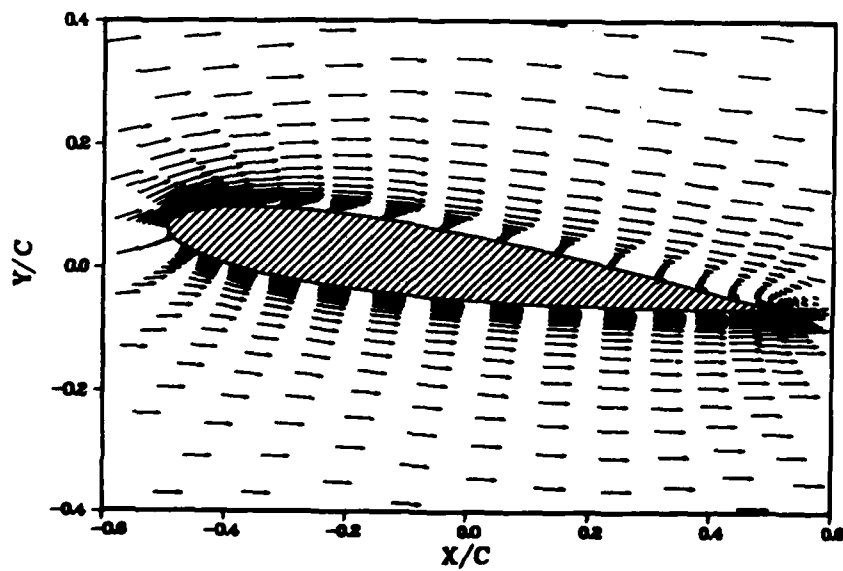
Figure 9. Mean Flow Velocity Field ($\alpha = 7.5°$)
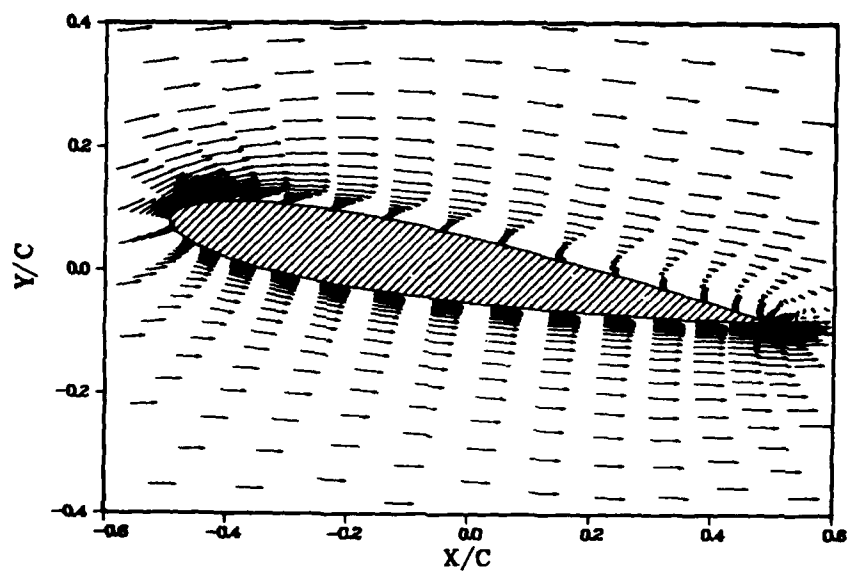
Figure 10. Mean Flow Velocity Field (α = 9.5°)
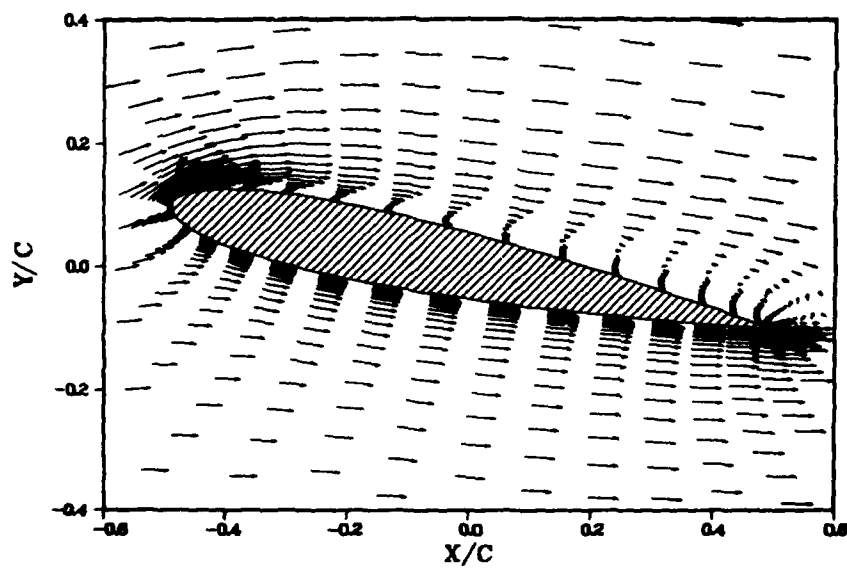
Figure 11. Mean Flow Velocity Field (α = 11.5°)
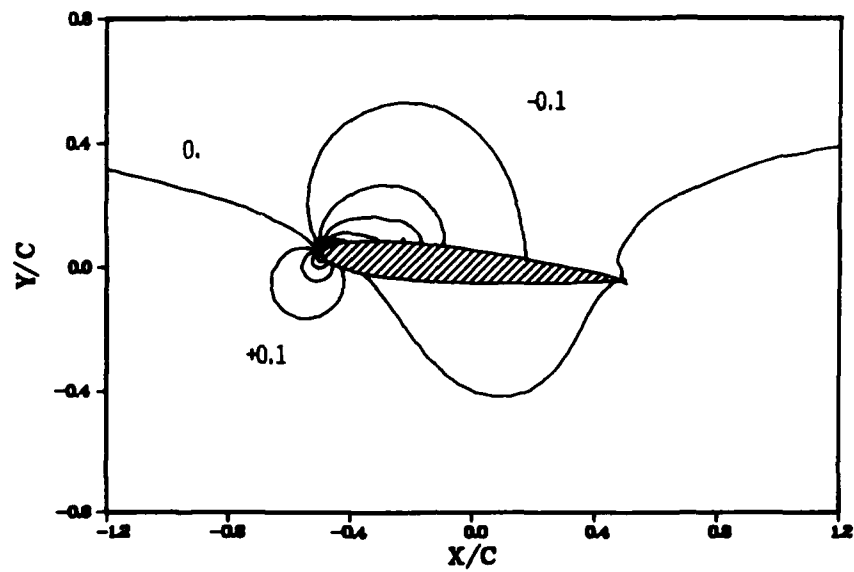
Figure 12. Mean Flow Pressure Contours (α = 5°)
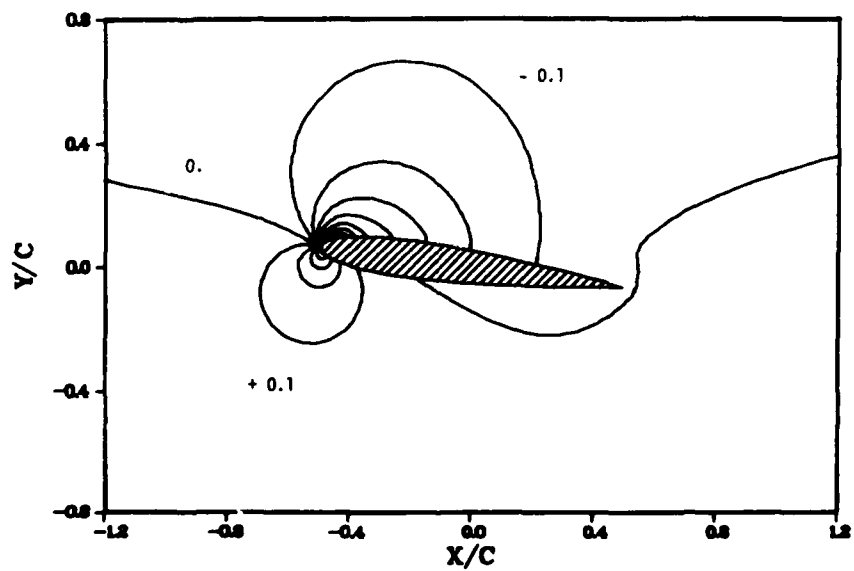
Figure 13. Mean Flow Pressure Contours (α = 7.5°)
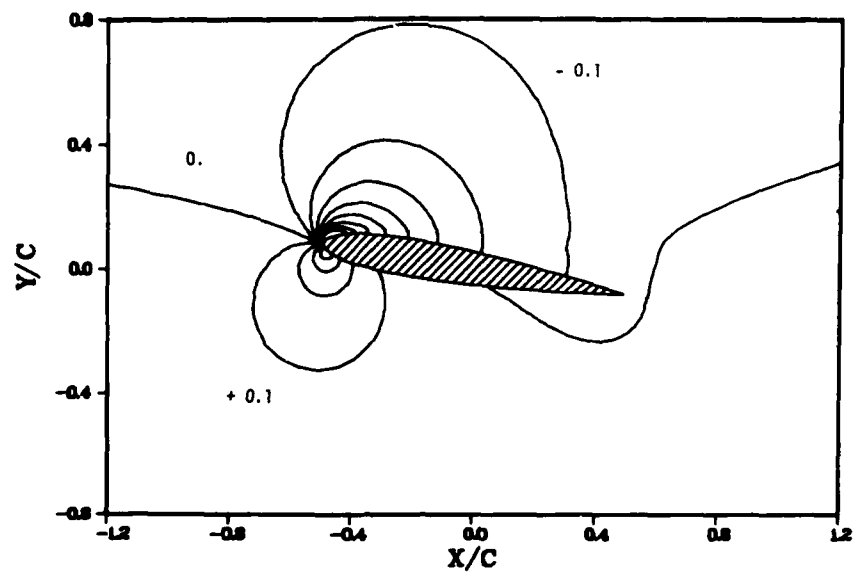
Figure 14. Mean Flow Pressure Contours (α = 9.5°)
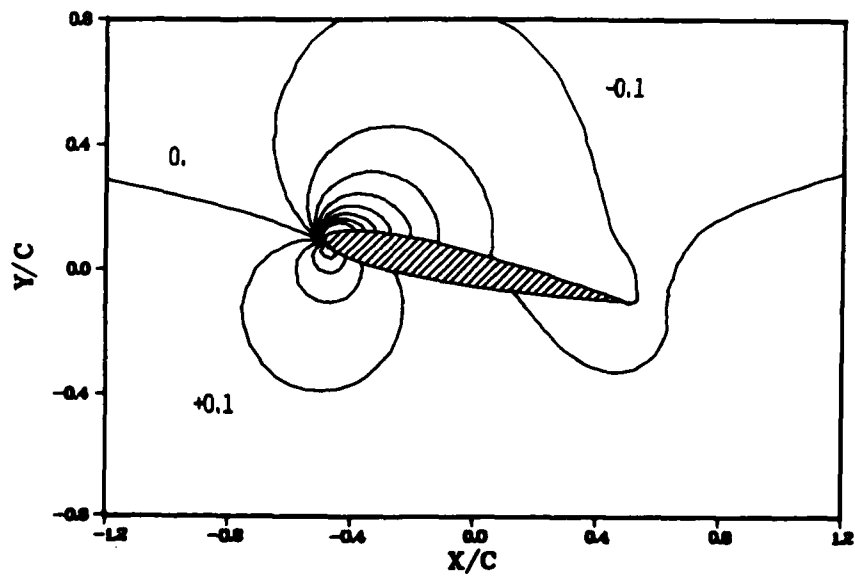
Figure 15. Mean Flow Pressure Contours (α = 11.5°)
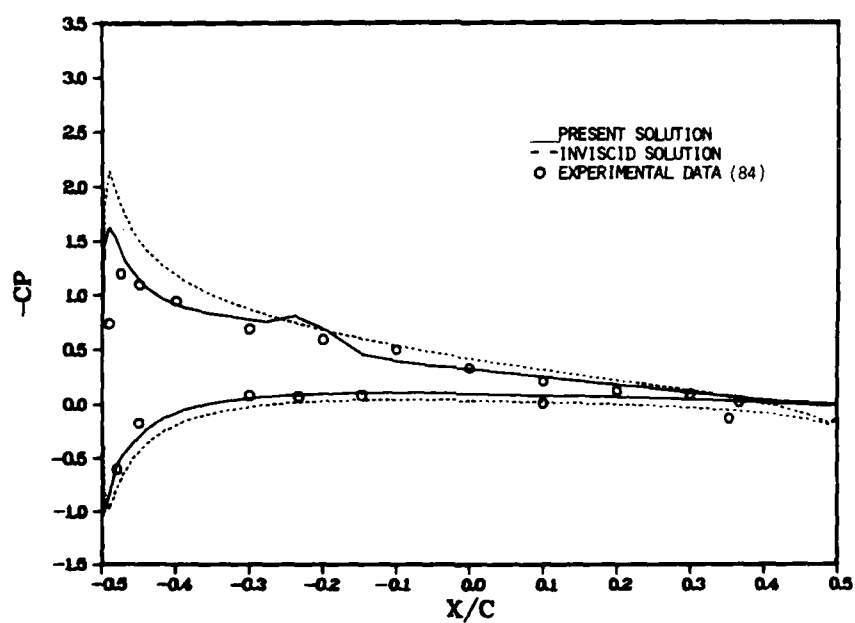
Figure 16.   Surface Mean Pressure Coefficients (α = 5°)
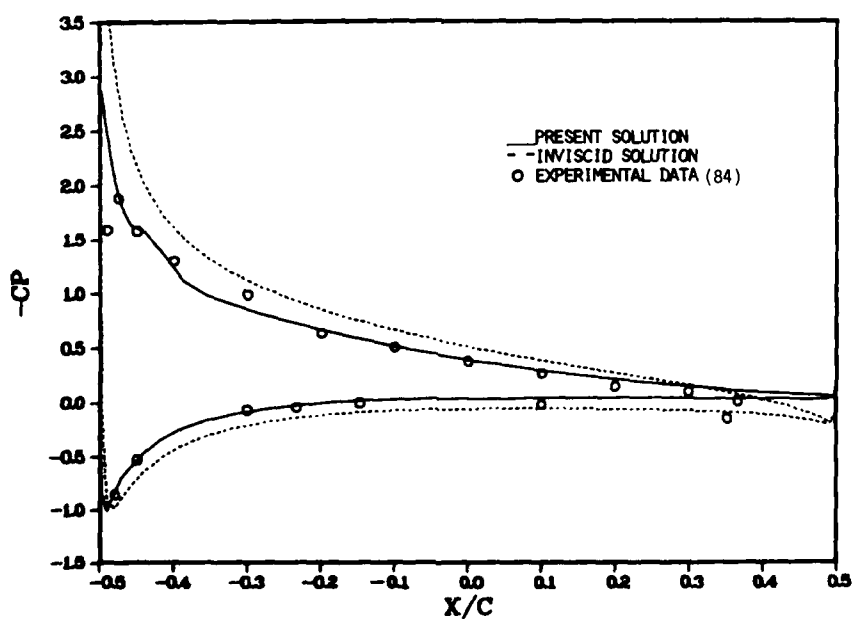
Figure 17.   Surface Mean Pressure Coefficients (α = 7.5°)
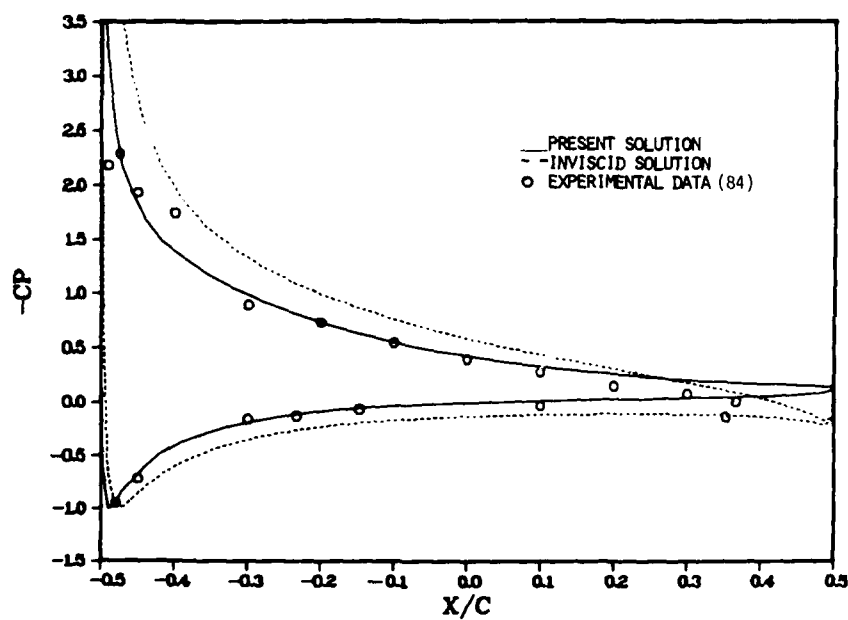
Figure 18.   Surface Mean Pressure Coefficients (α = 9.5°)
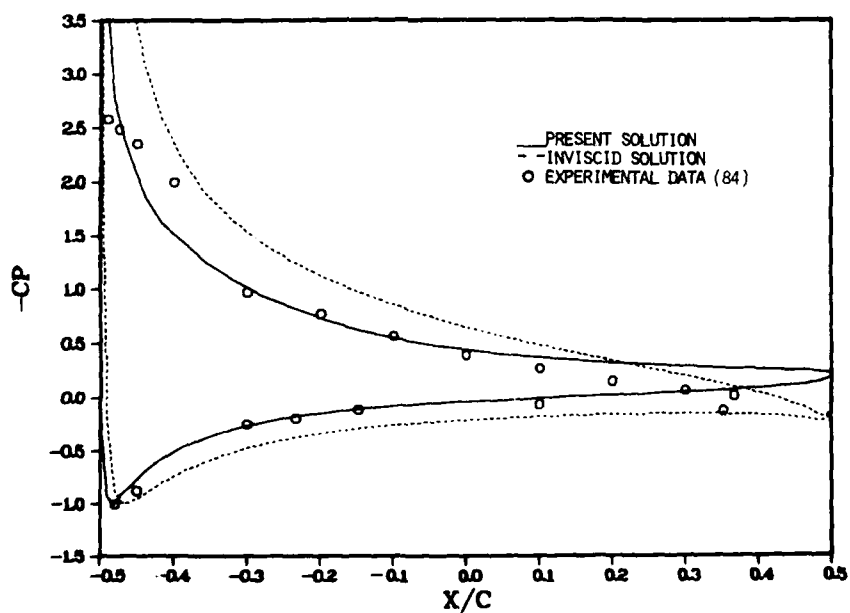
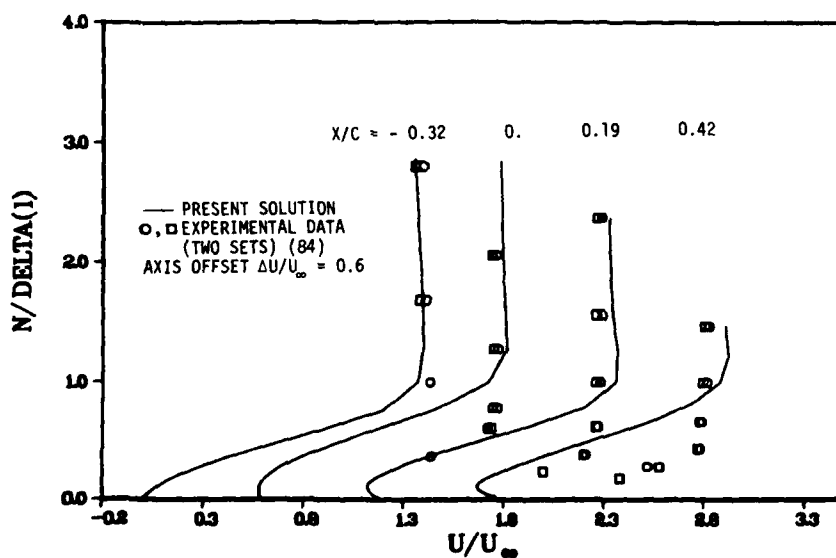Figure 19.   Surface Mean Pressure Coefficients (α = 11.5°)
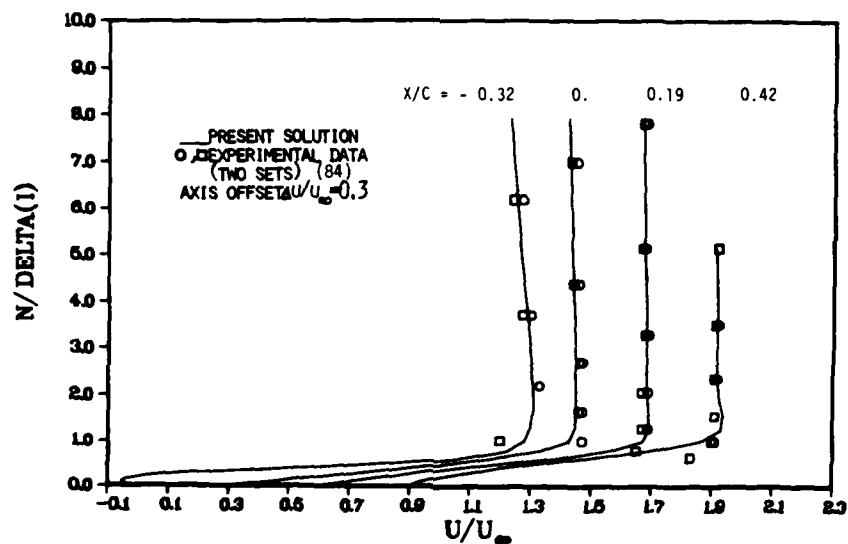
Figure 20. Mean Flow Velocity Versus Surface Normal Distance
Nondimensionalized by Computed Boundary-Layer Thick-
ness at Chord Locations on Upper Surface (α = 5°)
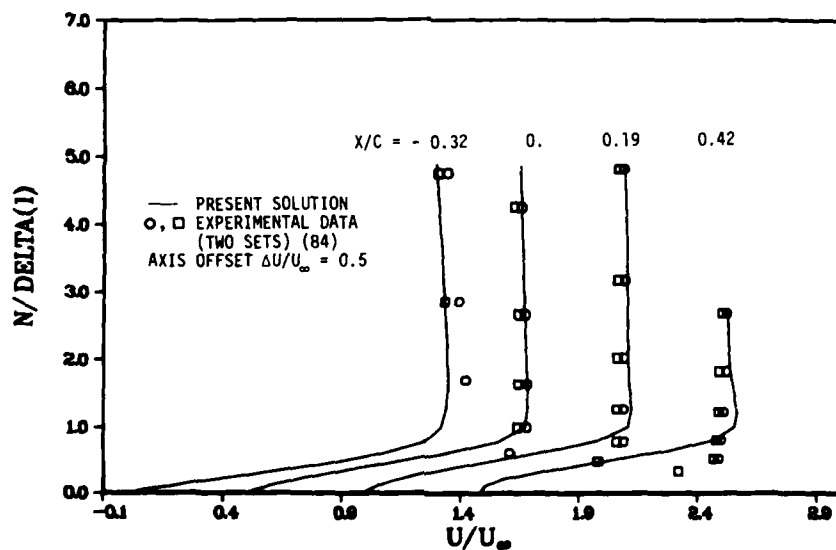
Figure 21. Mean Flow Velocity Versus Surface Normal Distance
Nondimensionalized by Computed Boundary-Layer Thick-
ness at Chord Locations on Upper Surface (α = 7.5°)
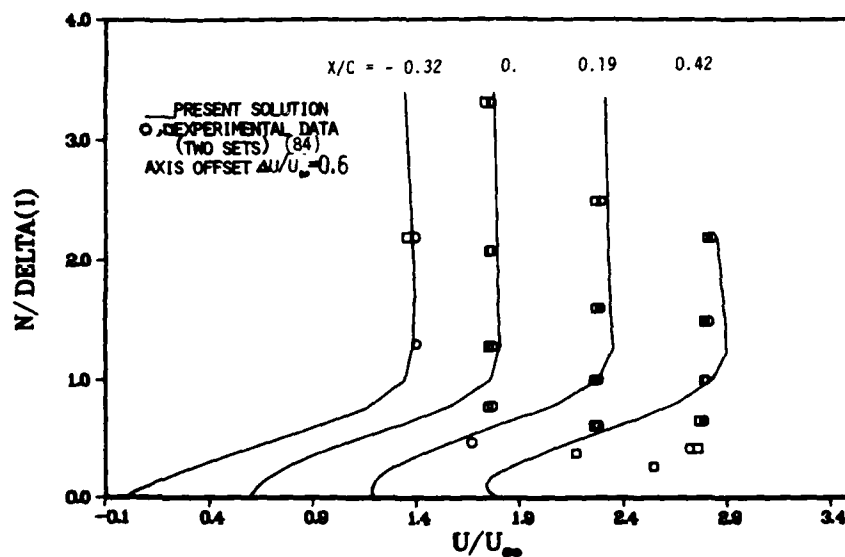
Figure 22.   Mean Flow Velocity Versus Surface Normal Distance
Nondimensionalized by Computed Boundary-Layer Thick-
ness at Chord Locations on Upper Surface (α = 9.5°)

Figure 23.   Mean Flow Velocity Versus Surface Normal Distance
Nondimensionalized by Computed Boundary-Layer Thick-
ness at Chord Locations on Upper Surface (α = 11.5°)
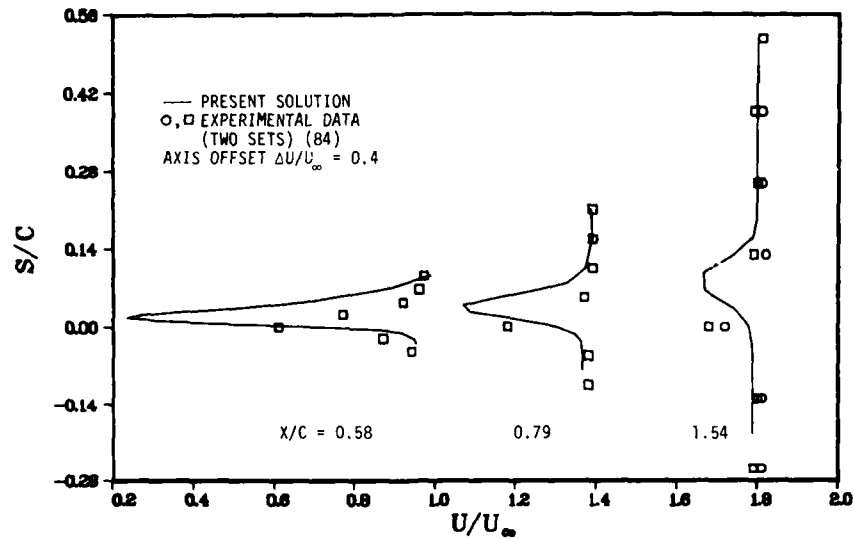
Figure 24. Wake Mean Flow Velocity Profiles at Chord Locations
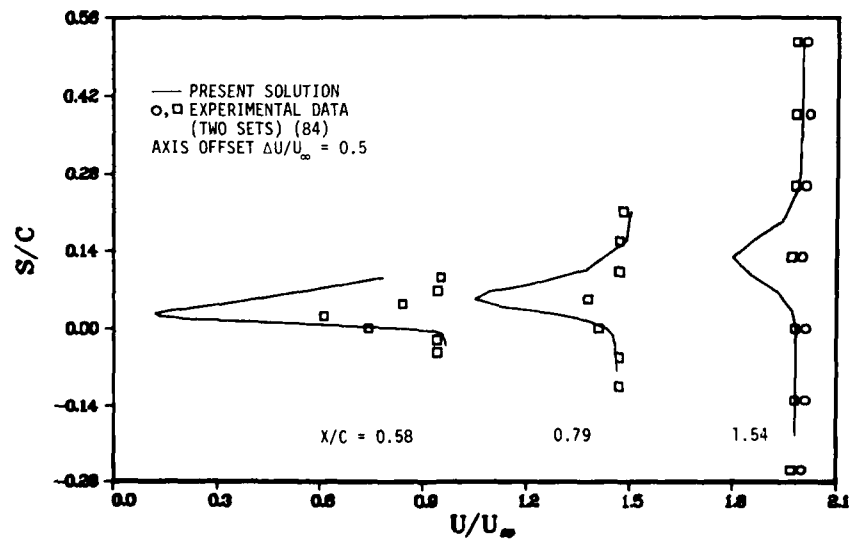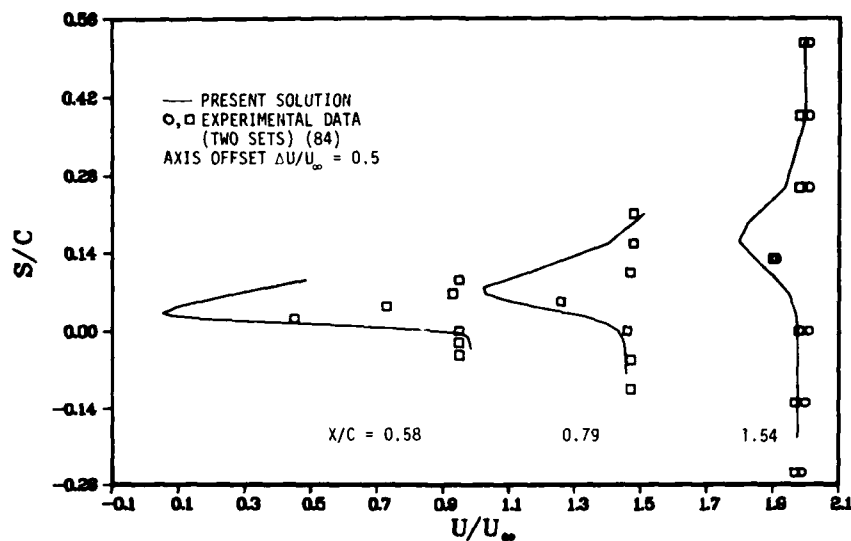with Origin on Chordline (α = 5°)

Figure 25. Wake Mean Flow Velocity Profiles at Chord Locations
with Origin on Chordline (α = 7.5°)

Figure 26. Wake Mean Flow Velocity Profiles at Chord Locations
with Origin on Chordline (α = 9.5°)
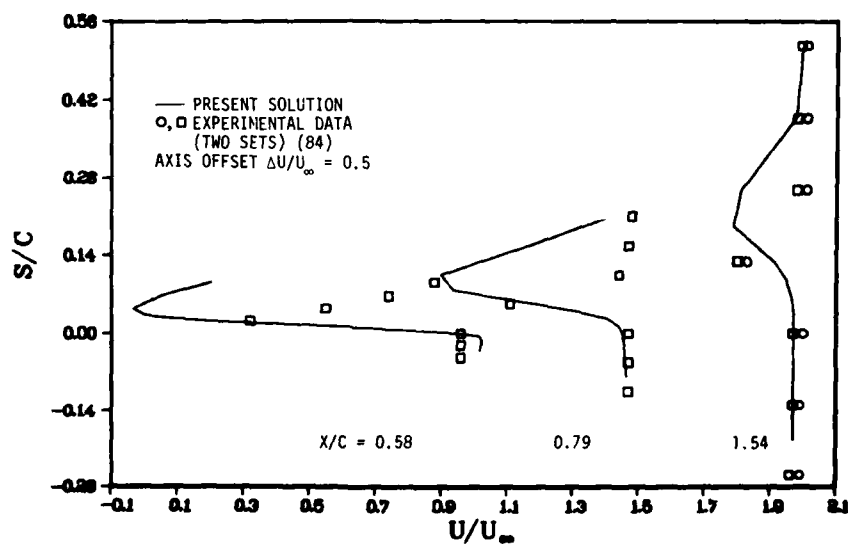

Figure 27. Wake Mean Flow Velocity Profiles at Chord Locations
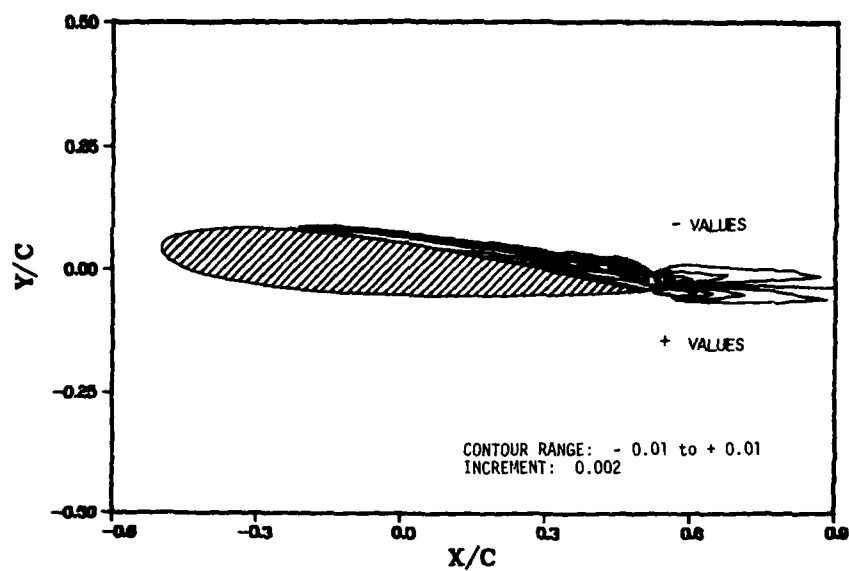with Origin on Chordline (α = 11.5°)

Figure 28.   Reynolds Stress $\overline{u'v'}$ Contours (α = 5°)
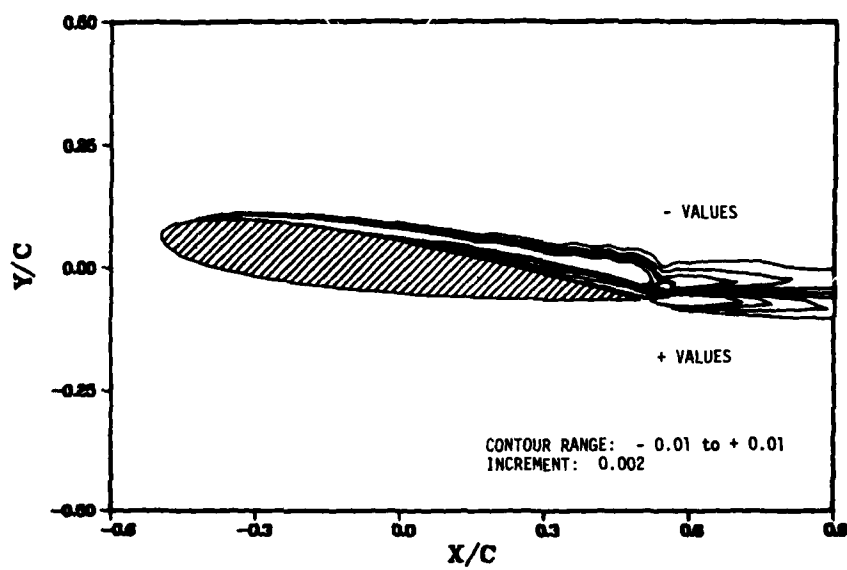

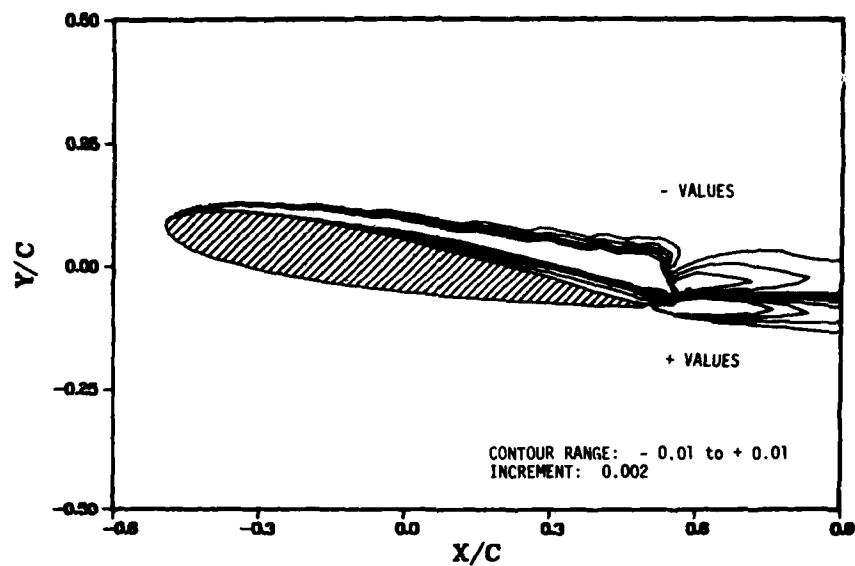Figure 29.   Reynolds Stress $\overline{u'v'}$ Contours (α = 7.5°)

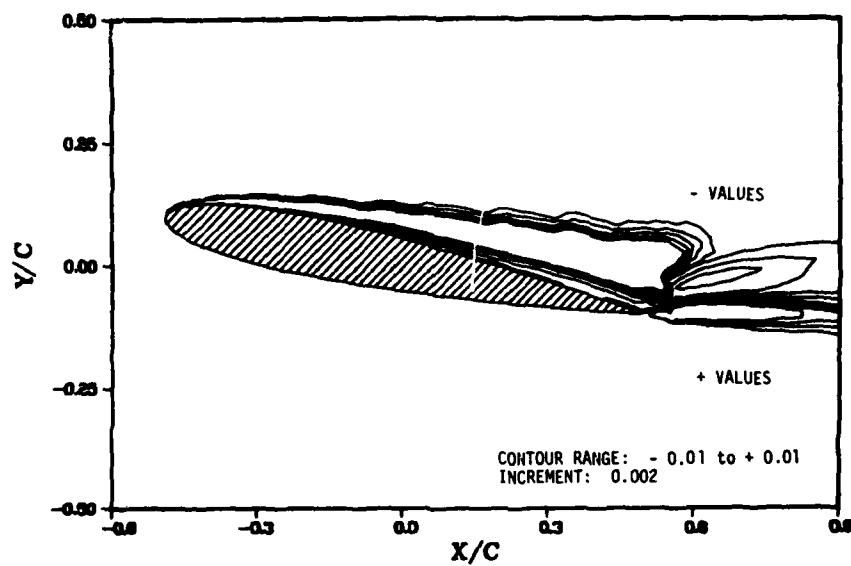Figure 30. Reynolds Stress $\overline{u'v'}$ Contours (α = 9.5°)

Figure 31. Reynolds Stress $\overline{u'v'}$ Contours (α = 11.5°)

Figure 11. Contour plots of double correlations $<u'u'>/(q_{ref})^2$, $<u'v'>/(q_{ref})^2$, and $<v'v'>/(q_{ref})^2$. Contour interval 0.010 or 0.005.

Figure 32. Experimental Reynolds Stress $\overline{u'v'}$ Contours for NACA 4412 Airfoil ($\alpha = 14°$ and Re = 1.5×10^6), Ref. 96
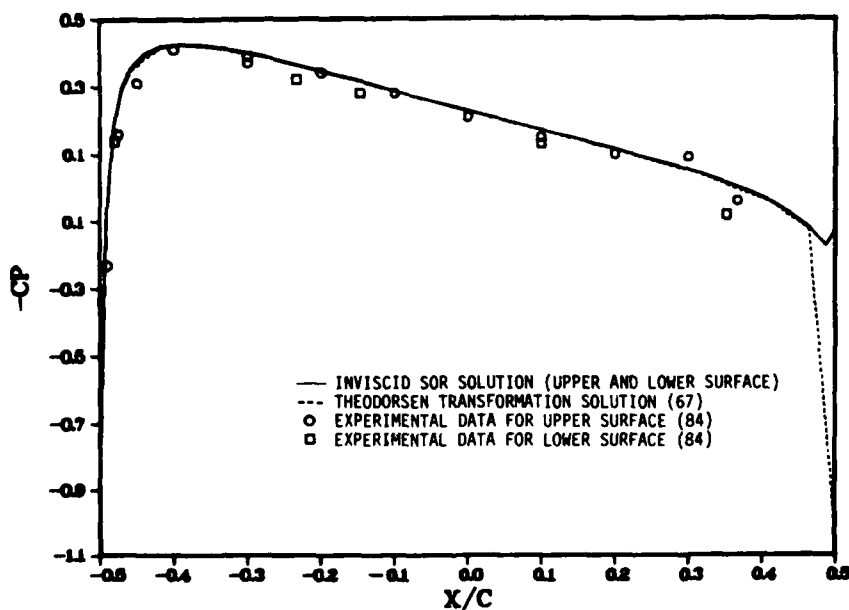
Figure 33. Surface Mean Pressure Coefficients Comparing Numerical Inviscid Methods with Experimental Data at $\alpha = 0°$
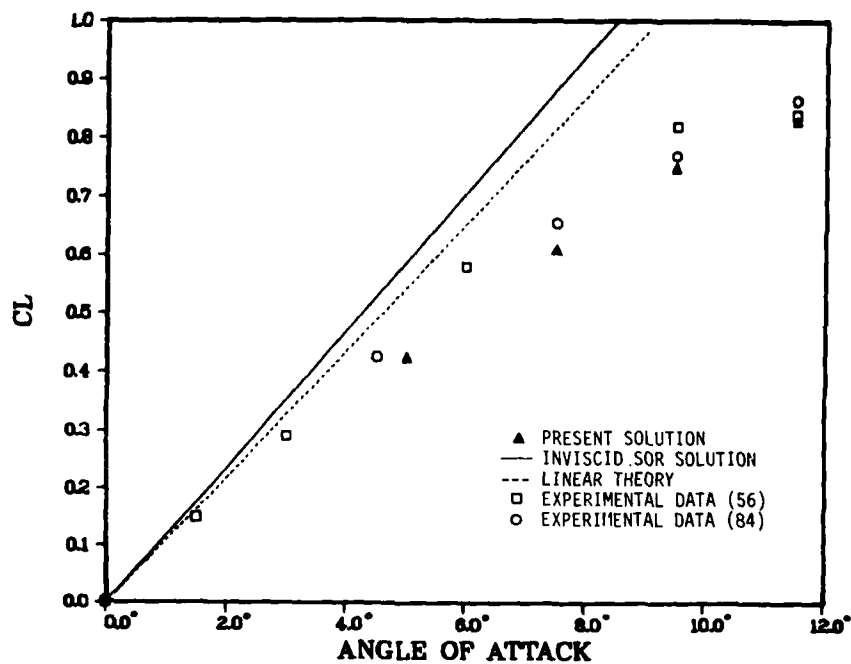
Figure 34.   Lift Coefficient Curve
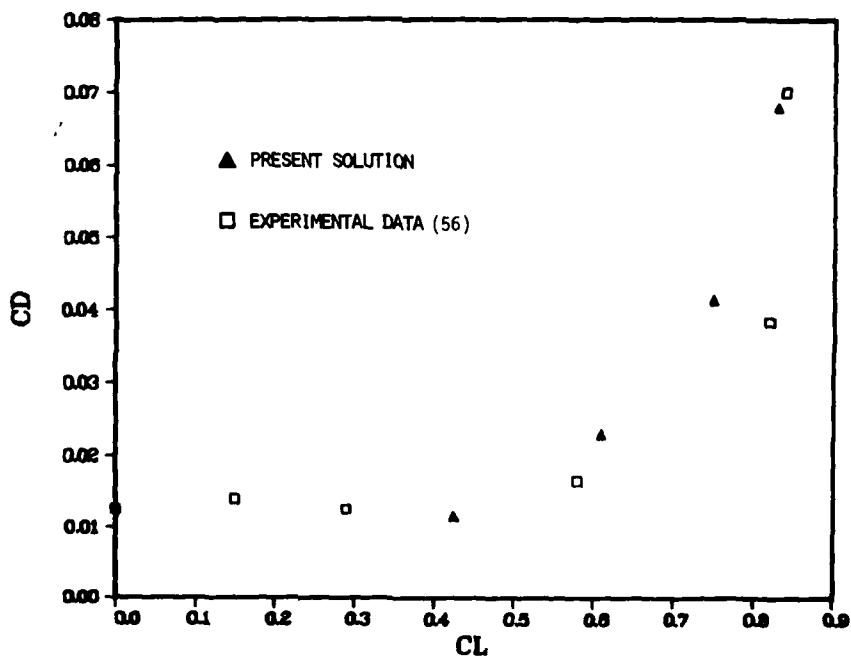
Figure 35.   Drag Polar Curve
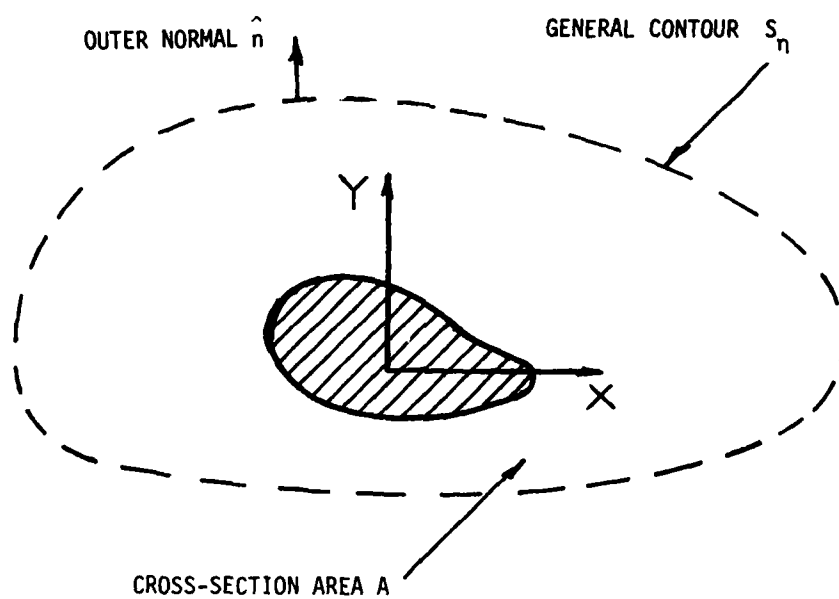
Figure 36. Contour Integration Geometry for
Two-Dimensional Flow
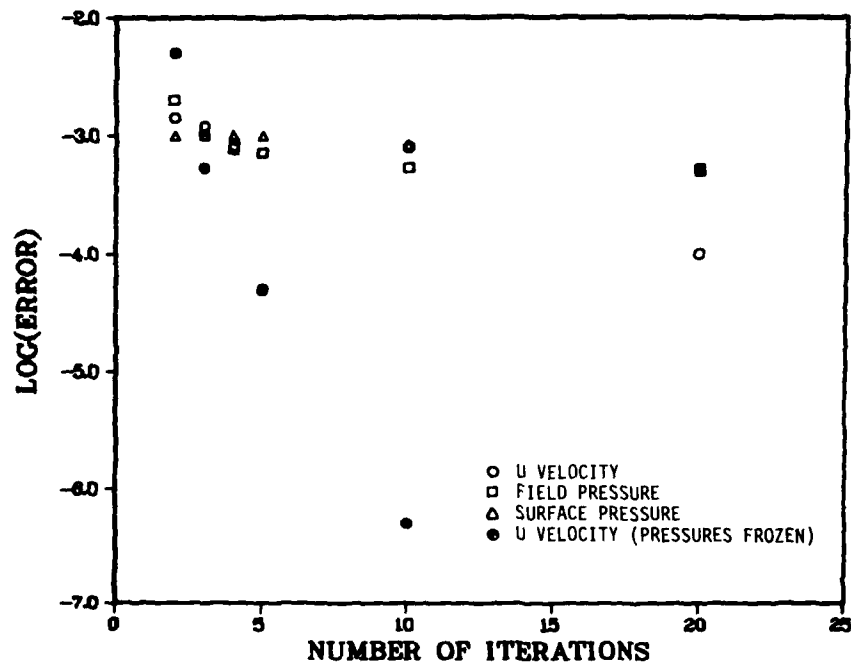
Figure 37. Maximum Error of SOR Solution for U, P, P_b Versus Number of Iterations with $\Delta t = 0.0005$ ($\alpha = 8°$)
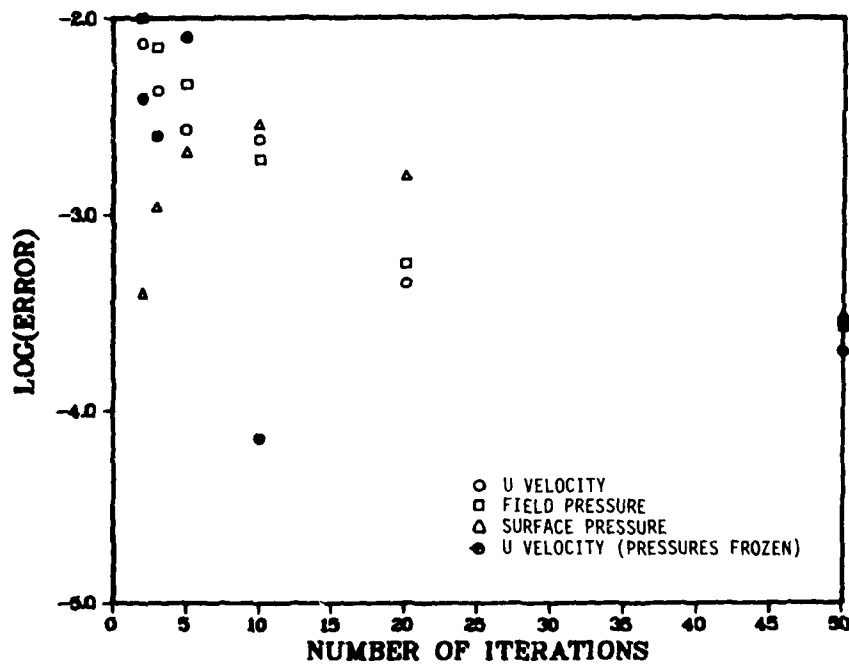
Figure 38. Maximum Error of SOR Solution for U, P, P_b Versus Number of Iterations with $\Delta t = 0.001$ ($\alpha = 8°$)

111
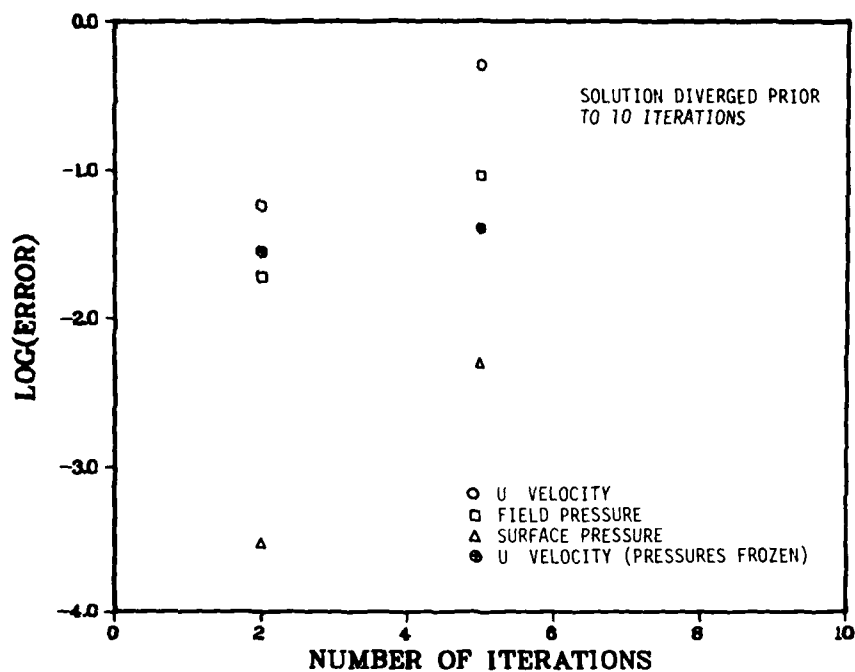
Figure 39.   Maximum Error of SOR Solution for U, P, P_b Versus
Number of Iterations with Δt = 0.005 (α = 8°)
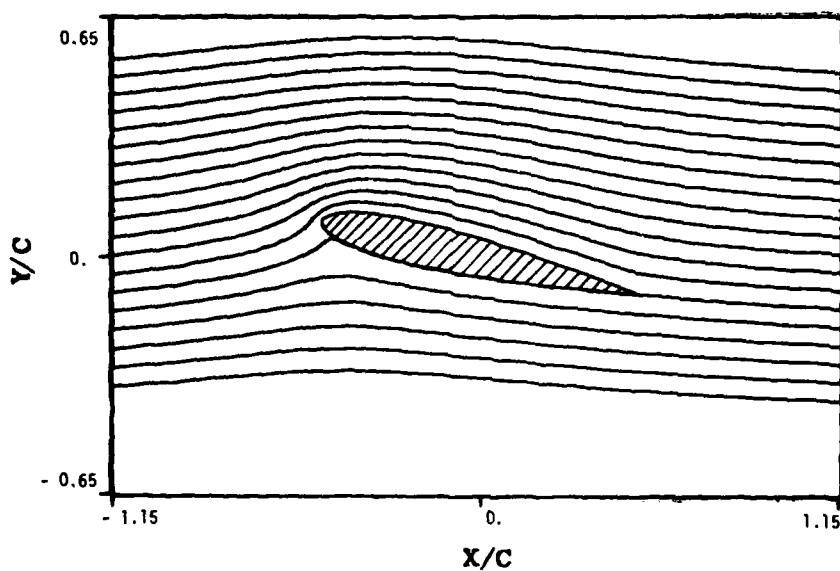
Figure 40.   Inviscid Flow Streamline Contours (α = 11.5°)

112

APPENDIX A

GRID TRANSFORMATION RELATIONSHIPS

Several of the definitions and coordinate transformation relations in the transformed plane are summarized below. The notation used by Thames (Reference 44) and Hodge (Reference 53) is retained. The physical plane is the (x, y) coordinate system and the computational plane is the (ξ, η) coordinate system. The following function definitions are used:

$f(x, y, t)$ - a twice differentiable scalar function.

$\underline{F}(x, y, t) = \hat{i} F_1(x, y, t) + \hat{j} F_2(x, y, t)$ a twice differentiable

vector function where $\hat{i}$ and $\hat{j}$ are Cartesian unit vectors.

Transformation Definitions

$$\alpha = x_\eta^2 + y_\eta^2 \tag{A-1}$$

$$\beta = x_\xi x_\eta + y_\xi y_\eta \tag{A-2}$$

$$\gamma = x_\xi^2 + y_\xi^2 \tag{A-3}$$

$$D_1 = (\alpha x_{\xi\xi} - 2\beta x_{\xi\eta} + \gamma x_{\eta\eta}) \tag{A-4}$$

$$D_2 = (\alpha y_{\xi\xi} - 2\beta y_{\xi\eta} + \gamma y_{\eta\eta}) \tag{A-5}$$

$$J = x_\xi y_\eta - x_\eta y_\xi \tag{A-6}$$

$$\sigma = (y_\xi D_1 - x_\xi D_2)/J \tag{A-7}$$

$$\tau = (x_\eta D_2 - y_\eta D_1)/J \tag{A-8}$$

Derivatives of Scalar Functions in Transformed Plane

$$f_x = \partial f/\partial x = (y_\eta f_\xi - y_\xi f_\eta)/J \tag{A-9}$$

$$f_y = \partial f/\partial y = (x_\xi f_\eta - x_\eta f_\xi)/J \tag{A-10}$$

$$f_t = \partial f/\partial t = (\partial f/\partial t)_{\xi,\eta} \text{ for fixed coordinates} \tag{A-11}$$

Vector Operators in the Transformed Plane

Gradient:

$$\underline{\nabla}f = \{(y_\eta f_\xi - y_\xi f_\eta)\,\hat{i} + (x_\xi f_\eta - x_\eta f_\xi)\,\hat{j}\}/J \tag{A-12}$$

Divergence:

$$\underline{\nabla} \cdot \underline{F} = \{y_\eta(F_1)_\xi - y_\xi(F_1)_\eta + x_\xi(F_2)_\eta - x_\eta(F_2)_\xi\}/J \tag{A-13}$$

Curl:

$$\underline{\nabla} \times \underline{F} = \hat{k}\{y_\eta(F_2)_\xi - y_\xi(F_2)_\eta - x_\xi(F_1)_\eta + x_\eta(F_1)_\xi\}/J \tag{A-14}$$

Laplacian:

$$\nabla^2 f = (\alpha f_{\xi\xi} - 2\beta f_{\xi\eta} + \gamma f_{\eta\eta})/J^2 + (\sigma/J^2)f_\eta + (\tau/J^2)f_\xi \tag{A-15}$$

Unit Normal and Tangent Vectors in Physical Plane

Normal to η line:

$$\underline{n}^{(\eta)} = \underline{\nabla}\eta/|\underline{\nabla}\eta| = (-y_\xi\hat{i} + x_\xi\hat{j})/\sqrt{\gamma} \tag{A-16}$$

Normal to ξ line:

$$\underline{n}^{(\xi)} = \underline{\nabla}\xi/|\underline{\nabla}\xi| = (y_\eta\hat{i} - x_\eta\hat{j})/\sqrt{\alpha} \tag{A-17}$$

Tangent to η line (increasing ξ direction):

$$\underline{t}^{(\eta)} = \underline{n}^{(\eta)} \times \hat{k} = (x_\xi\hat{i} + y_\xi\hat{j})/\sqrt{\gamma} \tag{A-18}$$

Tangent to ξ line (increasing η direction):

$$\underline{t}^{(\xi)} = -\underline{n}^{(\xi)} \times \hat{k} = (x_\eta\hat{i} + y_\eta\hat{j})/\sqrt{\alpha} \tag{A-19}$$

Integrals in the Transformed Plane

Area Integral:

$$\int_R f(x, y)\ dxdy = \int_{R^*} f(x(\xi, \eta), y(\xi, \eta))\ |J|\ d\xi d\eta \qquad \text{(A-20)}$$

where R^* is the region R mapped into the (ξ, η) plane.

Vector Line Integral:

$$\int_{s_\eta} \underline{F}(x, y)\ ds = \int_{\xi_{min}}^{\xi_{max}} \underline{F}(x(\xi, \eta_p), y(\xi, \eta_p))\sqrt{\gamma}\ d\xi \qquad \text{(A-21)}$$

where contour s_η is any constant η line in the physical plane, s is arclength along s_η, and η_p is the value of η for the chosen contour s_η.

APPENDIX B

FINITE DIFFERENCE APPROXIMATIONS

This appendix presents the finite difference approximations that are used in this investigation. The differences are formulated using a function $f(\xi, \eta)$ in the computational or transformed plane. The $\Delta\xi$ and $\Delta\eta$ spacings are assumed constant with value unity. The truncation error term is given in derivative form assuming $\Delta\xi$ and $\Delta\eta$ are equal. The approximations are second order accurate unless otherwise specified. Time differences are expressed by Δt. The superscript n denotes the nth time interval and is understood when omitted. The differences are given for a (ξ, η) point location denoted by subscripts (i, j) and are understood when omitted. Space derivatives with respect to only η are presented because the corresponding ξ derivatives are identical with subscripts (i, j) reversed.

First time derivative, backward difference, first order:

$$f_t = (f^n - f^{n-1})/\Delta t - \Delta t\, f_{tt}/2 + \ldots \tag{B-1}$$

First derivative, backward difference, first order:

$$f_\eta = (f_j - f_{j-1}) - f_{\eta\eta}/2 + \ldots \tag{B-2}$$

First derivative, central difference:

$$f_\eta = (f_{j+1} - f_{j-1})/2 - f_{\eta\eta\eta}/6 + \ldots \tag{B-3}$$

First derivative, forward difference:

$$f_\eta = (-f_{j+2} + 4f_{j+1} - 3f_j)/2 - f_{\eta\eta\eta}/3 + \ldots \tag{B-4}$$

First derivative, backward difference:

$$f_\eta = (f_{j-2} - 4f_{j-1} + 3f_j)/2 + f_{\eta\eta\eta}/3 + \ldots \tag{B-5}$$

Second derivative, central difference:

$$f_{\eta\eta} = (f_{j+1} - 2f_j + f_{j-1}) - f_{\eta\eta\eta\eta}/12 + \ldots \tag{B-6}$$

Second derivative, forward difference:

$$f_{\eta\eta} = (-f_{j+3} + 4f_{j+2} - 5f_{j+1} + 2f_j) + 11f_{\eta\eta\eta\eta}/12 + \ldots \tag{B-7}$$

Second derivative, backward difference:

$$f_{\eta\eta} = (f_{j-3} - 4f_{j-2} + 5f_{j-1} - 2f_j) - 11f_{\eta\eta\eta\eta}/12 + \ldots \tag{B-8}$$

Cross derivative, central difference:

$$f_{\xi\eta} = (f_{i+1,\,j+1} - f_{i+1,\,j-1} + f_{i-1,\,j-1} - f_{i-1,\,j+1})/4$$

$$- (f_{\xi\xi\xi\eta} + f_{\xi\eta\eta\eta})/24 + \ldots \tag{B-9}$$

Cross derivative, central in ξ and forward in η differences:

$$f_{\xi\eta} = \{-3(f_{i+1} - f_{i-1}) + 4(f_{i+1,\,j+1} - f_{i-1,\,j+1})$$

$$- (f_{i+1,\,j+2} - f_{i-1,\,j+2})\}/4 + (f_{\xi\xi\xi\eta} + f_{\xi\eta\eta\eta})/6 + \ldots \tag{B-10}$$

Cross derivative, central in ξ and backward in η differences:

$$f_{\xi\eta} = \{3(f_{i+1} - f_{i-1}) - 4(f_{i+1,\,j-1} - f_{i-1,\,j-1})$$

$$+ (f_{i+1,\,j-2} - f_{i-1,\,j-2})\}/4 - (f_{\xi\xi\xi\eta} + f_{\xi\eta\eta\eta})/6 + \ldots$$

$$\tag{B-11}$$

APPENDIX C

GRID MODIFICATION FOR WAKE RESOLUTION

This appendix describes the technique that is used to insert additional grid lines in the region of the airfoil wake. The body-fitted coordinate grid system becomes coarse at distances far from the body. The coarse grid may reduce the resolution of the velocity defect in the viscous far wake region. To increase wake resolution, eight additional ξ lines are placed downstream of the airfoil with body points on the rounded trailing edge. The original numerically generated grid has 71 ξ and 44 η lines. Linear interpolation between adjoining ξ lines of the form $x_p(I,J) = \{x(I-1, J) + x(I, J)\}/2$ is used to locate a ξ line between lines $I = 1$ and $I = 2$, $I = 2$ and $I = 3$, $I = 69$ and $I = 70$, and $I = 70$ and $I = 71$. The procedure is repeated using the new lines as well except only one additional line is located below the $I = 1$ cut. In this way the fine grid spacing has an asymmetry for better wake resolution at angle of attack. The final 79 by 44 grid is shown in Figure 3. Table C-1 gives the numbered I index (ξ line) designation for the grid systems in the wake region.

Table C-1

I INDEX (ξ LINE) DESIGNATION FOR GRID SYSTEMS IN WAKE

71 x 44 System	75 x 44 System	79 x 44 System
69	71	72
-	72	73
-	-	74
70	73	75
-	-	76
-	74	77
-	-	78
71, 1	75, 1	79, 1
-	-	2
-	2	3
2	3	4
-	4	5
3	5	6

APPENDIX D

CONTOUR INTEGRAL METHOD FOR DETERMINING BODY FORCE COEFFICIENTS

The determination of the resultant force that a flow field exerts on a body usually involves the calculation of surface pressure and viscous stresses and the summation of these forces over the body surface. An alternate approach is to apply a control volume analysis to a region enclosing the body. In the foregoing discussion, a control volume analysis for a body in a two-dimensional flow is presented.

Consider a general body immersed in a flow field with surface σ_B. Define a fixed control volume V with outer surface σ_η and inner surface σ_B. Conservation of linear momentum for the fluid in V is expressed by the Cauchy Integral Equation of Motion

$$\frac{D}{Dt} \int_V \rho \underline{v} \, dV = \int_V \rho \underline{b} \, dV + \int_\sigma \hat{n} \cdot \overline{\overline{T}} \, d\sigma \qquad (D-1)$$

where ρ is the density, $\underline{v}$ velocity field, $\underline{b}$ body force per unit mass, $\hat{n}$ unit outward surface normal vector, $\overline{\overline{T}}$ traction stress, and σ is the total surface $\sigma_B + \sigma_\eta$. Apply the Reynolds Transport Theorem to the material derivative term and the Divergence Theorem to the surface integral and obtain from Equation D-1 for the ith Cartesian vector component

$$\int_V \frac{\partial}{\partial t} (\rho v_i) \, dV + \int_V \partial_j (\rho v_i \, v_j - T_{ji}) \, dV = 0 \qquad (D-2)$$

Apply the Divergence Theorem to the second volume integral and express the resulting surface integral as separate integrals over σ_B and σ_η to obtain

$$\int_V \frac{\partial}{\partial t} (\rho v_i) \, dV + \int_{\sigma_B} n_j(\rho v_i v_j - T_{ji}) \, d\sigma + \int_{\sigma_\eta} n_j(\rho v_i v_j - T_{ji}) d\sigma$$

$$= 0 \qquad\qquad\qquad (D-3)$$

Now, on the solid nonporous body surface σ_B, $n_j v_j = 0$. The integral of the resultant traction force over σ_B is the net force exerted by the body on the control volume fluid. Therefore, the force $\underline{F}$ exerted by the fluid on the body is given by

$$F_i = - \int_{\sigma_B} n_j T_{ji} \, d\sigma \qquad\qquad (D-4)$$

Substitute Equation D-4 into D-3 and use the above surface condition to obtain a general expression for the force exerted by the fluid on the body.

$$F_i = - \frac{\partial}{\partial t} \int_V \rho v_i \, dV + \int_{\sigma_\eta} n_j(T_{ji} - \rho v_i v_j) \, d\sigma \qquad (D-5)$$

Now consider the case of two-dimensional flow in the x-y plane. Then Equation D-5 becomes the following expression for the force per length of span $\underline{f}$

$$f_i = - \frac{\partial}{\partial t} \int_A \rho v_i \, dA + \int_{s_\eta} n_j(T_{ji} - \rho v_i v_j) \, ds \qquad (D-6)$$

where A is the cross-sectional area of the control volume and s_η is the outer perimeter of A as shown in Figure 36.

Substitute for the traction stress $T_{ji} = -p\delta_{ji} + \tau_{ji}$ in Equation D-6 and obtain

$$f_i = \int_{s_\eta} n_j(-p\delta_{ji} + \tau_{ji} - \rho v_i v_j) ds - \frac{\partial}{\partial t} \int_A \rho v_i \, dA \quad (D-7)$$

where p is the pressure, τ_{ji} is the laminar viscous stress and δ_{ji} is the Kronecker Delta function. Next express the flow variables in terms of turbulent mean and fluctuating variables, assume incompressible flow, and Reynolds average Equation D-7 to obtain

$$\bar{f}_i = \int_{S_\eta} n_j\{-\bar{p}\delta_{ji} + \bar{\tau}_{ji} - \rho(\bar{v}_i\bar{v}_j + \overline{v_i'v_j'})\} \, ds$$

$$- \frac{\partial}{\partial t} \int_A \rho\bar{v}_i \, dA \qquad\qquad (D-8)$$

The term $\overline{-\rho v_i'v_j'}$ is the turbulent Reynolds stress $\bar{\tau}_{tji}$. Let the total stress be defined as $\bar{\tau}_{Tji} = \bar{\tau}_{ji} + \bar{\tau}_{tji}$. Then Equation D-8 becomes

$$\bar{f}_i = \int_{S_\eta} n_j \{-\bar{p}\delta_{ji} + \bar{\tau}_{Tji} - \rho\bar{v}_i\bar{v}_j\} \, ds - \frac{\partial}{\partial t} \int_A \rho\bar{v}_i dA \qquad (D-9)$$

Introduce the following nondimensional variables in Equation D-9

$$\tilde{p} = \frac{\bar{p} - p_\infty}{\rho U_\infty^2} \qquad \tilde{v}_i = \frac{\bar{v}_i}{U_\infty} \qquad \tilde{x}_i = \frac{x_i}{L} \quad \text{and } \tilde{t} = \frac{tU_\infty}{L} \text{ , and note that}$$

$$\tilde{\tau}_{Tji} = \frac{L}{U_\infty} \bar{\tau}_{Tji} \text{ where } U_\infty \text{ is the freestream velocity and L is a reference}$$

length in the x direction. Also, define the force coefficient $C_{f_i} = \dfrac{f_i \cdot 2}{\rho U^2 L}$ and obtain from Equation D-9

$$C_{f_i} = 2 \int_{S_\eta} n_j\{-p\delta_{ji} + \frac{1}{\rho U_\infty L}\tau_{Tji} - v_iv_j\} \, ds - 2\frac{\partial}{\partial t}\int_A v_i dA \quad (D-10)$$

where all variables are understood to be mean dimensionless variables. Now the turbulent eddy viscosity concept is used where

$$\tau_{Tji} = (\mu + \epsilon_M) \cdot (\partial_i v_j + \partial_j v_i)$$

and define $Re_t = \dfrac{\rho U_\infty L}{\mu + \epsilon_M}$ which transforms Equation D-10 to the following

$$C_{f_i} = 2 \int_{s_\eta} n_j \{-p\delta_{ji} + \frac{1}{Re_t} (\partial_i v_j + \partial_j v_i) - v_i v_j\} \, ds - 2 \frac{\partial}{\partial t} \int_A v_i dA$$

(D-11)

Expand Equation D-11 into x and y component equations

$$C_{f_x} = 2 \int_{s_\eta} \{-n_1 p + \frac{1}{Re_t} [2n_1\frac{\partial u}{\partial x} + n_2 (\frac{\partial u}{\partial y} + \frac{\partial v}{\partial x})] - (u^2 n_1 + uvn_2)\} \, ds$$

$$- 2 \frac{\partial}{\partial t} \int_A u dA$$

(D-12a)

$$C_{f_y} = 2 \int_{s_\eta} \{-n_2 p + \frac{1}{Re_t} [n_1 (\frac{\partial u}{\partial y} + \frac{\partial v}{\partial x}) + 2n_2 \frac{\partial v}{\partial y}] - (uvn_1 + v^2 n_2)\} \, ds$$

$$- 2 \frac{\partial}{\partial t} \int_A v dA$$

(D-12b)

where n_1 and n_2 are the x and y components of the unit outward normal vector $\hat{n}$ for the outer boundary s_η of area A. Equations (D-12a) and (D-12b) are expressions for the x and y force coefficients exerted by a two-dimensional incompressible turbulent flow on an arbitrary two-dimensional body where path s_η encloses the body and an eddy viscosity method is used to model turbulence.

Lift and drag coefficients are then obtained from the force coefficients as follows where α is the geometric angle of attack.

$$C_L = C_{f_y} \cos \alpha - C_{f_x} \sin \alpha$$

(D-13)

$$C_D = C_{f_y} \sin \alpha + C_{f_x} \cos \alpha$$

(D-14)

APPENDIX E

TIME INCREMENT INFLUENCE ON SOR CONVERGENCE

Implicit SOR methods have been shown by linear stability analyses to be unconditionally stable. However, convergence has required a small time step size in this investigation and elsewhere. The following analysis indicates the relationship between the time step size and convergence.

Consider the system of difference equations to be written in the following matrix form:

$$AU = b \tag{E-1}$$

where A is the coefficient matrix, U is the vector of unknown primitive variables at time step n with u, v, p grouped together for each (i,j) point location, and b is a vector of "constants". For example, the x component of the momentum equation (Equation 92) at the (i,j) point is

$$Q\, u_{ij}^{(s)} = u_{ij}^{n-1} + \Delta t[-YETA\, (p_{i+1\ j} - p_{i-1\ j}) + YXI\, (p_{i\ j+1} - p_{i\ j-1})$$

$$+ |UC|\, (4u_{IC1\ j} - u_{IC2\ j}) + |VC|\, (4u_{i\ JC1} - u_{i\ JC2}) + |UV|\, (4u_{IV1\ j} -$$

$$u_{IV2\ j}) + |VV|\, (4u_{i\ JV1} - u_{i\ JV2}) + \frac{1}{RET}\, \{ALFA\, (u_{i+1\ j} + u_{i-1\ j})$$

$$+ GAMA\, (u_{i\ j+1} + u_{i\ j-1}) + BETA\, (u_{i+1\ j+1} - u_{i+1\ j-1} + u_{i-1\ j-1} -$$

$$u_{i-1\ j+1})\} - u_{ij}^{(s-1)}\quad D] \tag{E-2}$$

where all coefficients are evaluated at point (i,j) and primitive variables are at time step n unless given otherwise, and Q is given by

$$Q = 1 + 3\, \Delta t(|UC| + |VC| + |UV| + |VV|) + \frac{2}{Re_t}\, (|ALFA| + |GAMA|)$$

Rearrange Equation E-2 and obtain

$$- |UC| \, u_{IC2 \, j} - |UV| \, u_{IV2 \, j} + \frac{BETA}{RET} u_{i-1 \, j-1} + 4 \, |UC| \, u_{ic1 \, j} + 4 \, |UV| \, u_{IV1 \, j}$$

$$+ \frac{ALFA}{RET} u_{i-1 \, j} + YETA \, p_{i-1 \, j} - \frac{BETA}{RET} u_{i-1 \, j+1} - |VC| \, u_{i \, JC2} - |VV| \, u_{i \, JV2}$$

$$+ \frac{GAMA}{RET} u_{i \, j-1} + 4 \, |VC| \, u_{i \, JC1} + 4 |VV| \, u_{i \, JV1} - YXI \, p_{i \, j-1} - \frac{Q}{\Delta t} u_{ij}^{(s)}$$

$$+ \frac{GAMA}{RET} u_{i \, j+1} + YXI \, p_{i \, j+1} - \frac{BETA}{RET} u_{i+1 \, j-1} + \frac{ALFA}{RET} u_{i+1 \, j} - YETA \, p_{i+1 \, j}$$

$$+ \frac{BETA}{RET} u_{i+1 \, j+1} = - \frac{u_{ij}^{n-1}}{\Delta t} + u_{ij}^{(s-1)} \quad D \qquad (E-3)$$

A similar y component of momentum equation is obtained if u is replaced by v; - YETA by XETA; and YXI by - XXI.

The finite difference pressure Equation 94 becomes

$$- |UV| \, p_{IV2 \, j} + BETA \, p_{i-1 \, j-1} + 4|UV| \, p_{IV1 \, j} + ALFA \, p_{i-1 \, j}$$

$$- BETA \, p_{i-1 \, j+1} - |VV| \, p_{i \, JV2} + GAMA \, p_{i \, j-1} + 4|VV| \, p_{i \, JV1} - Bp_{ij}$$

$$+ GAMA \, p_{i \, j+1} - BETA \, p_{i+1 \, j-1} + ALFA \, p_{i+1 \, j} + BETA \, p_{i+1 \, j+1} = -RHS$$

$$(E-4)$$

where $B = 2 \, (ALFA + GAMA) + 3 \, (|UV| + |VV|)$ and $RHS = - \frac{D^{n-1}}{\Delta t} + [(UX)^2 + 2(VX)(UY) + (VY)^2]$

Convergence theorems (Reference 81) for systems of linear equations with constant coefficients show that a necessary and sufficient condition for convergence requires that the coefficient matrix be diagonally dominant.

If this criteria is applied to the above quasi-linear system, the
following convergence criteria, inequality E-6 from the momentum
equation and inequality E-8 from the pressure equation, are obtained.

$$5 \, (|UC| + |VC| + |UV| + |VV|) + \frac{2}{RET} \, (|ALFA| + |GAMA|)$$

$$+ \frac{3}{RET} \, |BETA| + 2(|YXI| + |YETA|) < \frac{Q}{\Delta t}$$

$$or < 3 \, (|UC| + |VC| + |UV| + |VV|) + \frac{2}{RET} \, (|ALFA| + |GAMA|) + \frac{1}{\Delta t} \qquad (E-5)$$

which becomes

$$\Delta t < \{2 \, (|UC| + |VC| + |UV| + |VV|) + \frac{3}{RET} |BETA| + 2(|YXI| + |YETA|)\}^{-1} \qquad (E-6)$$

and

$$2(|ALFA| + |GAMA|) + 4 \, |BETA| + 5 \, (|UV| + |VV|) <$$

$$2(|ALFA| + |GAMA|) + 3 \, (|UV| + |VV|) \qquad (E-7)$$

or

$$4 \, |BETA| + 2 \, (|UV| + |VV|) \quad < 0 \qquad (E-8)$$

The convergence criteria (Equation E-6) provides a limit on Δt as a
function of both the grid geometry and flow field solution. The right-hand
side of the inequality has its smallest magnitude near the trailing edge
and increases rapidly away from the airfoil. An order of magnitude analysis
of the grid coefficients and an examination of the computational solutions
indicate that diagonal dominance occurs if $\Delta t < 0.0003$ for points near the
trailing edge, $\Delta t < 0.001$ elsewhere near the body, and $\Delta t < 1$ in the far
field. The pressure equation convergence criteria, (Equation E-8) has no
Δt dependence and is approximately satisfied only at points far from the
body where the left-hand side approaches zero. These criteria can only
indicate a possible time step restriction since the system of equations
has variable coefficients and lower order nonlinearities.

A numerical experiment was conducted to determine the time step effect on convergence. A computation for the flow over the NACA 0012 airfoil at an angle of attack of eight degrees was used. The solution was advanced one time step with the time step size and number of iterations per time step varied. The solution converged for time steps of 0.0005 and 0.001 while diverging for a time step of C.005. The relative maximum error magnitudes for the u component of velocity, surface pressure p_b, and field pressure p as functions of number of iterations are shown for each time step in Figures 37, 38, and 39. The relative error is defined as $(f_n - f_{n-1})/f_n$. The v component of velocity errors behave similarly to the u component. Next, the pressure was held fixed and the convergence of the velocity was monitored (Figures 37, 38, and 39). The rapid rate of convergence is observed. The u and v velocity components were also held fixed in turn to test convergence. In both cases, convergence was similar to the general solution case. These numerical experiments indicate that the convergence of pressure is slow and that convergence is dependent on time step sizes similar to those predicted by the simple analysis above.

APPENDIX F

FAR FIELD BOUNDARY CONDITIONS

The far field boundary for a numerical solution must usually be at a finite distance from the body of interest. This constraint may pose difficulties if the only known far field boundary conditions are those at infinity. This analysis uses complex variable methods for incompressible potential flow and develops approximate far field boundary conditions for use at a finite distance.

Consider a circular cylinder radius a and center at the origin, with positive clockwise circulation Γ, in a uniform stream (velocity U_∞), at angle of attack α. This coordinate system is identical with the physical plane of the airfoil. The complex velocity is

$$\tilde{W}(\tilde{z}) = U_\infty e^{-i\alpha} - \frac{(2\pi a^2 U_\infty)}{2\pi} \frac{e^{i\alpha}}{\tilde{z}^2} + i \frac{\Gamma}{2\pi} \frac{1}{\tilde{z}} \qquad (F-1)$$

where the first term is the uniform stream contribution, the second term is a doublet of strength $2\pi a^2 U_\infty$, and the third term is a vortex of strength Γ.

Next, use the Kutta-Joukowski Theorem for lift and the definition of the lift coefficient to obtain

$$\Gamma = (1/2) C_L U_\infty c \qquad (F-2)$$

where c is the airfoil chord.

Nondimensionalize Equation F-1 velocities with the freestream velocity U_∞ and lengths with the airfoil chord c and substitute Equation F-2 into F-1 and obtain

$$W(Z) = e^{-i\alpha} - \left(\frac{a}{c}\right)^2 \frac{e^{i\alpha}}{Z^2} + i \frac{C_L}{4\pi} \frac{1}{Z} \qquad (F-3)$$

where W is the nondimensional complex velocity and Z is the nondimensional complex variable $Z = x + iy$.

Airfoil transformations such as the Joukowski and Treffetz Transformations transform a cylinder into an airfoil with a chord of four radii. Thus, for a given chord c, choose the cylinder radius to be 1/4 c which gives a scaling factor $\frac{a}{c} = 1/4$ in the doublet. Then the complex velocity for the flow around the scaled cylinder becomes

$$W(Z) = e^{-i\alpha} - \frac{e^{i\alpha}}{16Z^2} + i \frac{C_L}{4\pi} \frac{1}{Z} \qquad (F-4)$$

Expression F-4 can then be used to approximate the far field potential flow over the airfoil of chord c with circulation Γ in the same physical plane.

Let the far field boundary be a circle of radius r_f where $Z = r_f e^{i\Theta}$, $0 \le \Theta < 2\pi$. Substitute for Z in Equation F-4 and obtain

$$W_f(\Theta) = e^{-i\alpha} - \frac{e^{i\alpha}}{16r_f^2} e^{-2i\Theta} + i \frac{C_L}{4\pi} \frac{1}{r_f} e^{-i\Theta} \qquad (F-5)$$

Combine the exponential terms in F-5 and use the fact that $W = u - iv$, where u and v are the x and y velocity components, to obtain

$$u_f(\Theta) = \cos\alpha - \frac{1}{16r_f^2} \cos(\alpha - 2\Theta) + \frac{C_L}{4\pi r_f} \sin\Theta \qquad (F-6a)$$

$$v_f(\Theta) = \sin\alpha + \frac{1}{16r_f^2} \sin(\alpha - 2\Theta) - \frac{C_L}{4\pi r_f} \cos\Theta \qquad (F-6b)$$

In both Equations F-6, the first term is the freestream velocity contribution, the second term is the doublet contribution, and the third term is the vortex contribution. As r_f approaches infinity, the infinity freestream

boundary conditions for u and v are recovered. Also, the doublet term is of higher order in $1/r_f$ than the vortex term for the case of a lifting airfoil and may be neglected.

The far field pressure is obtained by applying Bernoulli's equation for irrotational incompressible flow and using the nondimensional form for pressure. The result for the far field boundary is

$$p_f (\theta) = 1/2 \{1-(u_f{}^2 + v_f{}^2)\} \qquad (F-7)$$

The far field boundary conditions of Equations F-6 and F-7 modify the infinity freestream conditions by incorporating effects on the flow of body thickness and circulation at a large but finite distance from the airfoil.

Transonic small disturbance theory for slender bodies and airfoils has similar expressions for the far field conditions. Klunker (Reference 101) has obtained an asymptotic solution applicable at large distances from thin airfoils. This form has been used as a numerical outer boundary condition. For the limiting case of incompressible two-dimensional flow, the doublet and vortex strengths are compared below with the general forms found in Equation F-1.

The nondimensional velocity potential doublet in the far field from Klunker becomes

$$\phi_d = \frac{1}{2\pi} \frac{x}{x^2+y^2} 2\int_0^c F(s)ds \qquad (F-8)$$

where F(s) is the airfoil thickness function. The doublet strength is thus $2\int F(s)ds$. The NACA four digit airfoil thickness function (Reference 67) is

$$F(s) = \frac{cf}{0.2} \left(.2969 \left(\frac{s}{c}\right)^{\frac{1}{2}} - .126 \frac{s}{c} - .3516\left(\frac{s}{c}\right)^2 + .2843 \left(\frac{s}{c}\right)^3 - .1015 \left(\frac{s}{c}\right)^4\right)$$

$$(F-9)$$

where c is the airfoil chord, f is the maximum thickness as a fraction of chord and s is the chord distance, $0 \le s \le c$.

Substitute the thickness function Equation F-9 into the doublet strength expression and obtain the following doublet strength from transonic small disturbance theory:

$$\mu_D = 0.685 \ fc^2 \qquad (F-10)$$

For the case of a NACA 0012 airfoil, $\mu_D = 0.0822c^2$. The corresponding doublet strength in the simple potential flow model from Equation F-1 is $2\pi \ (\frac{c}{4})^2$ or $.3972c^2$. Klunker points out that the doublet may be neglected in the far field for finite circulation flows because the vortex contribution is of order $(\frac{1}{r_f})$ compared with an order $(\frac{1}{r_f})^2$ for the doublet.

The vortex potential term of Klunker for the case of incompressible two-dimensional flow is

$$\phi_V = \frac{\Gamma}{2\pi} \ \{\frac{\pi}{2} \ sgn \ (y) + tan^{-1}(\frac{x}{y})\} \qquad (F-11)$$

where Γ is the clockwise circulation, the inverse tangent function is defined on the interval $(-\frac{\pi}{2}, \frac{\pi}{2})$, and the angle within braces is defined clockwise from the negative x axis. This potential function is identical with the vortex function in Equation F-1 where the clockwise strength is again Γ and the angular orientation is the right hand polar coordinate Θ defined counterclockwise from the positive x axis.

Thus the far field potential for each method differs only in the thickness or doublet term. Furthermore, for flows with finite circulation this difference is negligible because the vortex term dominates.

APPENDIX G

NUMERICAL INVISCID FLOW RESULTS

A numerical solution for the inviscid flow over the NACA 0012 airfoil is obtained for comparison with both the Navier-Stokes computation and the experimental data. The numerical algorithm, developed by Thames (Reference 44), which solves Laplace's equation for the stream function in two-dimensional flow is used. The method uses SOR iteration to solve the system of equations written in terms of body-fitted coordinates. The stream function value on the body can either be specified or computed by imposing a given circulation or a Kutta condition.

The stream function equation for two-dimensional flow is

$$\psi_{xx} + \psi_{yy} = 0 \tag{G-1}$$

Rewrite Equation G-1 in terms of the transformed variables in the computational plane using expressions in Appendix A to obtain

$$\alpha\, \psi_{\xi\xi} - 2\beta\psi_{\xi\eta} + \gamma\psi_{\eta\eta} + \sigma\psi_{\eta} + \tau\, \psi_{\xi} = 0 \tag{G-2}$$

The boundary condition for the stream function on the outer boundary, which is a radius of ten chords, is the freestream value

$$\psi_f = y_f\, \cos \alpha_L - x_f\, \sin \alpha_L \tag{G-3a}$$

where (x_f, y_f) are coordinates on the outer computational boundary and α_L is the angle of attack. Hodge and Ghia (Reference 82) have shown by an inviscid analysis that this boundary condition induces an error in lift of less than 1% for angles of attack less than 10°. The boundary condition on the body is

$$\psi_b = \text{constant} \tag{G-3b}$$

The constant can be specified or determined by imposing a given circulation or a Kutta condition. The Kutta condition which matches the upper

132

and lower trailing edge surface velocities by extrapolation is selected. The details for each option are given by Thames (Reference 44).

The derivatives in the transformed Equation G-2 are approximated by central difference formulas found in Appendix B. The resulting system of equations is solved by SOR as described by Thames (Reference 44). Solutions are obtained for $0°$, $5°$, $7.5°$, $9.5°$, and $11.5°$ for the NACA 0012 airfoil section. The body surface pressure coefficients can be calculated from the stream function solution as follows. The body pressure coefficient is defined as

$$C_p = 1 - (u^2 + v^2) \tag{G-4}$$

where at a location on the body u and v are the x and y components of the flow velocity nondimensionalized by the freestream velocity. Use the definition of the stream function to obtain

$$C_p = 1 - \{(\psi_y)^2 + (\psi_x)^2\} \tag{G-5}$$

Then rewrite the Equation G-5 in terms of the transformed variables and note that $\psi_\xi = 0$ on the body to give

$$C_p = 1 - \frac{\alpha}{J^2} (\psi_\eta)^2 \tag{G-6}$$

where all quantities are evaluated on the body surface. The body pressure coefficients, calculated using Equation G-6 with second order one-sided differences, are plotted in Figures 16, 17, 18, 19, and 33. A typical streamline plot for $\alpha = 11.5°$ is shown in Figure 40. The numerical inviscid solution is also compared with an analytical solution (Reference 67) which uses Theodorsen's (Reference 12) method. The excellent agreement is seen in Figure 33 where both solutions are plotted.

DAT
ILM